Cross-phase modulation effects in normal dispersive fibers and their applications

Marin Gilles

THESE DE DOCTORAT DE L'ÉTABLISSEMENT UNIVERSITÉ
BOURGOGNE FRANCHE-COMTÉ
PRÉPARÉE À L'UNIVERSITÉ DE BOURGOGNE

École doctorale N°553
École Doctorale Carnot-Pasteur

Doctorat de physique

par
Mr. Marin GILLES

Effets de modulation de phase croisée dans les fibres à dispersion normale et leurs applications

Thèse présentée et soutenue à Dijon, le 12 novembre 2018.

Composition du Jury:

Mr. Alexandre Bouhelier	Directeur de recherches UBFC	Président du Jury
Mr. Vincent Couderc	Directeur de recherche CNRS	Rapporteur
Mr. Thierry Chartier	Professeur ENSSAT	Rapporteur
Mr. François Leo	Chargé de Recherches ULB	Examinateur
Mr. Julien Fatome	Ingénieur de recherche CNRS	Co-Directeur
Mr. Christophe Finot	Professeur UBFC	Directeur

Acknowledgments

This Ph.D. work was done in the Laboratoire Interdisciplinaire Carnot de Bourgogne (ICB) at the UFR Sciences et Techniques de l'Université de Bourgogne–Franche-Comté, in the Solitons, Lasers et Communications Optiques (SLCO) team, in Dijon.

My first thanks goes to my Ph.D. supervisor, Julien Fatome. He helped me during these years to accomplish all this work, thanks to his scientific insights and with his moral support. I then want to thank Christophe Finot for the interesting discussions, and for pointing out inconsistencies or missing elements about this work, helping me improve it greatly over time. I also want to thank Massimiliano Guasoni, Javier Nuño and Antonio Picozzi for their participation in the theory and the experiments of this work. I also want to thank Pierre-Yves Bony for helping me get on board when I just started, for sharing his knowledge and for being so curious that it spread on me.

Thank you to all the people I had the chance to spend these years in the lab, Abdelkrim Bendahmane, Manon Lamy, Gang Xu, Kamal Hamami, Guy Millot, Jérémy Picot-Clémente, and all the others I crossed path with.

Thanks to my family for always having been there for me, even in the most difficult moments, whether during the time of this Ph.D. or before, and never letting me down even when everyone else would have. Thank you to my father for always pushing me to do my best, to my grand-mother to giving me the taste for learning and to my mother for her support. Thank you for being proud of me and always believing in me.

Finally, I thank my wife, Hạnh, for guiding me, and helping me become better that I could have ever imagined. I would never have finished or maybe even started this whole adventure without her and my life would not look as good as it does today without her unconditional love and support.

It does not matter how slowly you go so long as you do not stop

Confucius

Contents

Preface

As the technologies of information advance, electronic devices have been reaching their limits in treating optical signals, even more since the development of very short optical pulses down to the atto-second. For this reason, more and more technologies have been developed lately for the all-optical treatment of light, such as the polarization attractor and polarization scrambler realized by Guasoni et al.[1]. For such applications, a lot of research has been done in the field of telecommunications using anormal dispersion fibers, as the solitons used for information transmission appear. Thus, a lot of applications are available with such fibers, but not in normal dispersion fibers, which may be needed in some other fields of research or industry. Some of those applications may include pulse generation, pulse sampling, and data transmission at low and high power. We studied cross-phase modulation in order to solve such issues. In the first part of this work, after introducing the necessary conventions and reminding the reader of the proper optics concepts, we will demonstrate the creation of two applications of cross-phase modulation, to pulse generation and to pulse sampling and magnification in normal dispersion fiber. Those applications were studied experimentally and confirmed theoretically and could be applied in any fibered optical system.

More than 20 years ago, Haelterman et al. showed that a new kind of soliton may appear in isotropic normal dispersion fibers, in which the classical soliton would not. This new type of soliton would come from the equilibrium created by the interplay of chromatic dispersion and the Cross-Phase Modulation (XPM) generated by the pulse on the orthogonal polarization. This effect however could only appear in isotropic fibers, more precisely in fibers with a polarization mode dispersion of an isotropic fiber, which would be null. Such fibers did not exist over a few meters at the time, which made studying the effects described theoretically hard. In the recent years, improvements were made on reducing the Polarization Mode Dispersion (PMD) of the fibers by adding a spinning to the preform of the fiber during drawing, averaging the asymmetry of the fiber core over the length of the fiber. In the second part of this work, and inspired by the work of Haelterman et al., this new kind of solitonic structure, already known in other fields as domain wall, will be studied in telecommunication applications and its origin demonstrated. Their observation will first be demonstrated along with their robustness. An application of those newly observed structure to telecommunication transmission is then demonstrated, before their spontaneous apparition during the propagation of incoherent signals is studied. Finally, the effect at the origin of these structures, the polarization modulation instability, will be observed in shorter fibers, confirming the observations and predictions of Haelterman.

Chapter 1

Introduction

This chapter will serve as a reminder for the physical effects that have been used for the following work. It will also serve as a basis for notations and equations used through this manuscript.

When a pulse of light propagates in an optical fiber, it undergoes a variety of effects, modifying some or all of its characteristics. This work is based upon some of these effects, which we will detail in the following sections.

To get an overview of the main physical phenomena occurring during propagation of light in an optical fiber, the simplest case will be explained first, sending a pulse of light in a single mode optical fiber, in which only the effects of second order chromatic dispersion and Self-Phase Modulation (SPM) are taken into account, by detailing every part of the Nonlinear Shrödinger Equation (NLSE). Then, we will go further by introducing the polarization components of the Kerr effect in the NLSE, allowing for a coupling through the Kerr effect by XPM, to obtain the Coupled Nonlinear Shrödinger Equations (CNSLE), which are the basis for all the work later described in this manuscript.

Finally, we will give a reminder of the main method used to simulate the propagation of optical pulses in an optical fiber, known as the Split-Step Fourier method.

1.1 Nonlinear Shrödinger Equation

In the field of optical signal transmission, the two effects that are encountered in an optical fiber, after the power loss which have now become so small that they are considered as perturbations, are the effects of the second-order chromatic dispersion, and, when the power of the signal becomes large enough, of SPM. In order to simplify the studies and numerical calculations, a simple equation has been derived from the Maxwell's Equations. The equation, called the Nonlinear

Shrödinger Equation, is formulated as, in its simplest form using only second order chromatic dispersion and SPM[2]

$$i\frac{\partial A}{\partial z} + \frac{\alpha}{2}A - \frac{\beta_2}{2}\frac{\partial^2 A}{\partial T^2} + \gamma |A|^2 A = 0 \tag{1.1}$$

with the terms:

- A Pulse amplitude (V/m)
- z Spatial position on the axis of the fiber (m)
- T Time in the moving frame of reference of the pulse defined as $T = t - z/v_g = t - \beta_1 z$, t being the time in the reference framework of the fiber, β_1 the first order chromatic dispersion coefficient. (ps)
- αA Losses coefficient ($\mathrm{dB\,km^{-1}}$)
- β_2 Second-order chromatic dispersion parameter ($\mathrm{ps^2\,m^{-1}}$)
- γ Nonlinear coefficient ($\mathrm{W^{-1}\,m^{-1}}$)

There are some limitations to this equation, such as the fact that it is a scalar model, and multiple approximations were taken into account to allow for it to be derived[2]. The first main approximation is the slowly varying envelope approximation, stating that the envelope of the forward propagating wave is considered to be varying slowly in time and space compared to the wavelength of the signal. It is also considered that the polarization is maintained during the propagation in the fiber. While this is usually not true, this approximation brings a lot of simplifications while keeping the equation easy. Other effects were not taken into account, such as higher-order dispersion, Raman and Brillouin scattering and losses.

This equation is simple, but already covers a lot of usual cases, allowing for quick understanding and easy simulations of two of the main effects that can occur in an optical fiber. We can clearly see three different parts to this equation. Let us explain which effect every part corresponds to before going into more details about each phenomenon.

$i\frac{\partial A}{\partial z}$ describes the propagation of the pulse along the z axis, meaning along the fiber.

$\frac{\alpha}{2}$ describes the losses observed by the signal during its propagation

$\frac{\beta_2}{2}\frac{\partial^2 A}{\partial T^2}$ describes the second order chromatic dispersion applied to the pulse in the fiber during its propagation.

$\gamma |A|^2 A$ describes one of the nonlinear Kerr effect the pulses undergo inside the optical fiber. This term corresponds to the SPM effect.

This equation can be rewritten with explicit dispersion and nonlinear operators as

$$\frac{\partial A}{\partial z} = (\hat{D} + \hat{N})A \tag{1.2}$$

With $\hat{D}$ corresponds to the dispersion operator, and $\hat{N}$ corresponds to the nonlinear operator, where

$$\hat{D} = \frac{\alpha}{2} - \frac{i\beta_2}{2}\frac{\partial^2}{\partial T^2} \tag{1.3}$$

$$\hat{N} = i\gamma |A|^2 \tag{1.4}$$

Before increasing the complexity of this equation, it is important to understand this first equation, and what physically happens when the pulse is propagating inside the fiber.

1.1.1 Chromatic dispersion

To understand the chromatic dispersion, it is first important to analyze how a pulse is composed. To illustrate more easily, let us study a Gaussian pulse Fig. 1.1(a). To every pulse is associated an optical spectrum, representing the frequency distribution inside the optical pulse Fig. 1.1(b). This spectrum is linked mathematically by the Fourier transform (FT), which is defined by:

$$\mathcal{F}\{f\}(\omega) = \tilde{f}(\omega) = \int_{-\infty}^{\infty} f(t) \exp^{-2\pi i t\omega}\, dt \tag{1.5}$$

However, inside an optical fiber, not every wavelength propagates at the same speed. This phenomenon is similar to what happens when sending a ray of light in a prism. When sending in a ray of light, the colours composing the ray of light will be separated, as the refractive index is wavelength dependent. This phenomenon is called chromatic dispersion. If we plot the evolution of the speed of light in silica as a function of its wavelength, we obtain a plot similar to Fig. 1.2, displaying the evolution of the refraction index of the material for different wavelengths.

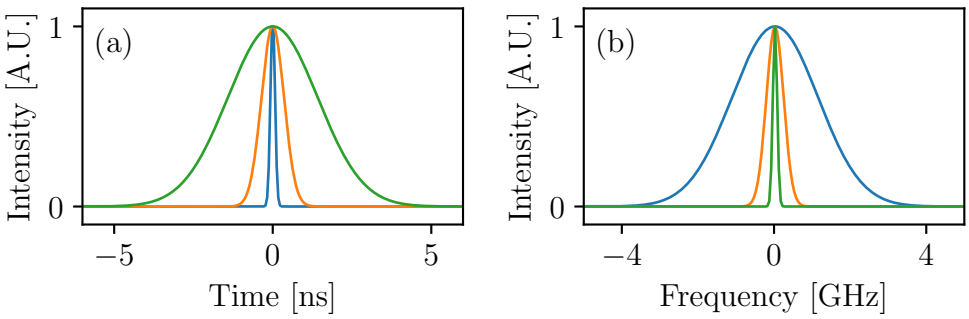

Figure 1.1: A gaussian pulse (a) and its associated optical spectrum (b)

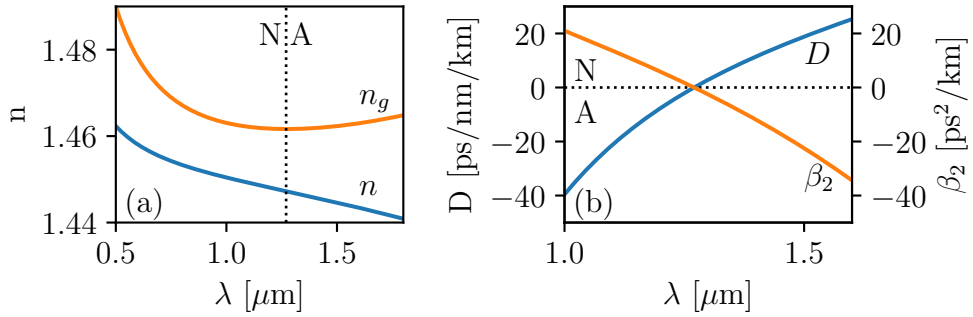

Figure 1.2: (a)Evolution of the refraction index and (b) associated chromatic dispersion inside a silica fiber with the wavelength. N: Normal dispersion regime, A: Anomalous dispersion regime

So when the pulse propagates, the photons at one edge of the spectrum will go faster than the others, which can impact the shape of the pulses depending on the sign of the dispersion of the medium. The effects of such dispersion can have a very different impact depending on the shape of edge the pulse, and more particularly, the shape of its spectrum. If the spectrum is very thin (broad pulse), the difference between the speed of the photons on the lower and the higher edge of the spectrum will be very small, as the difference in wavelength is minor, inducing only a tiny dispersion on the pulse. Inversely, if the spectrum is broad (short pulses), the large difference in wavelength will induce a high speed difference, leading to a more pronounced dispersion, inducing a dramatic pulse temporal broadening.

As we can notice, in the dispersion term of Eq. (1.1), the higher the second order derivative of the pulse amplitude envelope, the larger the dispersion effect, which means that the strength of the dispersion is linked to the evolution of the

signal with time. To illustrate with a gaussian pulse, the shorter the pulse, the faster its evolution, and so the higher dispersion it undergoes. This is only true, however in the case for which the pulses are in the Fourier transform limit, meaning they hold no chirp.

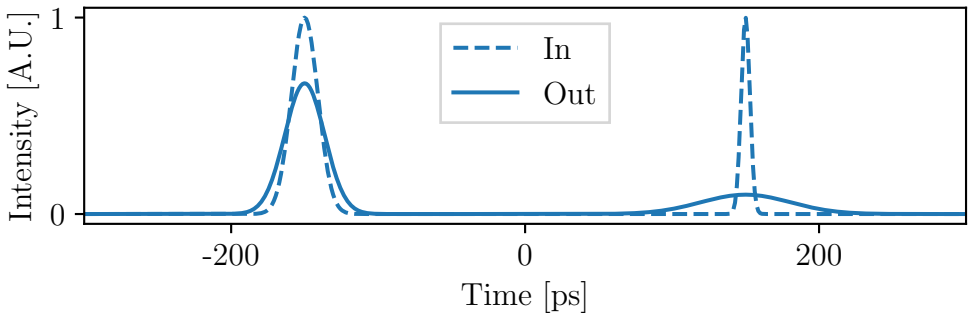

Figure 1.3: Evolution of pulses undergoing dispersion in an optical fiber. Dashed lines are the input signal, solid lines are the output. $\beta_2 = 18.5\,\mathrm{ps}^2\,\mathrm{km}^{-1}$, $L = 10\,\mathrm{km}$

In Fig. 1.3, an example of two gaussian pulses transmitted in a standard optical fiber is shown, taking into account only the chromatic dispersion. For this, we used the NLSE, but without the nonlinear response, giving us the equation Eq. (1.6). As we can see, at the end of the fiber, the shortest pulse has broadened 10 times, while the longer pulse only broadened about 1.5 times.

$$i\frac{\partial A}{\partial z} - \frac{\beta_2}{2}\frac{\partial^2 A}{\partial T^2} = 0 \tag{1.6}$$

While we are now able to understand the effect of dispersion, we now need to understand very quickly how much of an impact it will have on the propagation of a pulse inside a fiber. To this aim, a dispersion length L_D was introduced, providing a length for which the dispersive effect become important[2], meaning here that the pulse has broadened by a factor of $\sqrt{2}$. It is defined as

$$L_D = \frac{T_0^2}{|\beta_2|} \tag{1.7}$$

With β_2 the dispersion coefficient of the fiber, and T_0 the input pulse width, which in the case of the Gaussian pulse is the half-width at $1/e$. While this relation is only applicable for gaussian pulses, it is commonly used with a large range of different pulses.

For a more practical use, if the dispersion length L_D of a pulse propagating in a fiber is much larger than the length of the fiber L, meaning $L_D \gg L$, then we can

approximate that the transmission is dispersionless, as the effect is not significant enough to modify the signal.

1.1.2 Self-Phase Modulation (SPM)

Let us now explore the second phenomenon taken into account in Eq. (1.1). This second element is linked to one of the nonlinear phenomenon occurring inside the fiber, namely the Kerr effect, and more precisely, the SPM.

SPM comes from the interaction between the light and the material it propagates in. As photons propagate, they interact with the electrons and nuclei of the material, leading to a local change of properties of the material, namely a change in the refractive index. Indeed, the refractive index can be written as

$$\tilde{n}(\omega, I) = n(\omega) + n_2 I = n(\omega) + \bar{n}_2 \left|E\right|^2 \tag{1.8}$$

where $n(\omega)$ is the linear part, I is the optical intensity of the signal and $\bar{n}_2$ is the nonlinear-index coefficient, and E is the electrical field of the signal propagating in the fiber, A being the envelope of the component dependant on the z axis of the fiber of the electrical field E. This nonlinear interaction leads to the apparition of a nonlinear phase shift that can be calculated using the equation

$$\phi_{\mathrm{NL}} = \left(\bar{n}_2 \left|E\right|^2\right) k_0 L \tag{1.9}$$

where $k_0 = 2\pi/\lambda$ and L is the total length of the fiber.

The propagation of the pulse in an optical fiber was then simulated, including only the SPM effect, for gaussian pulses with a peak intensity varying from 0.1 W to 1.5 W. In such a case, no dispersion was applied, allowing for the reduction of Eq. (1.10) to

$$i\frac{\partial A}{\partial z} - \gamma \left|A\right|^2 A = 0 \tag{1.10}$$

where $\gamma(\omega_0) = \omega_0 n_2 / c A_{\mathrm{eff}}$, with ω_0 being the central wavelength of the spectrum, and A_{eff} the effective mode area.

As we can notice on Fig. 1.4(a), the temporal shape of the pulse is not modified by the SPM effect. However, the spectrum in the case of the high intensity pulse is completely changed by the SPM through nonlinear phase modulation leading to the appearance of new frequencies, while the spectrum of the low intensity signal remains almost unchanged, as seen on Fig. 1.4(b).

It is now useful to define a characteristic quantity that will help to characterize the SPM. Similarly to Eq. (1.7), a nonlinear length L_{NL} can be defined. This

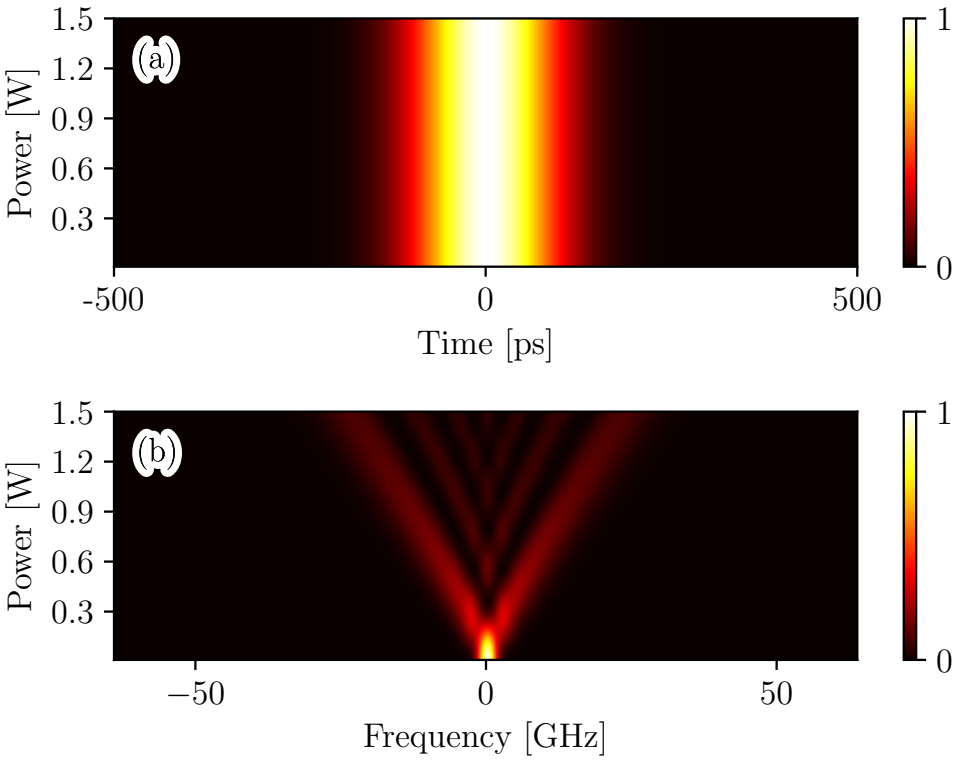

Figure 1.4: Evolution of (a) the temporal intensity profile and (b) the spectrum of a gaussian pulse with input pulse peak power. $L = 10\,\text{km}$ and $\gamma = 1.4\,\text{W}^{-1}\,\text{km}^{-1}$

length is the effective propagation distance for which the maximum phase shift $\phi_{\text{NL, max}} = 1\,\text{rad}$, as described in [2]. L_{NL} can then be written as

$$L_{NL} = \frac{1}{\gamma P_0} \tag{1.11}$$

where P_0 is the peak power of the pulse. It can be noticed that this length depends directly on the peak power of the signal, and that the more power, the less distance will be needed for the SPM to have a noticeable impact. As in Section 1.1.1, if $L_{NL} \gg L$, we consider the SPM to have no impact onto the transmission of the signal through the fiber and approximate the propagation as linear.

1.1.3 Soliton in the NLSE

A very interesting effect that arises from the interplay between the second order chromatic dispersion and the SPM is when each effect compensates the contribution of the other. When this happens, a soliton, which is a pulse that propagates

without deformation, appears. Since their discovery[3], solitons have been studied extensively in diverse media including optical fibers[4–6]. In our case, only the fundamental soliton will be presented. For it to appear, a perfect balance between the chromatic dispersion and the SPM is required, meaning

$$L_{NL} = L_D \tag{1.12}$$

leading to the relation between dispersion, temporal width and peak power :

$$\frac{\gamma P_0 T_0^2}{|\beta_2|} = 1 \tag{1.13}$$

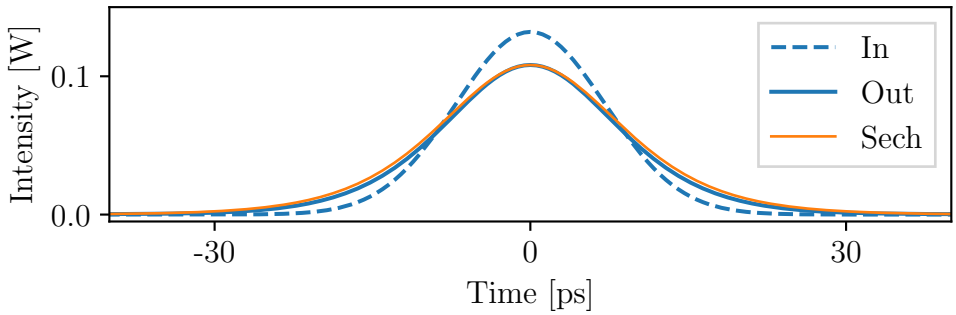

Figure 1.5: Reshaping of a pulse into a soliton during the propagation of a 10 ps Gaussian pulse in a 10 km fiber (losses neglected). $\gamma = 1.4\,\mathrm{W^{-1}\,km^{-1}}$, $\beta_2 = -18.5\,\mathrm{ps^2\,km^{-1}}$

By using an inverse scattering method[2], it is possible to show that the solution for the fundamental soliton in an optical fiber, considering the NLSE model is of the form

$$u(\xi, \tau) = sech(\tau) \exp(i\xi/2) \tag{1.14}$$

with $\xi = z/L_D$ the normalized number of dispersive (and nonlinear, in this case) lengths, $\tau = T/T_0$, the normalized time and $u = A\sqrt{\gamma L_D}$ the normalized envelope of the signal.

A very interesting property of these solitons is that they are very robust. Indeed, even if in reality the fibers are more complex than described in the NLSE model, solitons can be observed to propagate through very long distances. Moreover, as they lose energy, or are deformed by other unaccounted for physical effects, they adapt to stay in a solitonic state, meaning the mutual counteracting of the chromatic dispersion and SPM will still occur, even if the pulses are modified slightly. Moreover, if the starting pulse is not perfectly solitonic, it will evolve as

it propagates towards a solitonic state, if it is close enough at the input of the fiber[2], as illustrated by Fig. 1.5. The input gaussian pulse, with parameters validating Eq. (1.13) is clearly seen on this figure to be reshaped during propagation and the pulse at the output is an almost exact hyperbolic secant shaped pulse.

1.1.4 Modulation Instability

An other interesting phenomenon arising from the interaction between the chromatic dispersion and nonlinear effects is the modulation instability, which comes from an instability of a continuous wave towards small perturbations caused by the interplay between both effects[7,8].

This process can be seen as a three-wave mixing between a high-power pump, a signal and an idler. In such a case, two photons of the same frequency ω_0 from the pump are transformed into two, at the signal frequency $\omega_1 = \omega_0 + \Omega$ and at the idler frequency $\omega_0 - \Omega$, both experiencing a net gain given by Eq. (1.15)

$$g(\Omega) = |\beta_2 \Omega| \left(\Omega_c^2 - \Omega^2\right)^{1/2} \tag{1.15}$$

where g is the gain observed by the signal, and

$$\Omega_c^2 = \frac{4\gamma P_0}{|\beta_2|} \tag{1.16}$$

defines the critical frequency under which gain is observed. This equation was obtained by executing a stability analysis of the basic NLSE equation in the case of a continuous wave (CW) wave. Eq. (1.15) shows that there is a maximum frequency Ω_c over which this signal amplification does not occur anymore, as there would be no real solution to the equation in the case where $\Omega > \Omega_c$.

There are two applicable cases of this equation. If a signal is actually sent co-propagating with the CW pump wave, *seeded* Modulation Instability (MI) appears, the CW wave allowing for the gain to be more visible. If not, the background noise acts as a seed, and a gain spectrum containing two symmetrical sidebands is observed, similarly to Fig. 1.6, and is called *spontaneous* MI. On this figure, the result of the theoretical band shape from Eq. (1.15) is plotted along with the simulation of the propagation of a noisy CW wave.

By plotting the gain relation, the bands shape can be seen, as illustrated on Fig. 1.6. On this figure, one can see that there is a frequency Ω_{max} for which the gain is maximum. This frequency can be calculated using the relation

$$\Omega_{max} = \pm \frac{\Omega_C}{\sqrt{2}} = \pm \left(\frac{2\gamma P_0}{|\beta_2|}\right)^{1/2} \tag{1.17}$$

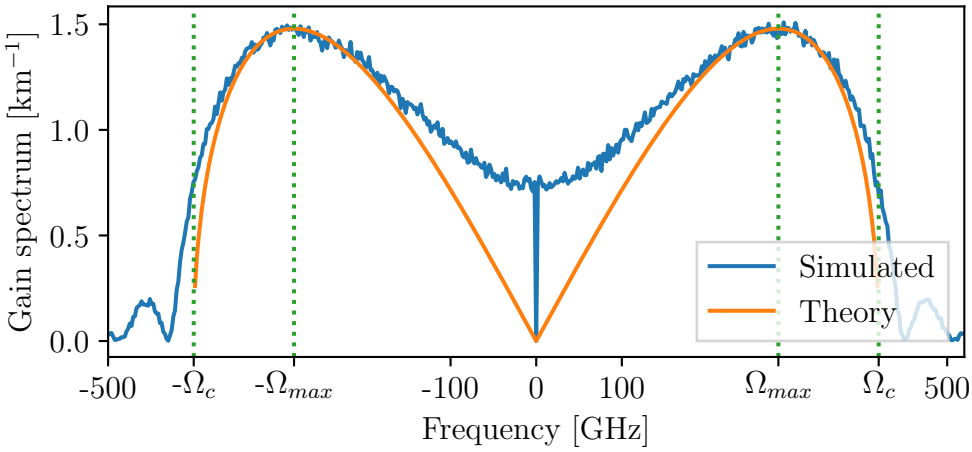

Figure 1.6: Bands generated by modulation instability. $\gamma = 1.4\,\mathrm{W^{-1}\,km^{-1}}$, $\beta_2 = -18.5\,\mathrm{ps^2\,km^{-1}}$, $L = 10\,\mathrm{km}$, $P_{\mathrm{pump}} = 0.52\,\mathrm{W}$

and by replacing in the expression of the gain, it is possible to calculate the maximum gain at Ω_{max} using the expression

$$g_{max} \equiv g(\Omega_{max}) = \frac{1}{2}\,|\beta_2|\,\Omega_c^2 = 2\gamma P_0 \tag{1.18}$$

It can be seen that the gain does not depend on the dispersion parameter, but linearly increases with the power. This process has been extensively studied to develop parametric amplifiers[9,10].

1.2 Coupled Nonlinear Shrödinger Equations

While the NLSE is very useful for a number of cases, it can become limiting, lacking to take physical effects into account. An addition that can be made is to take into account two orthogonally polarized signals. Such an extension allows to study the evolution of each signal independently of the other, and observe the coupling effects that appear.

As two coupled signals will be studied, a system of coupled equations is derived. However, depending on the polarization basis, the system can be slightly altered. For this case, the simplest form of the equations is used, which comes from writing the equations in the circular polarization basis.

To write these equations, It was assumed that the fiber has very low birefrin-

gence (isotropic case). The equations can then be written as :

$$\begin{aligned}\frac{\partial A_+}{\partial z}+\frac{\alpha}{2}A_+ + \frac{i\beta_2}{2}\frac{\partial^2 A_+}{\partial T^2} &= \frac{2i\gamma}{3}\left(c_{SPM}\left|A_+\right|^2 + c_{XPM}\left|A_-\right|^2\right)A_+ \\ \frac{\partial A_-}{\partial z}+\frac{\alpha}{2}A_- + \frac{i\beta_2}{2}\frac{\partial^2 A_-}{\partial T^2} &= \frac{2i\gamma}{3}\left(c_{SPM}\left|A_-\right|^2 + c_{XPM}\left|A_+\right|^2\right)A_-\end{aligned} \tag{1.19}$$

with A_+ and A_- representing respectively the right- and left-handed circularly polarized states, $C_{SPM} = 1$ when the fiber is considered randomly birefringent[11] and $C_{XPM} = 2$ in the case of an isotropic fiber[12]. The elements of dispersion and SPM are still present in this equation, but a new term appeared in the nonlinear part. This term, representing the coupling between the two signals, is responsible for the effect of XPM.

To study the randomly birefringent model, which describes accurately long fibers, Eq. (1.19) were further derived accounting for the average birefringence over the length of the fiber, and the time and space coordinates were normalized with, respectively, the dispersion and nonlinear length, leading to the couple of equations Eq. (1.20), called the Manakov model.

$$\begin{aligned}i\frac{\partial u}{\partial \xi}+\frac{\alpha}{2}u+\frac{1}{2}\frac{\partial^2 u}{\partial \tau^2}+(\left|u\right|^2+\left|v\right|^2)u &= 0 \\ i\frac{\partial v}{\partial \xi}+\frac{\alpha}{2}v+\frac{1}{2}\frac{\partial^2 v}{\partial \tau^2}+(\left|v\right|^2+\left|u\right|^2)v &= 0\end{aligned} \tag{1.20}$$

with $u = A_x\sqrt{\gamma L_D}\exp(i\Delta\beta z/2)$, $v = A_y\sqrt{\gamma L_D}\exp(i\Delta\beta z/2)$, the normalized amplitude where A_x and A_y are the envelope amplitudes and $\Delta\beta$ the birefringence coefficient, $\xi = z/L_D$ and $\tau = (t-\beta_1 z)/T_0$.

Vectorial Cross-Phase Modulation

The vectorial XPM comes, similarly to the SPM, from the optical Kerr effect, which appears from an interaction of the light with the propagating media by modulation of the refractive index. While the SPM arises from a light modifying its properties through its own interactions with the media, the XPM comes from the modification of a signal through the interaction of a second signal with the media, thus creating a new interaction between the first signal and the propagation media. As a simple view, it seems that both signals are coupled, as can be seen in Eq. (1.19), where a coupling factor appears.

Similarly to the SPM Section 1.1.2, the XPM effect is based on the modification of the refractive index of the fiber, thus modulating the phase of the signals, inducing a modification of the frequency across the pulse. Such a modulation of frequency is called a chirp, and is defined as

$$\delta\omega(T) = -\frac{\partial\phi}{\partial T} \tag{1.21}$$

However, although this modulation has an effect on the signal which generated it (SPM), it also creates a phase modulation on the other signals present in the fiber. In the case of the vectorial XPM, the modulation is created on the signal that is orthogonally polarized, creating new frequencies, the same way new frequencies are created by SPM.

In the case of the isotropic model, the nonlinear coefficients are $c_{SPM} = 1$ and $c_{XPM} = 2$. This means that the XPM will be twice as effective as the SPM. This implies that the signal spectrum will broaden twice as much on the orthogonal polarization than on the parallel. This phenomenon is illustrated on Fig. 1.7.

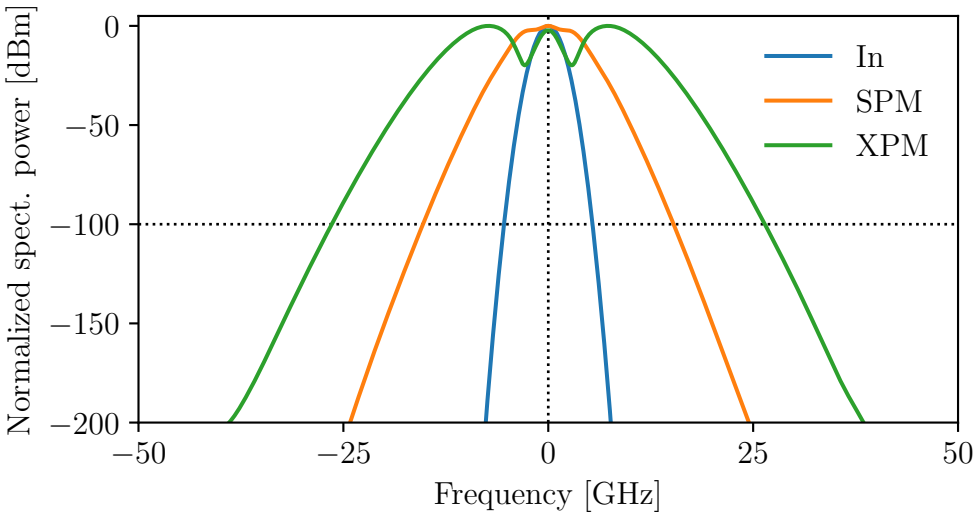

Figure 1.7: Illustration of the broadening of the spectrum by SPM and XPM in the isotropic case (simulation with losses neglected). $\gamma = 1.4\,\mathrm{W^{-1}\,km^{-1}}$, $\beta_2 = -18.5\,\mathrm{ps^2\,km^{-1}}$, $L = 10\,\mathrm{km}$, $P_{\mathrm{pump}} = 1\,\mathrm{W}$

1.3 Simulation methods

In order to simulate the previous equations, and for all the simulations of this manuscript, the Split-Step Fourier method[13] has been used, as it is the fastest and easiest solution. The method will be explained here only for the NLSE, and will be left to expand, more complex equations, to the reader if necessary.

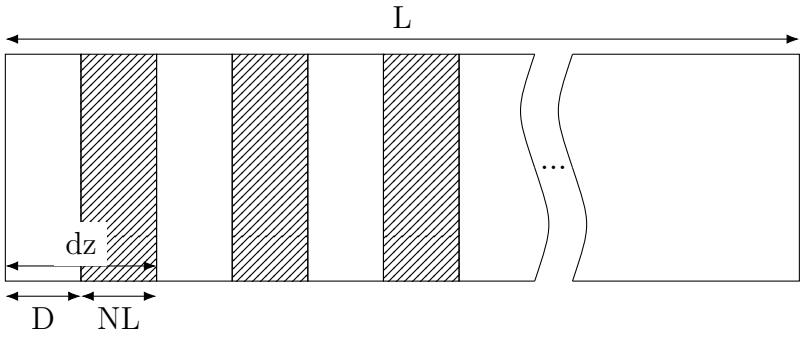

Figure 1.8: Illustration of the Split-Step Fourier method. D stands for the dispersion step, NL for the Nonlinear step. Both are applied one after the other, on the whole dz step.

The Split-Step Fourier method is a two-step simulation method. By taking a distance of propagation small enough, on which dispersion and non-linearity don't have a high enough impact, we can apply each effect one after the other (the two steps) on the signal, upon this small length of fiber[13]. By iterating onto each part of the fiber, we can then get the total transformation of the signal after propagation through the whole fiber. The method is illustrated by Fig. 1.8.

By assuming, as previously stated, that the dispersive effects and nonlinear effects act independently, we can rewrite Eq. (1.2) for a single step of the simulation to separate the two effects, leading to

$$A(z+h,T) = \exp(h\hat{D})\exp(h\hat{N})A(z,T) \tag{1.22}$$

While the nonlinear transformation can easily be applied, the dispersion operator contains a derivative, which is quite slow to calculate. Moreover, dispersion is directly linked to $n(\omega)$, which gives its application to the transformation in the frequency domain physical sense. The dispersion effect is thus evaluated in the Fourier domain, thanks to the relation:

$$\exp(h\hat{D})B(z,T) = \mathcal{F}_T^{-1}\left\{\exp(h\mathcal{F}_T\left\{\hat{D}\right\})\mathcal{F}_T\left\{B(z,T)\right\}\right\} \tag{1.23}$$

A single step of the simulation, from z to $z+h$ is then composed of

1. Get the signal at z
2. Apply the dispersion operator in the Fourier domain to the signal, on a length of h to get the signal with dispersion at $z+h$
3. Apply the nonlinear operator in the time domain, to the previous signal, on a length of h.

By applying this method for $z \in [0, L]$, we obtain, at the end, the signal in $z = L$.

The Split-Step Fourier method was shown to be one of the fastest methods to simulate the propagation of optical pulses inside a fiber. Numerous amelioration have been added, which can increase the speed and/or the precision of the simulation, but are always based on this basic technique.

Chapter 2

Nonlinear optical functionalities based on cross-polarized phase modulation in telecom fibers

One of the main limitations of optical telecommunications systems is linked to the electrical bandwidth of equipments, limiting the optical generation and characterization to the bandwidths of those equipments, going up to a maximum of around 100 GHz. To get over those limitations, multiple all-optical applications were designed such as autocorrelators[14] and Frequency-Resolved Optical Gating (FROG)[15] for measurement, as well as mode-locked lasers[16,17] and pulse compression schemes for generation[2,18–32].

In this context, ultra-fast optical functions can be developed by using the coupling between two waves through nonlinear interactions in optical fibers. Thus, when one of the signals can be acted upon, the evolution of the second can also be modified through the coupling. Such coupling effects have been demonstrated over the years, such as Sum Frequency Generation (SFG), four-wave mixing, inter-mode coupling and cross-phase modulation. Those effects have been used to develop amplifiers, all-optical polarizers, frequency combs, and optical gates.

In this work, two all-optical applications were designed and studied by taking advantage of the cross-phase modulation coupling between copropagating signals. First, a novel pulse source based on the compression of pulses in a normally dispersive telecom fiber generated from a sinusoidal beat signal by cross-phase modulation was designed and studied experimentally and numerically. Secondly, an all-optical sampler and magnifier based on the same principle and demonstrating a noise free magnification and tunable sampling rate will then be detailed and characterized. Finally, a conclusion on both these experiments will be drawn and further possible applications put into light. This work was realized in collaboration with Mr. Massimiliano Guasoni and Mr. Javier Nuño.

2.1 XPM-induced pulse source through beat-signal pulse compression

The ability to design optical pulse sources at repetition rates of tens of GHz is of high interest in many fields of photonics, including optical communications, sampling, metrology, clocking, sensing, spectral comb, and arbitrary waveform generation. To develop alternative solutions to traditional mode-locked fiber lasers, numerous cavity-less scenarios have been investigated based on the nonlinear reshaping within optical fibers of an initial beat signal into a train of well-separated pulses[18]. Basically, the nonlinear temporal compression of the initial beating is induced through the focusing regime of the NLSE, taking advantage of the interplay between the nonlinear Kerr effect and the anomalous dispersive regime[2]. This particular technique has been demonstrated in a wide range of fiber arrangements to produce pedestal-free pulse trains or frequency combs at various repetition rates, ranging from GHz to several THz[2,18–32]. To this aim, various fiber concatenation systems have been implemented, including dispersion decreasing fibers[19], comb-like or step-like fiber profiles[20,33], modulation instability[22], XPM[23], multiple Four-Wave Mixing (FWM)[24–29], parametric amplification[31], and Raman amplification[32].

2.1.1 State of the art

Compression of pulses is a very important application of nonlinear systems. While multiple techniques can be used to compress pulses, the principle used stays the same, where a chirped signal is passed through a dispersive media, thus cancelling the chirp and inducing the compression. The main compression schemes will be reminded, giving a point of comparison with the compression scheme developed in this section.

Grating-fiber SPM compression

The first developed method of pulse compression, and still the most used to this day, was based on the association of a fiber and gratings, as displayed on Fig. 2.1. The pulse was first coupled into a normal-dispersion single mode fiber, leading to the development of a chirp with a positive slope along the span of the pulse, and broadening of its spectrum due to SPM in the fiber. The pulse is then sent through a grating pair, which acts as a dispersive delay line, where it experiences anomalous Group Velocity Dispersion (GVD). This effectively cancels the chirp induced by SPM while conserving the broad spectrum generated after propagation, thus leading to the compression of the pulse[34].

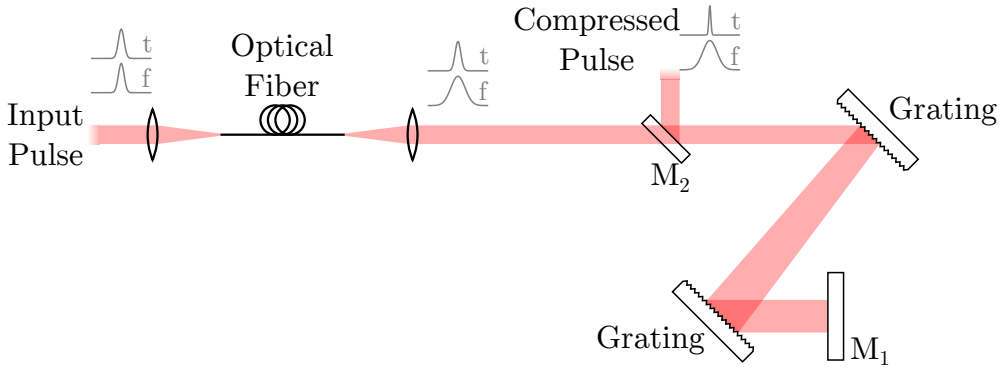

Figure 2.1: Grating-fiber compression schematic. M_1 is a mirror and M_2 is a one-way mirror

It must be noted that this technique suffers multiple limitations. While the system works optimally with an unchirped pulse, as do all the techniques detailed in this section, the compression will be reduced in the cases of down-chirped, up-chirped or random-chirped input pulses. Moreover, while a full theory was developed to work more easily with grating-fiber compressors, it is only applicable while pulse width is large enough, namely over 1 ps. If this threshold is reached, higher order nonlinear and dispersion effects appear, leading to a reduction of the linearity of the chirped signal at the output of the fiber, thus a reduction in the compression efficiency. Similarly, if the pulse width become even shorter, under 50 fs, the gratings response change to include higher-order effects, effectively reducing the compression ratio. Finally, Raman scattering is a significant limitation, as one must avoid the transfer of energy to the Raman pulse by reducing the power under the Raman threshold. As for all the nonlinear compression methods, while increasing the power theoretically increases the compression ratio, apparition of Raman scattering can lead to interaction with the pulse, and unbalance the linearity of the pulse chirp.

Soliton based compression

The second main method of pulse compression is the use of the well known solitons that appear in the NLSE. It was shown that in an anomalous dispersion fiber, solitons can propagate through a balance between the dispersion and SPM. However, when the ratio between the dispersion length and nonlinear length $L_D/L_{NL} = N$, with N being an integer $\gg 1$, the formation of higher-order solitons was observed along the fiber length, and pulses with a much shorter Full-Width Half Maximum (FWHM) that the input pulse are then generated[35]. By adapting the ratio to have short pulses appearing at the end of the fiber, it is thus possible to compress the

input pulse into a much shorter one. Compression ratios up to 3700 have been reached through multiple soliton based compression schemes[36]. This method was however highly limited by the appearance of pedestals to the pulses and the instability of the technique. It must be noted that similarly to the previous compression scheme, when the pulse is short enough, with a width under 100 fs, higher order effects must be taken into account to obtain a precise estimation of the compression ratio and the optimal fiber length at which the shortest pulse appears.

Dispersion decreasing fibers

As was demonstrated in Chapter 1, there is a particular solution to the NLSE equation, that leads to the propagation of solitons in optical fibers with an anomalous dispersion. This effects arises from the compensation of the GVD by the SPM.

However, by unbalancing those two terms very slightly, the soliton will adapt, and its shape will change, given the changes are small enough (*i.e.* the GVD does not change much over the dispersion length, or similarly for the nonlinear coefficient over the nonlinear length)[18]. The solitons will, under these conditions, keep the same pulse energy E_0, leading to the following relation

$$E_0 = 2P_0(z)T_0(z) = -\frac{2\beta_2(z)}{\nu(z)T_0(z)} = Cste \tag{2.1}$$

where $\nu(z) = \exp(-\alpha z)\gamma(z)$, α being the loss (or amplification) coefficient of the fiber.

From this equation, it can be easily seen that by gradually reducing the GVD coefficient β_2 along the fiber, the pulse width will also gradually decrease to keep the energy constant, given that the nonlinear coefficient stays constant. Similarly, if ν increases, meaning an increase of the nonlinear coefficient or an amplification along the fiber, the pulse will also gradually compress during propagation (this phenomenon will be studied in Section 2.1.1). This compression process is called the Adiabatic Soliton Compression (ASC), and leads to compression without addition of new components to the signal, like pedestals or the dispersive wave of the pulse.

Using this phenomenon, a first approach studied was to create a fiber with an actual decreasing GVD along its length, the Dispersion Decreasing Fibers (DDF)[19], the GVD being illustrated in Figure 2.2. Indeed, the GVD and Kerr coefficient are dependent on the core radius. By adapting it along the fiber, a decrease in the GVD was thus realized, effectively allowing the pulse to be compressed through ASC, while the Kerr coefficient increases, improving further the compression.

This method has been proven successfully, and have been implemented in a number of different fiber types, like Erbium-doped DDF[37], Dispersion-flattened

DDF (DF-DDF)[38,39], polarization-maintaining DF-DDF[40] and photonic crystal fibers[41,42].

This type of fibers has the advantage of compression without other external device, like would be the case in Raman amplification based compression (Section 2.1.1). It has been shown that the compression ratio, $R = \Delta T_{in}/\Delta T_{out} = \beta_{2in}/\beta_{2out}$, which can be both an advantage, allowing to get a precise compression ratio when making the fiber, and a drawback, making it impossible to tune the ratio once the fiber is drawn, thus needing to make a new fiber for each new desired compression ratio. Another main drawback of this technique is that the fibers are quite difficult to produce, as they are created by constantly changing the drawing conditions of the fiber, thus making it very difficult to reproduce the process in a consistent way.

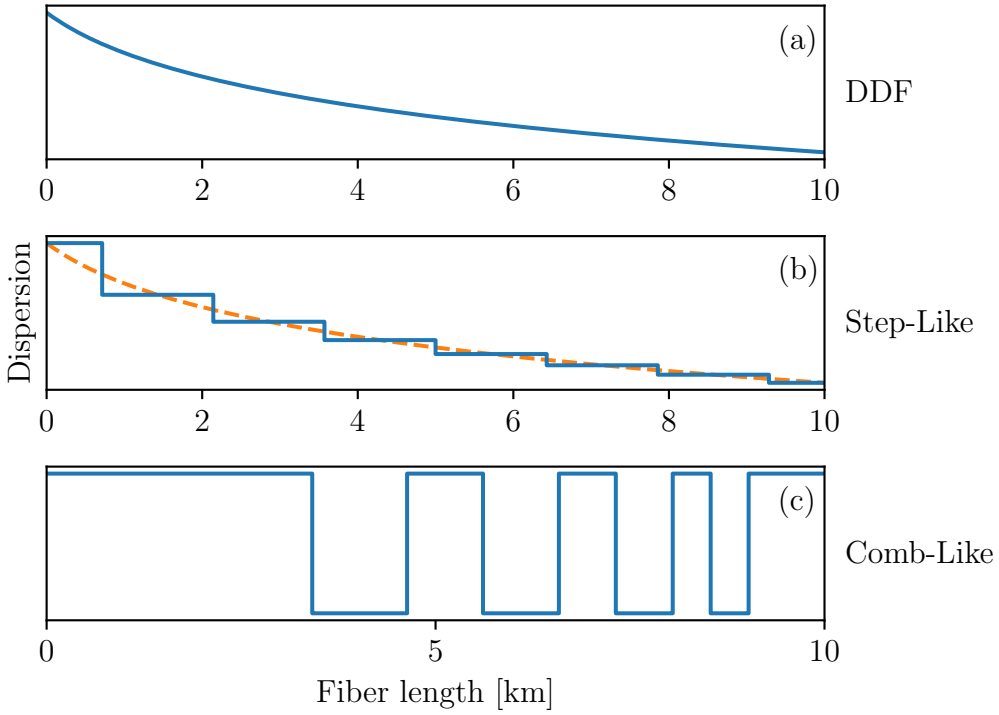

Figure 2.2: (a) DDF; (b) Step-Like profile; (c) Comb-Like profile

Step-like and comb-like fiber profiles

The DDF being hard to manufacture, a first solution to make manufacturing easier is to mimic such fibers by creating fibers that have a decreasing dispersion, but averaged on small distances (relative to the dispersion length).

The first of those methods is to make a step-like dispersion fiber Step-like Profiled Dispersion Fiber (SPDF) (Figure 2.2b). By splicing fibers with constant dispersion coefficient, but decreasing a bit over each portion, the total dispersion seen by the pulses travelling through the fiber is similar to a linearly decreasing dispersion. The number of different fibers that have to be used to implement such a system is linked to the number of steps one wants to achieve. The more steps, the more there will be different fibers.

Building on this method, there is an other way to create a DDF. Instead of using multiple different fibers for each step, one can use two fibers, with a higher dispersion gap, according the length of each segment so that the dispersion seen when travelling through both of them is equal to the dispersion that would be seen in a single of the previous steps, forming a comb-like dispersion profile (Figure 2.2c). These fibers are thus called Comb-like Profiled Dispersion Fiber (CPDF). In this technique, one of the fibers is used as the dispersive element (usually a Single Mode Fiber (SMF) fiber), and the other as a nonlinear element (usually a Dispersion Shifted Fiber (DSF) fiber).

Using both these techniques, the manufacturing is easier, and more consistent. Indeed, creating fibers with a constant dispersion coefficient has become easy. Step-like fibers however, still come with more constraints. One would indeed need one particular fiber for each of the resulting fiber segment. The particularly needed fibers would be hard to come by in a typical laboratory, unless one fabricates them. Thus, the method would only be really applicable in a laboratory where the fibers can be directly manufactured. The comb-like method, on the other hand, would allow a reduction of the dispersion in between two extremes, at the cost of more splicing, as only two different fibers are needed to implement it.

By using the CPDF method, but replacing the DSF by a Highly NonLinear Fiber (HNLF), is created a Comb Profile Fibers (CPF)[18]. This kind of fiber is interesting in that it allows both ASC, when using a fine fiber structure, and steep compression, using a coarser fiber structure. It also allows better management of the individual effects (dispersion and nonlinearity), the HNLF increasing significantly the nonlinearities, as seen on Figure 2.3b, making the dispersion in those fiber segments negligible. At the same time, introducing the HNLF allows to launch lower input power, thus reducing the nonlinear effects in the dispersion segments of the fiber. However, it must be noted that splicing HNLF fibers is quite difficult, thus making the splicing losses important to take into account.

Being able to manipulate both effects independently allows for easy tuning. Using the nonlinear segment, the signal spectrum is broadened through SPM. Then the induced chirp is compensated by dispersion in the following segment, the length of the segments being the parameter allowing to control how much nonlinearity and dispersion is applied to a pulse at each step. The fiber thus created is not just

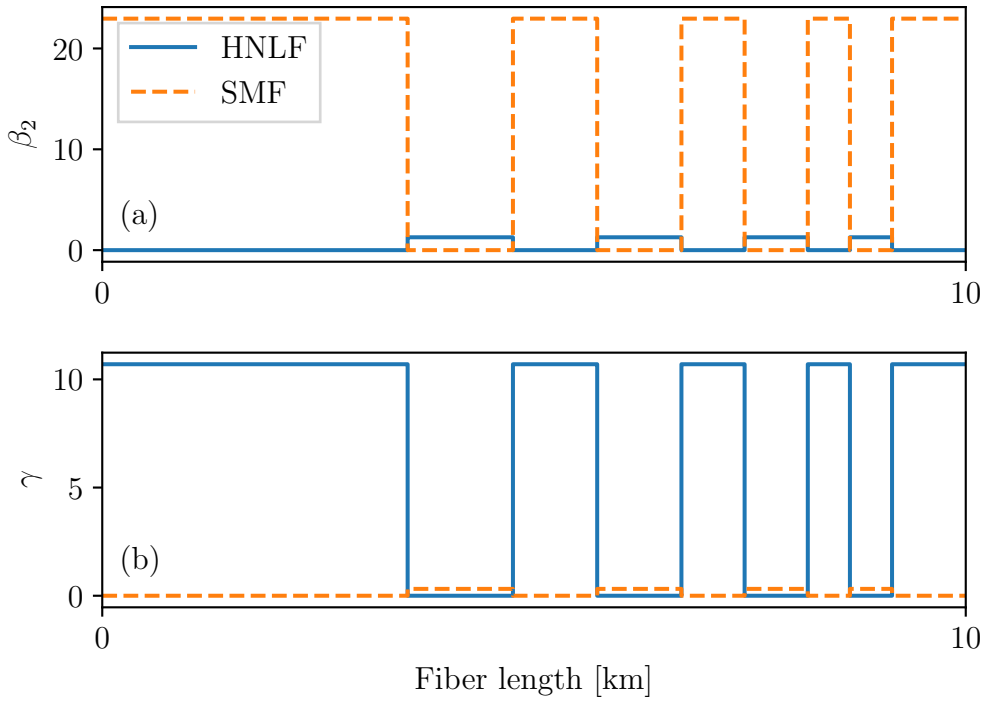

Figure 2.3: CPF dispersion and nonlinearity profile along the fiber (a) Second-order dispersion profile; (b) Nonlinearity profile

a DDF, but leads to more complex behaviours, depending on the lengths of the HNLF, as is noted by Inoue et al.[18].

Distributed Raman amplification

From Equation (2.1), it is possible to see that similarly to Section 2.1.1 in which we decrease the dispersion of the overall fiber, it is also possible to increase the nonlinear parameter along the fiber, namely ν, where $\nu(z) = \exp(-\alpha z)\gamma(z)$ with $\alpha < 0$, meaning a gain is introduced in the fiber. Distributed Raman amplification will create a gain factor, leading to the compression of the pulse[43,44].

Parametric amplification

Another possible way of pulse compression is to exploit FWM. This technique was demonstrated experimentally by Wiberg et al.[31]. A first pulse train was generated by modulating a CW laser through a Mach-Zender Modulator (MZM) modulated by a beat signal at its quadrature point. These pulses were then first compressed through spectral broadening by SPM generated through the propaga-

tion in a HNLF down to 2.58 ps after filtering of the spectrum in order to get pulses that are transform-limited. In order to further compress the pulses, and reduce the small pedestals created after the SPM compression, a CW seed was added through Wavelength-Division Multiplexing (WDM). This allowed the creation of an other spectral band through parametric amplification. While the high-power parts of the pulse will be replicated on the newly created spectral band, the low-power features, such as pedestals will not, thus filtering them out. Similarly, the low-power part of the pulse itself will not be replicated, leading to further compression of the pulses. Wiberg et al.[31] demonstrated a compression factor around 20 using this method, creating pulse-free pedestals, and a factor 2 was also demonstrated by Feng et al.[45].

Multiple Four-wave mixing

As was shown by Trillo et Al.[24], by sending a beat signal created by two CW in a fiber, it is possible through FWM to compress pulses with a very large ratio. However, this comes at a price of creating pulses with pedestals. Using this phenomenon, Pitois et al.[46] demonstrated that by carefully managing the parameters, the same method could be used to compress an initial beat signal significantly, creating gaussian pulses that are transform limited. The advantage of this method is that it can be used with a fiber having constant anomalous dispersion, and the pulse FWHM can be managed simply through the input power and fiber length. It is worth noting that using this method, the results from [24] were validated, showing that over a certain input power, large pedestals started to form, although the pulses compression ratio was higher.

2.1.2 XPM-induced reshaping principle

Multiple compression schemes have been demonstrated over the years, as shown in this section, using a large variety of effects that appear in optical fibers, such as dispersion, SPM, FWM, or parametric amplification, and specially designed fibers, with dispersion management such as DDF. Most of those techniques however are only applicable in the anomalous dispersion regime. In fact, only a few techniques have been demonstrated for normally dispersive fibers, usually including a two-stage technique, similar to the grating compression technique. However, a less exploited process combining both the nonlinear reshaping and chirp compensation stages can be provided in the defocusing regime of the NLS equation by means of a cross-phase modulation phenomenon[47–51]. Indeed, it was shown that an XPM-induced focusing of a probe beam can occur in the defocusing regime when it co-propagates orthogonally, polarized and bounded between two intense pump pulses traveling at the same group velocity[48–50]. In this configuration, in analogy

to the soliton-effect compression technique, the evolution of the dark structure generated in the center of these twin pump pulses induces an XPM-based temporal compression, even in normally dispersive fibers, thus creating an adiabatic compressor for the probe beam.

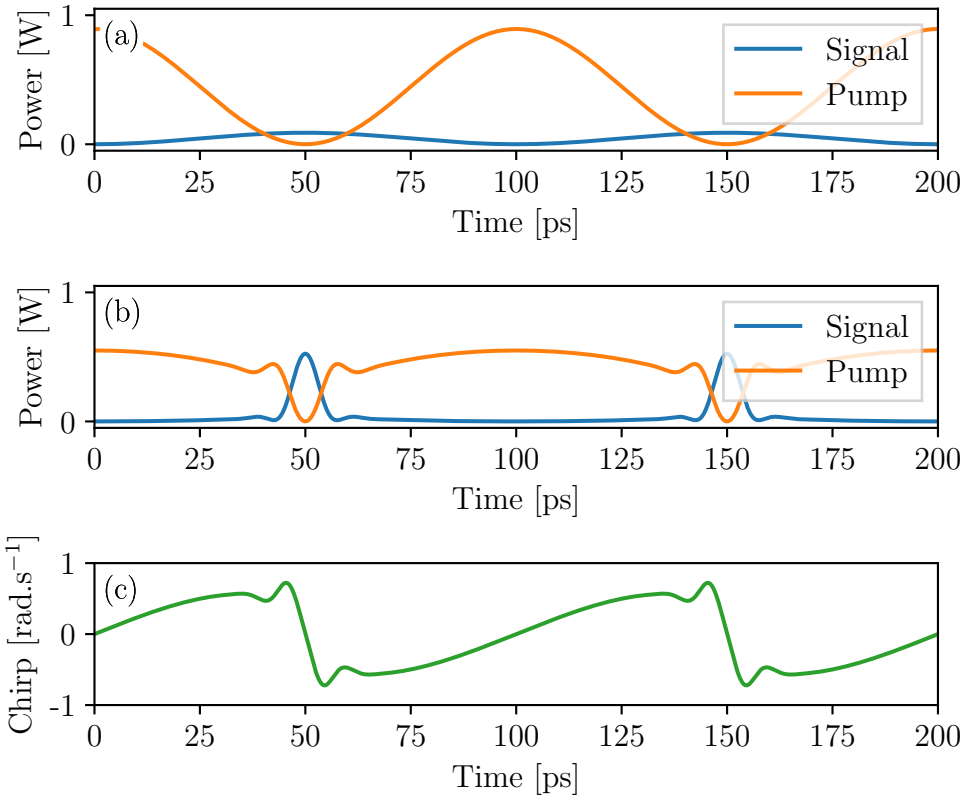

Figure 2.4: (a) Signal and pump input intensities at the input of the fiber (b) Signal and pump output intensity after propagation in a 5 km DSF for a pump power of 26.5 dBm (c) XPM-induced chirp created by the pump on the signal

The compression scheme developed in this section appears from the simultaneous combined effect of XPM and chromatic dispersion. In order to observe the compression, two waves are sent copropagating with orthogonal polarizations, the low-power beat signal to be compressed is a sinusoidal wave, and the high-power pump that induces the XPM is an out-of-phase replica with high power. The intensities of those waves is illustrated on Fig. 2.4a. Through SPM and chromatic dispersion, the pump pulses will broaden and their edges sharpen. Simultaneously, the pump induces a chirp, through XPM, on the signal, which is displayed on Fig. 2.4c. The chirp is, at the same time, canceled out in the signal pulse by

the chromatic dispersion experienced by the signal, similarly to the phenomenon that is observed in an anomalous fiber during soliton-like compression. A focusing regime is thus locally created through the XPM-induced chirp. The cancellation of the chirp thus leads to the compression of the signal. The output waves can be observed in Fig. 2.4b. Thanks to the orthogonal pump wave, the beat-signal is now compressed into a train of well-separated pulses.

2.1.3 Experiment

In order to observe this effect, a setup was designed to generate, propagate and observe the orthogonal waves, as illustrated in Fig. 2.5. The first operation that needed to be achieved was to generate the two interleaved orthogonally polarized sinusoids. For this, a CW laser emitting at 1550 nm is first modulated in intensity to create a sinusoidal signal using a Intensity Modulator (IM) driven at its null point by a 20 GHz clock to create a pure 40 GHz carrier-free sinusoid.

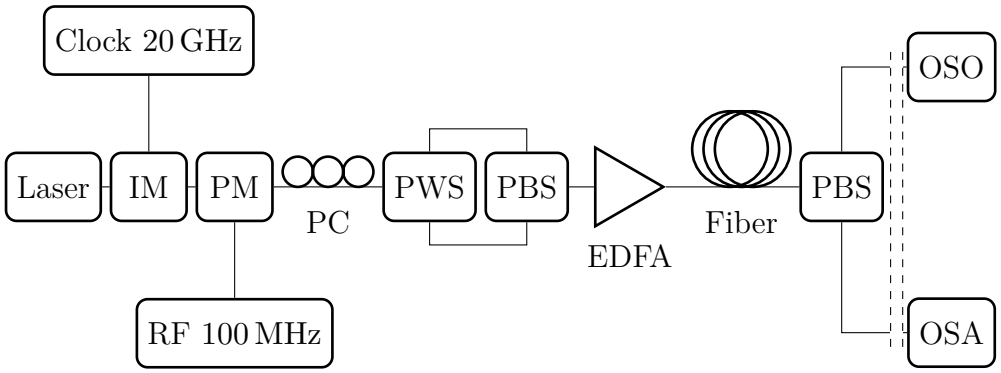

Figure 2.5: Schematic experimental setup designed to create a 40 GHz pulse source. IM: Intensity Modulator, PM: Phase Modulator, RF: Radiofrequency generator, PC: Polarization Controller, PWS: Polarization WaveShaper, PBS: Polarization Beam Splitter, EDFA: Erbium-doped Fiber Amplifier, OSO: Optical Sampling Oscilloscope, OSA: Optical Spectrum Analyser

When looking at the transmission curve of a typical IM (Figure 2.6), it can be seen that setting the bias voltage in a null-point, meaning the point of lowest optical output, of this curve will lead to generate an optical peak for each high and low of the sinusoidal input beat signal, thus doubling the frequency of the input optical signal. It should be noted that each output optical pulse is dephased by 180° compared to the previous one.

This signal is then phase-modulated at a frequency of around 100 MHz in order to reduce Brillouin back-scattering in the fiber under test. As was demonstrated in[19], phase modulation of a signal is equivalent to changing the frequency

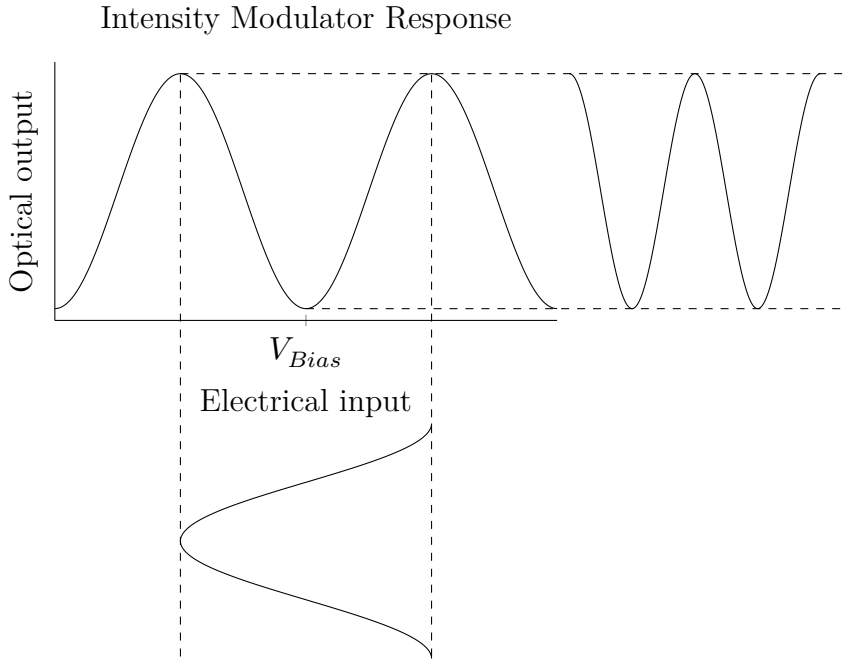

Figure 2.6: Carrier suppressed RZ principle of operation

of maximum gain of the Brillouin back-scattering, thus enlarging the Brillouin back-scattering gain bandwidth. Having a larger spectrum then leads to a decrease of the Brillouin peak gain defined as

$$g_p = g_B(\Omega_p) = \frac{4\pi^2\gamma_e^2 f_A}{n_p c\lambda_p^2 \rho_0 \nu_A \Gamma_B} \tag{2.2}$$

where $\gamma_e \approx 0.902$ is the electrostrictive constant of silica, f_A the fraction by which the Brillouin back-scattering gain is reduced if the acoustic and optical modes do not fully overlap, n_p is the effective index at the pump wavelength λ_p, $\rho_0 \approx 2210\,\mathrm{kg\,m^{-3}}$ is the material density, ν_A the acoustic wave velocity. The FWHM of the gain spectrum is linked to Γ_B with the relation $\nu_B = \Gamma_B/(2\pi)^2$. By reducing the peak gain, the Brillouin back-scattering power threshold P_{cr} can be reduced, which can be approximated for fibers not too long by

$$g_B(\Omega_B) P_{\mathrm{cr}} L_{\mathrm{eff}}/A_{\mathrm{eff}} \approx 21 \tag{2.3}$$

where $L_{\mathrm{eff}} = [1 - \exp(-\alpha L)]/\alpha$ is the effective fiber length and A_{eff} is the effective mode area[2]. The increased threshold is enough for the experiments that are conducted in the following parts.

The resulting signal is then injected into a Polarization WaveShaper (PWS) separating the input signal into two signals, and allowing to control characteristics

of the signals, like amplitude and delay, independently. The delay on each branch can go up to 12.5 ps, and allows for a fine tuning of the signals interleaving. It must also be noted that the power difference in between the two signals was set to 11.5 dB on the PWS. Those signals are then recombined into a Polarization Beam Splitter (PBS), ensuring an orthogonal polarization in between them. The resulting waves are then amplified through an Erbium-doped Fiber Amplifier (EDFA), allowing for high power transmission, and precise control over the power, before being injected into a 5 km-long normal dispersion fiber, characterized by a chromatic dispersion $D = -2.5\,\mathrm{ps\,nm^{-1}\,km^{-1}}$ at 1550 nm (second-order dispersion $\beta_2 = 3.2\,\mathrm{ps^2\,km^{-1}}$), an attenuation factor of $\alpha = 0.2\,\mathrm{dB\,km^{-1}}$ and a nonlinear Kerr coefficient of $\gamma = 1.7\,\mathrm{W^{-1}\,km^{-1}}$. This particular fiber was used as it was the fiber with the optimal parameters at a pump power input of 28 dBm, giving the best square shaped pump at the output. After propagation, the two waves are demultiplexed using a second PBS and characterized temporally using and Optical Sampling Oscilloscope (OSO) (eye-checker from *Alnair Labs*), and spectrally using an Optical Spectrum Analyser (OSA).

Fig. 2.7 displays the normalized signal and pump demultiplexed after the output PBS for an input pump power of 26.5 dBm. Compression of the signal pulses, broadening and wave-breaking of the pump pulses can be observed clearly. On the signal output, the intensity is not perfectly driven down to zero outside the pulses, leaving small pedestals at the edges of the created pulses.

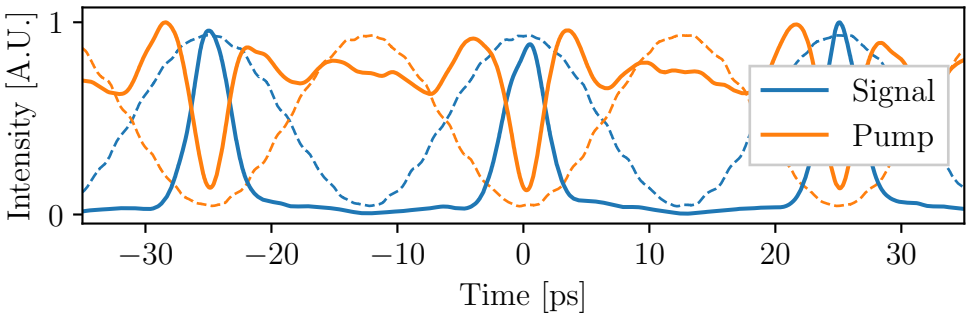

Figure 2.7: Interleaving of the pump and signal waves at a power of 26.5 dBm, normalized. Dashed: Input, Solid: Output

Power study

We first study the impact of the total input power, keeping the power ratio between the pump and the signal at 11.5 dB, as previously described. Each output polarization axis is independently measured, for input powers ranging from 12 dBm to

26 dBm. The results are summarized in Fig. 2.8. Fig. 2.8a displays the evolution of the normalized signal pulses with increasing power, while Fig. 2.8b displays the evolution of the normalized pump pulses.

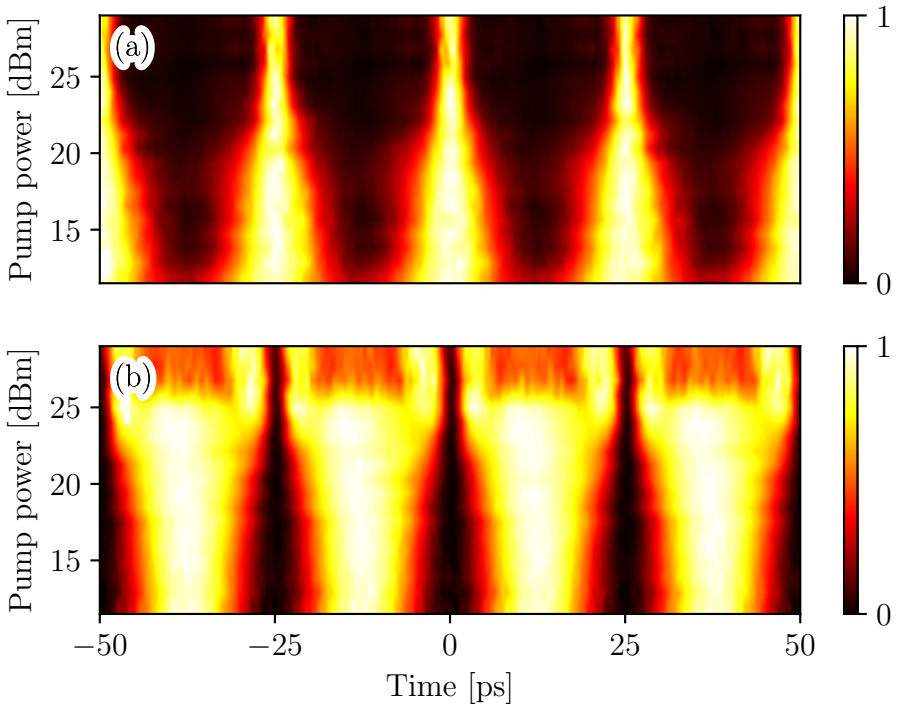

Figure 2.8: Experimental results (a) Evolution of the normalized signal pulses with pump power (b) Evolution of the normalized pump pulses with pump power

At low power (around 12 dBm), in the *linear* regime, it was observed that the sinusoids keep their shape during propagation. At these power levels, no nonlinear effect appear during propagation, hence the name of linear regime. However, when increasing the input power and getting into the *nonlinear* regime, it can be observed that the pump starts widening, and its pulses edges are getting sharper. It is interesting to note that the signal pulses power evolution follows the evolution of the dark structures created between the pump pulses. When their power increases, the pump pulses broaden through SPM and dispersion. This leads to the spacing between two pulses gradually reducing[52]. At the same time, the signal is getting compressed, confined in between the edges of the pump pulses. At 25 dBm, we observe the maximum compression, with the generation of 3.3 ps FWHM pulses. It can be noticed that when this power is reached, increasing the power does not further compress the signal pulses. It also does not significantly reduce the spacing

between two pump pulses which would lead to further compression of the signal. Finally, one can notice the apparition of interaction between adjacent pulses on the pump signal. At the maximum level of total input power, 28 dBm, the level of Brillouin back-scattering becomes a severe limitation for the experiments, so the study stopped at this maximum power.

2.1.4 Simulations

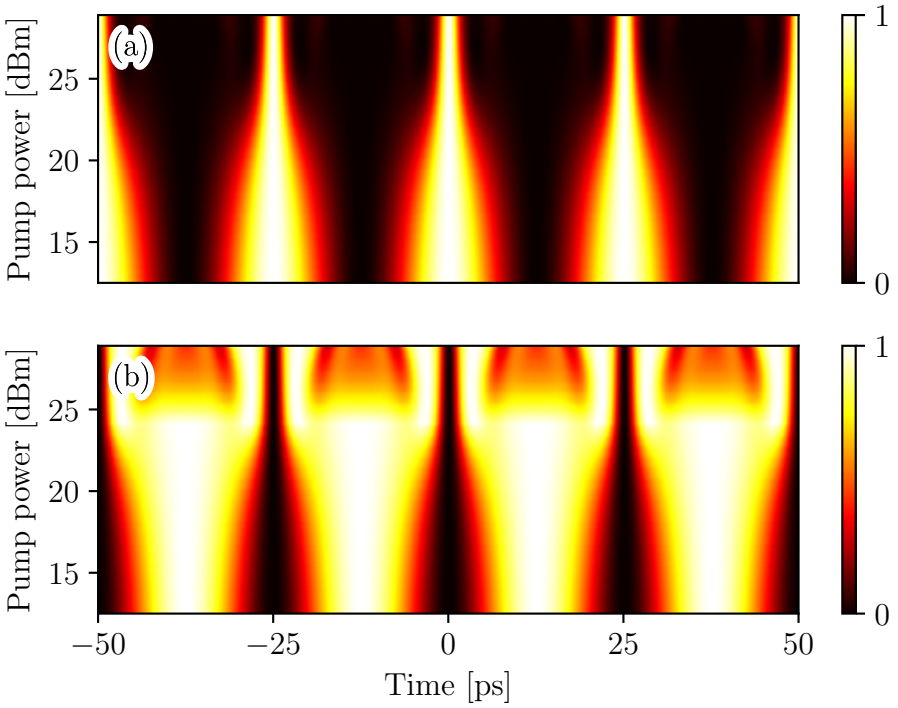

Figure 2.9: Numerical simulation results. Temporal intensity profile evolution in the numerical study as a function of pump power of the pulse generation using the Manakov model (pump + signal) (a) Evolution of the signal with the pump power (b) evolution of the pump with the pump power.

To validate and further explore the compression phenomenon, numerical simulations of the propagation of the two orthogonal waves were performed. While the Manakov model (Eq. (1.19)) can be used to simulate this system, the large power difference between the signal and pump waves allows to simplify the equations. Indeed, this large difference translates, mathematically, to $|u|^2 \ll |v|^2$. By taking

this relation into account, Eq. (1.19) can be rewritten as

$$\begin{aligned} i\frac{\partial A_+}{\partial z} + i\frac{\alpha}{2}A_+ - \frac{\beta_2}{2}\frac{\partial^2 A_+}{\partial t^2} + \frac{8}{9}\gamma\left|A_-\right|^2 A_+ = 0 \\ i\frac{\partial A_-}{\partial z} + i\frac{\alpha}{2}A_- - \frac{\beta_2}{2}\frac{\partial^2 A_-}{\partial t^2} + \frac{8}{9}\gamma\left|A_-\right|^2 A_- = 0 \end{aligned} \tag{2.4}$$

where A_+ corresponds to the signal wave, A_- to the pump wave, A_+ and A_- being the two orthogonal components of the total optical wave. $\beta_2 = 3.2\,\mathrm{ps}^2\,\mathrm{km}^{-1}$ is the dispersion coefficient of the fiber, $\gamma = 1.7\,\mathrm{W}^{-1}\,\mathrm{km}^{-1}$ is the nonlinear Kerr coefficient, and $\alpha = 0.2\,\mathrm{dB/km}$ is the losses coefficient. In these equations, it can be noticed that there is a coefficient 8/9 that is not present in Eq. (1.19). This coefficient appears out of the averaging of the birefringence on the length of the fiber during the derivation of those equations[53], allowing for a more realistic simulation. While the development of this new model offers little advantage compared to the Manakov model in regards to simulation time, it allows for the development of the theoretical model demonstrated in Section 2.1.5.

First, the full model was simulated so that comparison with the reduced model can be made. The results of such a simulation are shown on Fig. 2.9. On this figure, the results obtained are very close to the experimental results obtained on Fig. 2.8.

Figure 2.10 displays the evolution of the signal and pulse waves with input pump power after simulation. As expected, it is almost identical to the evolution of the signal simulated using the full Manakov model displayed in Fig. 2.9. Fig. 2.10a displays the evolution of the normalized signal pulses with power, while Fig. 2.10b shows the orthogonal pump pulses. Similarly to the results obtained Section 2.1.3, compression of the signal pulses is shown to increase with pump power, and the evolution of the signal pulses follows the evolution of the pump dark structures. The compression is shown to have a limit at around 25 dBm, which is also the threshold above which we start to observe interaction between adjacent pump pulses.

The numerical results obtained are very similar to the ones obtained in Fig. 2.8, thus validating the experiment, and proving that the compression effect is effectively coming from an XPM-induced chirp. They also validate the Manakov-based model that was explicited, in which the contribution of the signal probe in the nonlinear effects was neglected. Finally, it validates the assumptions that Raman effect and third-order dispersion have no effect in this compression mechanism, as both those elements were neither included in the equations, nor in the simulations.

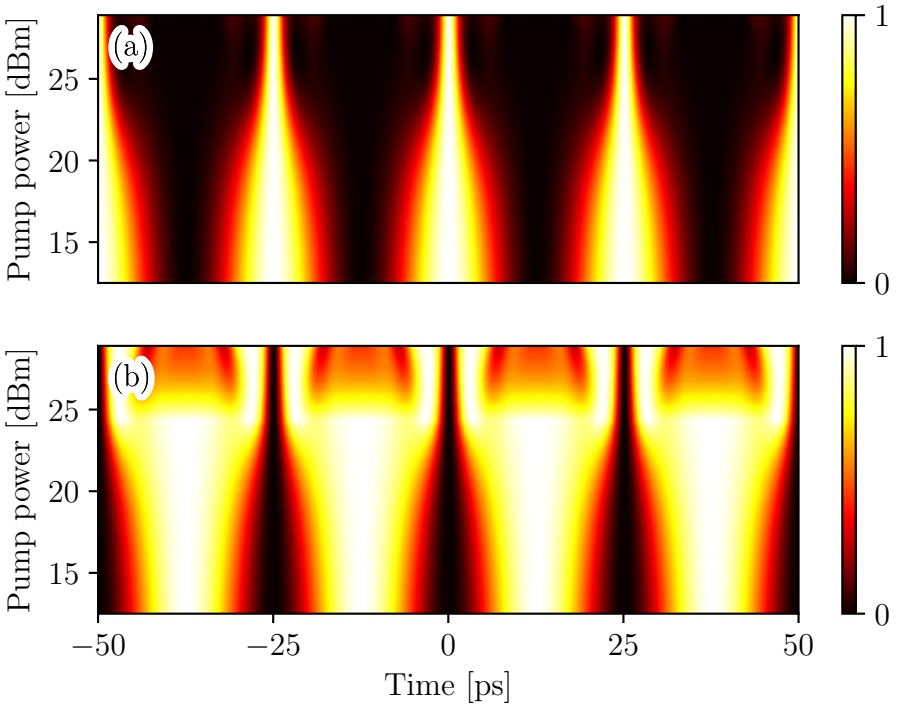

Figure 2.10: Same as Fig. 2.9, but using the reduced model

2.1.5 Theoretical model

By creating a reduced model, a numerically simple solution could be designed, removing the need to fully solve the numerical model, and allowing extremely fast approximations of the solutions. First, the input pump and signal can be rewritten from their initial form.

$$A_+(0,t) = (2S)^{1/2}\sin(\omega_1 t) \tag{2.5}$$

$$A_-(0,t) = (2P)^{1/2}\cos(\omega_1 t) \tag{2.6}$$

It can be noticed that writing A_+ and A_- this way leads to $\langle|A_+|^2\rangle = S$ and $\langle|A_-|^2\rangle = P$ where P and S represent respectively the pump and signal power. By rewriting the sin and cos in exponential form, the following form is obtained

$$A_+(0,t) = -i\frac{S}{2}^{1/2}\exp(i\omega_1 t) + i\frac{S}{2}^{1/2}\exp(-i\omega_1 t) \tag{2.7}$$

$$A_-(0,t) = \frac{P}{2}^{1/2}\exp(i\omega_1 t) + \frac{P}{2}^{1/2}\exp(-i\omega_1 t) \tag{2.8}$$

The four-wave mixing between frequency components centered at $\pm\omega_1$ leads to the generation of new frequencies at odd multiples of ω_1, in both the pump and the signal wave. To create this theoretical model however, the generation of new frequencies in the pump wave are neglected. This assumption can coherently be made, as the first sideband observed both experimentally and numerically in the spectrum of the pump are always 10 dB below the central bands. By making this approximation, it is now possible to write a simple form of $|A_-(z,t)|^2$

$$|A_-(z,t)|^2 = |A_-(0,t)|^2 = P + \frac{P}{2}\exp(i2\omega_1 t) + \frac{P}{2}\exp(-i2\omega_1 t) \tag{2.9}$$

On the other hand, it is not possible to neglect the generation of new sidebands on the signal wave. Thus, it can be written as a linear combination of components centered at odd multiples of ω_1

$$A_+(z,t) = \sum s_n(z)\exp(i\omega_n t) \tag{2.10}$$

with $\omega_n = n\omega_1$ where n is an odd number.

By then inserting the expressions of $|A_-(z,t)|^2$ and $A_+(z,t)$ in Eq. (2.4), we obtain a system of coupled Linear Differential Equations (LDE)

$$s_n : \frac{\partial s_n}{\partial z} = (ia_n - \alpha/2)\, s_n + ib\,(s_{n+2} + s_{n-2}) \tag{2.11}$$

where $a_n = (n^2\omega_1^2\beta_2/2 + 8/9\gamma P)$ and $b = 4/9\gamma P$. This system of LDE is now solvable quickly and easily by truncating it at a finite value $n = n_c$, and knowing the initial conditions $s_1(0) = -i(S/2)^{1/2}$, $s_{-1}(0) = i(S/2)^{1/2}$ and $s_n(0) = 0$ for $n \neq \pm 1$. By evaluating the values of s_n, it is possible to directly go back to A_+, by replacing in Equation (2.10). The result of such calculation can be seen on Fig. 2.11. From the pulse thus calculated, the compression ratio can then be easily computed. It can be noted that while an increased number of n will increase the precision of the results, a value of $n_c = 9$ is sufficient to give a good approximation of the end result. If the spectrum is to be calculated from this method, the assumption of the pulses being in Fourier Transform Limit (FT Limit), allowing then to simply calculate the FT of the signal and obtaining directly the spectrum.

2.1.6 Comparison between the experimental, numerical and theoretical results

After studying the process of pulse generation through XPM-induced compression experimentally, numerically and theoretically with the model developed in Section 2.1.5, the overall results were analyzed.

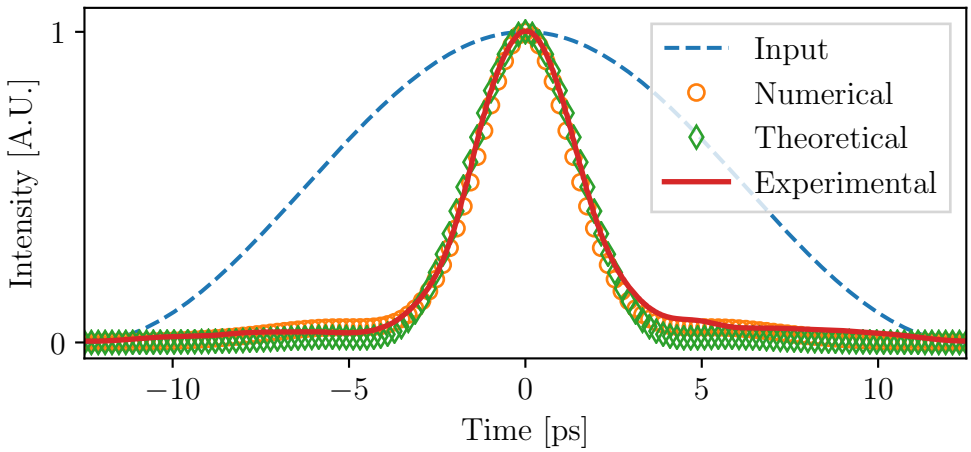

Figure 2.11: Comparison of the pulses obtained experimentally, numerically by simulation of the propagation using Eq. (2.4) and theoretically using the model developed in Section 2.1.5.

As can be observed on Fig. 2.11 illustrating the generated compressed pulses at the output of the fiber, there is a good agreement between the experimental, numerical and theoretical data. The generation of 3.3 ps FWHM well-separated pulses can be observed, with a small residual pedestal.

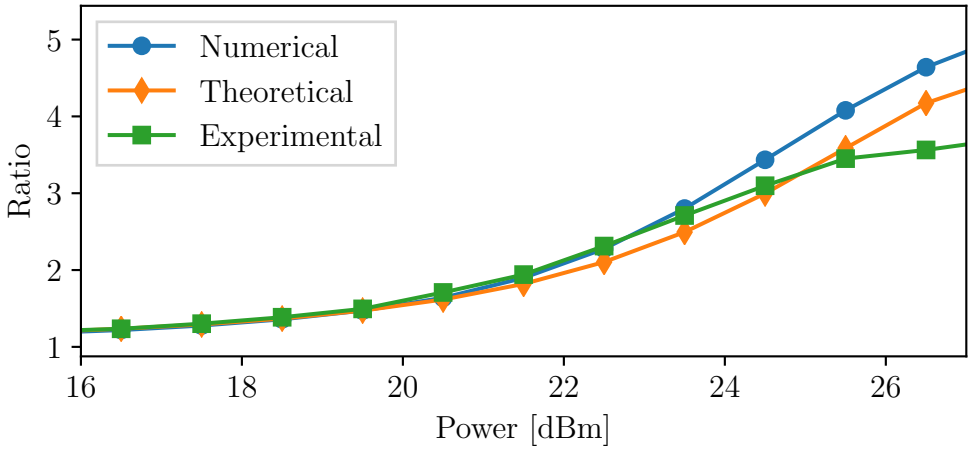

Figure 2.12: Compression ratio comparison between the experimental, numerical and theoretical methods, depending on the power input

The compression ratios obtained experimentally, numerically and theoretically for each input pump power were measured by fitting a gaussian pulse on the output

pulses, and their evolution were plotted on Fig. 2.12. A good agreement can be observed between the experimental and calculated ratios, although around 25.5 dBm, the experimental compression ratio increase slows down, due to Stimulated Brillouin Back-scattering (SBS) limiting the pump power, thus the nonlinear effects. Moreover, even though strong simplifications were made during the creation of the theoretical model, in particular the conservation of the pump spectrum, it is showed to allow for a good approximation of the end result. At 26.5 dBm of pump power, a compression ratio around 3.5 was observed.

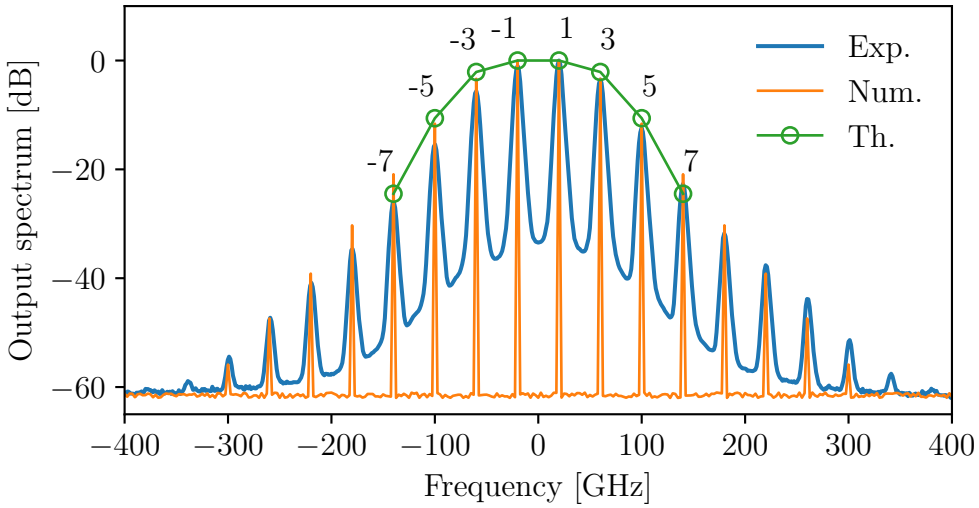

Figure 2.13: Normalized spectrums after propagation in the fiber for the experimental, numerical and theoretical methods, with the n value of the peaks (Eq. (2.11)).

The output spectrum was also observed experimentally by placing an OSA after the output PBS, as depicted in Fig. 2.5, and is displayed on Fig. 2.13. The theoretical spectrum was also computed by assuming the output pulses are FT Limit and taking the Fourier transform of the output temporal signal computed previously. Such an assumption can be made as the time-bandwidth product was calculated to be around 0.58 which is not too far from the value of the FT Limit gaussian pulse at 0.44, and by remembering that the pulses obtained are not exactly gaussian. It can be noticed that the experimental spectrum has a higher background than the numerical value, which is due to a limitation in the resolution of the OSA (resolution of 0.01 nm) that was used for the experiment. As observed on Fig. 2.13, there is a good agreement between the experimental and numerical spectrum, confirming the assumptions made during the derivation of Eq. (2.4). Finally, the theoretical spectrum is displayed by plotting the different

s_n at the frequencies ω_n obtained after solving Eq. (2.11). The theoretical model appears to yield a very good approximation of the results for $n_c = 7$, confirming further the validity of the model developed in Section 2.1.5.

2.1.7 Limitations

From Fig. 2.8, Fig. 2.10 and Fig. 2.12, limitations on the pulse generation can be observed. First, the saturation of the compression ratio will be studied, and the effects of SBS and inter-pulses interactions will be explicited. Possible methods to overcome the pulse compression limit will then be applied numerically and their results compared. Fig. 2.12 made clear that small pedestals appear during the compression of the input signal pulses. After introducing the origin of those pedestals and the issues that could arise from them, their evolution with power will be quantified, and methods to remove such pedestals will be discussed. Finally, the effects of a bad temporal alignment of signal and pump at the input of the fiber will be studied, and its impact on the compression ratio and side pedestals explicited.

Pulse compression saturation

It can clearly be seen on Fig. 2.12 that the experimental compression ratio saturates with an increase in power, while the numerical and theoretical ratio keeps going up. The simulated results indeed did not take into account the power reductions of the pump pulse due to SBS, thus enabling higher SPM and XPM interactions due to higher power. The phenomenon of SBS was experimentally reduced by introducing a phase modulation of the pump but cannot be completely removed. It however allowed for a study at much higher pump powers with negligible SBS, up to 28 dBm.

However, it was observed on Fig. 2.8 and Fig. 2.10 that when inter-pulse interaction between pump pulses appears[52], the pulses compression is reduced. To observe the effects of these interactions, a study was realized numerically at higher pump power. Fig. 2.14 shows the evolution of the signal and pump at higher powers. It can be noticed on Fig. 2.14a that the central pulse tends to be more and more compressed, but that it undergoes some oscillations of its width, depending on the shape of the pump pulses, which divide in multiple pulses, as can be seen on Fig. 2.14b. Moreover, Fig. 2.14a shows the apparition of multiple pedestals around the central pulse, which is confirmed by the signal intensity profile at fiber output plotted on Fig. 2.14c. It can also be observed that for some powers, the central peak on the signal disappears and is replaced by multiple peaks with the same power, as can be seen on Fig. 2.14f in which the signal intensity profiles are plotted for pump powers giving an output with 1 pulse with very low pedestals

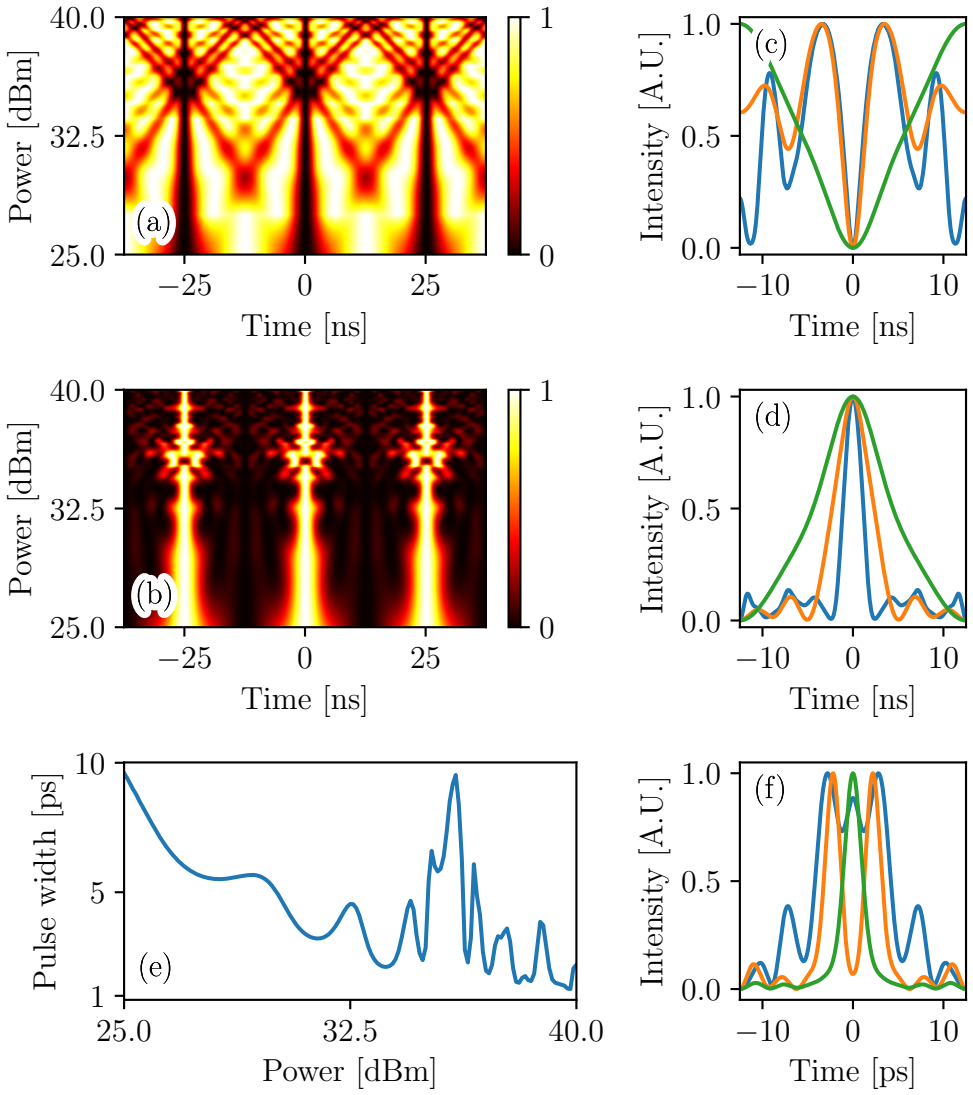

Figure 2.14: Numerical evolution of the signal and pump waves at higher power (a) Pump pulses evolution with power (b) Signal pulses evolution with power. (c) Pump profile at 25 dBm, 32.5 dBm, 40 dBm (d) Signal profile at 25 dBm, 32.5 dBm, 40 dBm (e) Width of the gaussian fit applied to the signal pulses (f) Multiple signal pulses created. Green: 34 dBm, orange: 35.5 dBm, blue: 35.9 dBm

(34 dBm), 2 pulses with a dark structure in the center (35.5 dBm) and a pulse which shows flattening of its top (35.9 dBm). Finally, Fig. 2.14e shows the gaussian fit of the center pulse. While the output signal pulse are obviously not gaussian for

some powers, fitting the output pulses this way allows to observe a reduction of the minimum width of the pulses for appropriate powers when a single pulse is created and very low power sidebands are created. Indeed, pulse width down to around 1.3 ps are observed for a pump power of 38.8 dBm, meaning a compression ratio around 9.6.

Inter-pulse interactions are indeed limiting the compression by creating signal pulse shapes that were not planned, such as double pulses or pulses with a flattened top. However, with increasing pump power can appear well-defined signal pulses with lower width, thus increasing the compression ratio. It must finally be noted that while those interactions introduces new behaviour in this system, the SBS and Raman scattering generated from the high pump powers used for this simulation would make such a system difficult to implement experimentally.

Pulses pedestal

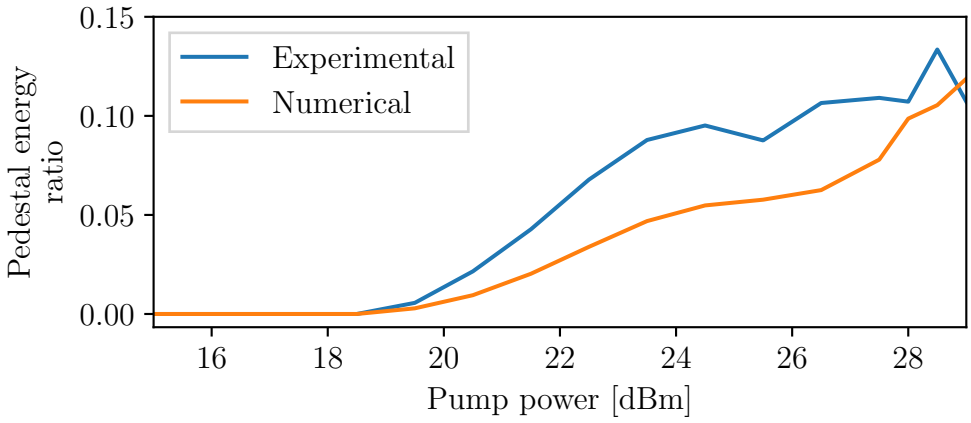

Figure 2.15: Evolution of the energy contained in the pedestals with pump power.

As can be seen on the results of simulations on Fig. 2.10, still have pedestals remaining after compression. Even if they are not observed on the experimental data as clearly, those pulse are still generated during the compression. Such pedestals can provide some impairment due to intersymbol interference and lead to transmission errors in telecommunication systems, such as in Optical Time-Division Multiplexing (OTDM), and also create compressed pulses with lower peak power[18]. In this paragraph, their evolution with power is thus monitored on the experimental and numerical data by calculating the ratio of the pulse energy they contain.

By fitting a gaussian on the experimental and numerical pulses, the energy

contained in the pedestals can be evaluated using the formula

$$\text{ratio} = 1 - \frac{E_{\text{fit}}}{E_{\text{data}}} \tag{2.12}$$

where E_{fit} is the energy contained in the gaussian fit and E_{data} is the energy of the experimental or numerical data, and by setting ratio = 0 if the ratio calculated is negative. By fitting the pulses for each input pump power, the evolution of the pedestals energy can be plotted, and is displayed on Fig. 2.15. It can be observed that while not apparent on the experimental map of the signal pulse evolution in Fig. 2.8a, pedestal do appear in the experimental case, and the energy contained in them is even larger than during the simulation, where the pulse evolution maps clearly displayed their apparition (Fig. 2.10).

As is observed on Fig. 2.15, the energy in the pedestals quickly reaches 10% of the total, which is not negligible. In order to improve the generated pulses, a pedestal removal method can be used, such as described by Mamyshev[54] using SPM, Wiberg et al.[31] using parametric amplification or Pelusi et al.[55] using a nonlinear optical loop mirror. By employing nonlinear effects generating the pulses at different wavelength, only the higher power pulses are mirrored on the generated spectrum. By filtering on the newly generated band, the pulses are retrieved, their pedestals having been filtered out, as they do not have enough power for the nonlinear effect to be significant over their time frame. However, it must be noted that such filtering adds one further step in the pulse generation process and may create additional pulse train instability and timing jitter[56].

Asymmetrically modulated input signals

The interleaving of the signal and pump was also observed to have a significant impact on the generated signal pulses. A slight temporal misalignment of the input waves can indeed have a visible impact at the output of the fiber, destroying the symmetry of the output pump and signal. To demonstrate the impact of this effect, the waves were simulated copropagating with different modulation phase shifts, for a power of 26.5 dBm. It was possible to obtain the approximate width of the output signal main pulses, and by calculating the difference of energy between the simulation and the fitting, obtain the ratio of energy that is found in the pedestals.

As shown in Fig. 2.16a, the signal pulses after propagation with an asymmetry in the alignment of the signal and pump change in shape, the pedestals increasing on one side of the pulse, and their peak power decreasing significantly, while the pump stays unaffected by the change, as seen on Fig. 2.16b. By fitting a gaussian to the signal pulses, their width was approximated and is evolution with phase plotted on Fig. 2.16c, where it is clearly seen that the pulse width of the signal increases with the phase, thus leading to reduced compression of the pulses. Finally,

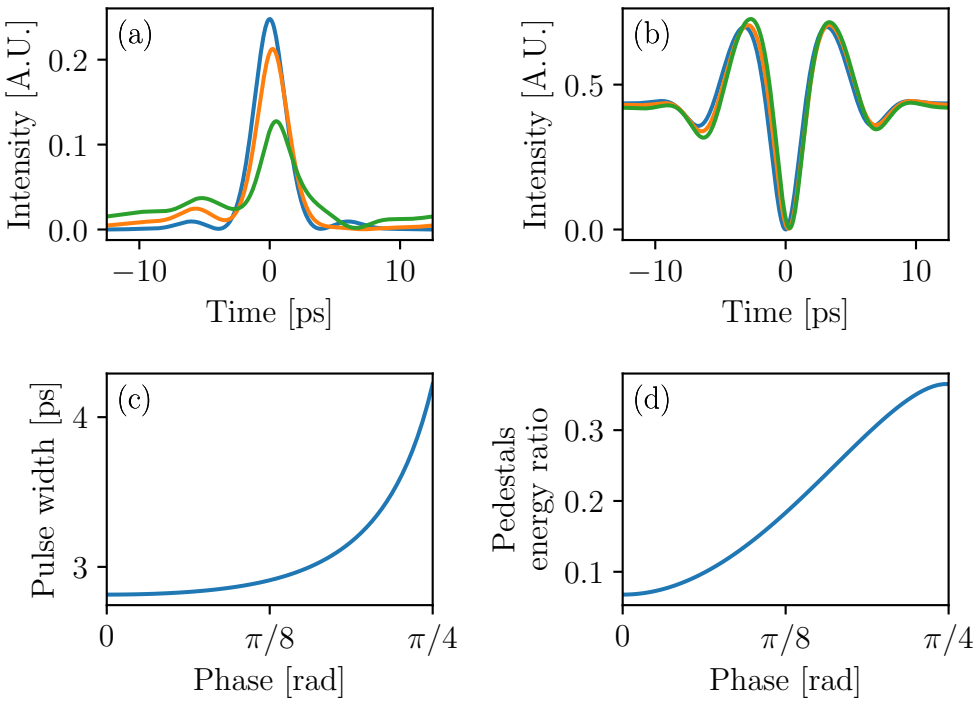

Figure 2.16: Numerical evolution of the pulses with increasing asymmetry between the input signal and pump (a) Signal pulse shape after propagation with an asymmetry of 0 rad (blue), $\pi/8$ rad (orange), and $\pi/4$ rad (green) (b) Pump pulse shape for the same asymmetry values (c) Evolution of the width of the gaussian fitted to the pulses (d) Evolution of the pedestal energy ratio

the pedestal energy ratio was calculated, using the fitted gaussian as the central pulse, and is seen to increase on Fig. 2.16d, thus decreasing the quality of the compressed pulse.

2.2 All optical sampling

In modern photonic systems, the sampling process has widespread applications in the fields of optical communications, metrology, clocking, sensing, spectral comb or arbitrary waveform generation. In this context, nonlinear effects have been demonstrated as potential key technologies to develop all-optical sampling devices[57–70]. In most of these techniques, a train of ultrashort pulses acts as an optical gate and the basic physical phenomena under use include FWM[66], XPM[67], nonlinear polarization rotation[69] or Raman soliton self-frequency shift[70]. On the other hand, signal amplification is also a critical function in many area of physics. Basically, optical amplification process refers to multiply an incident signal by increasing its global energy through an active gain medium pumped by an external pump beam. The large range of current and mature amplification techniques at telecommunication wavelengths involves Erbium doped fiber amplifiers, Raman-based amplifiers, semiconductor amplifiers or parametric processes. However, it is noteworthy that most of these techniques lead to an inherent degradation of the signal-to-noise ratio induced by the detrimental spontaneous emission of photons. Azaña and coworkers have suggested and experimentally validated a different scenario in which a linear redistribution of energy into a periodic pulse train through the self-imaging Talbot effect can lead to a noiseless amplification process[71], in which the peak pulse power increases, but the pulse energy stays the same.

In this section, an alternative approach is developed, allowing for the simultaneous sampling and magnification of an arbitrary shaped signal. This new method is based on the focusing effect that was explored previously in Section 2.1. After having provided an overview of the already existing sampling methods, the principle of operation of this method will be detailed. Simulations will be performed using the same modified Manakov model as in Section 2.1 to get a first observation of the effect and better insights on the phenomenon. From these simulations, a theoretical model is developed, in the same way as in Section 2.1, allowing for the fast calculation of an approximation of the result. To validate both models, experimental data is gathered. The magnification factor of the incoming signal after sampling is then studied by varying the pump power and monitoring its evolution. Finally, a conclusion will be drawn on the sampling system.

2.2.1 Examples of optical sampling techniques

In order to observe ultra-fast optical signals, it has been necessary to develop new methods. Indeed, the electronic components are limited to a bandwidth around 100 GHz (pulse width around 10 ps), while short optical pulses (below 1 ps) are now commonly used. One of the methods that was developed to respond to this problem was the optical sampling of those signals.

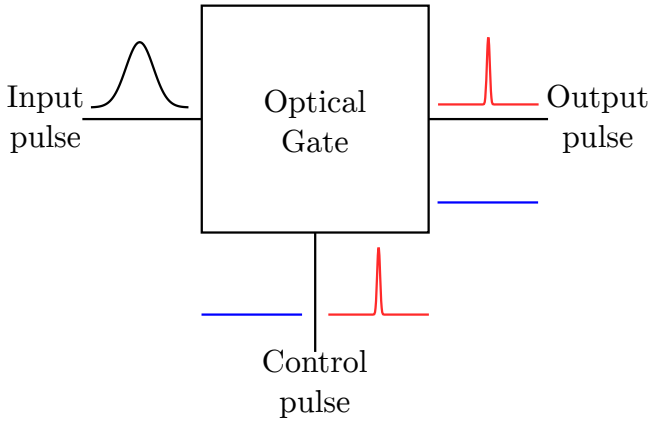

Figure 2.17: Principle of operation of an optical gate. When the control pulse is present with the input pulse, an output pulse is formed, its peak power being proportional to the pulse intensity at the control pulse time.

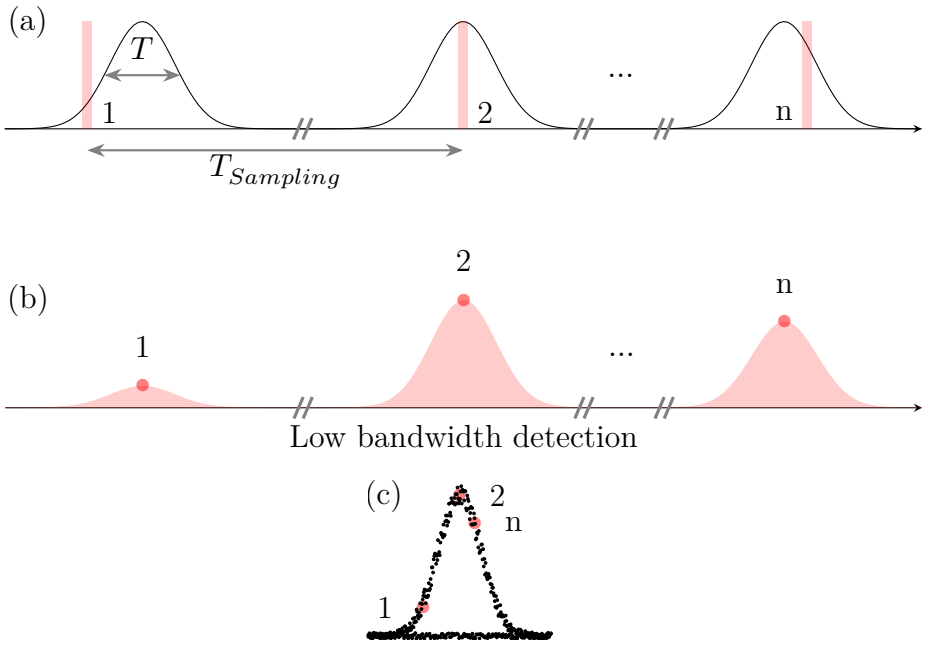

Figure 2.18: Signal sampling. The sampling window moves through the signal window, to get the signal intensity for each point

To better observe a signal, it is possible to only observe it at given times, if the signal is periodic, and repeat the operation on the next incoming pulses. By compiling all those observations, it is possible to reconstruct the shape of the incoming signal. This operation is called sampling. To do this, the receiver only

gets a signal which is proportional to the input one at given times. To achieve this, an ultra-fast optical gate is used. Such a gate is opened when a pulse (the sampling signal) is given on one end, letting the signal through. This phenomenon is illustrated on Figure 2.17. Using this technique, the gate is opened at different times of the input signal window, allowing to get the intensity of the signal at this given time, as illustrated by Figure 2.18.

It can be noted that there are two main configurations used for sampling, that use different synchronization schemes of the signal wave and pump pulsed wave. Those correspond to the synchronous sampling and random sampling.

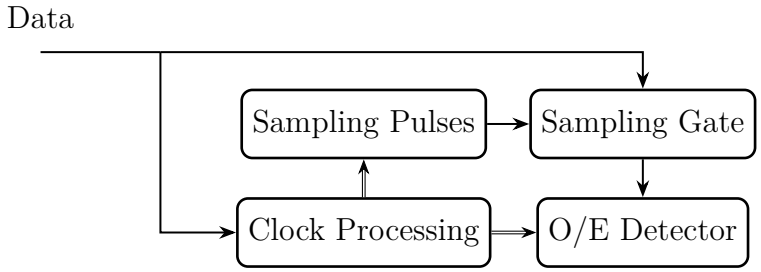

Figure 2.19: Synchronized sampling

In the case of synchronized sampling, the signal and pump are synchronized, usually using a subharmonic of the emission frequency of the signal on the pump, but with a slight offset on the pump so that it can go through the whole time window of the signal. Such a setup is illustrated in Fig. 2.19. For example, using a signal at a frequency of 10 GHz, a pump at a frequency of $50\,\mathrm{MHz} - 1\,\mathrm{Hz}$ will be used. This frequency shift is done through a clock processing setup, and the output clock is also used as a trigger for the opto-electrical detector[72]. The pump and signal emitters are also synchronized in emission. The sampling will thus be executed at given times in the signal temporal window, which is determined by the frequency offset of the pump. This sampling scheme is illustrated by Figure 2.18. In order to have a precise sampling, the frequency must then be as small as possible. However, if the offset is too small, sampling the whole time window will take a long time.

In the case of random sampling, the pump samples the signal at a random time. There is no synchronization between signal and pump, and thus no need to process the clock. In this case, the opto-electrical detector triggers on the signal, but it also receive the arrival time of the pulse source. Using this arrival time, and getting the intensity of the sample from the sampling gate, the detector is able to reconstruct the image of the signal pulse. A schematic description of the setup is illustrated on Figure 2.20. It should be noted that the arrival time detection is

crucial in this case. Indeed, if there is a time shift, it will be repercuted directly on the output, leading to errors in plotting and increased time-jitter.

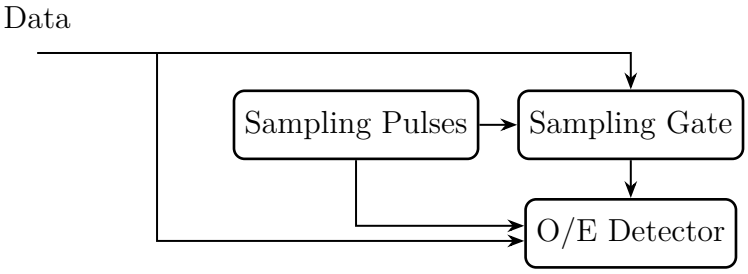

Figure 2.20: Random sampling

Now that the main principle of the sampling has been explained, different types of optical gates that have been developed will be explained. There are two main types of gates: SFG based gates, and four wave mixing gates.

Sum Frequency Generation based optical gate

The SFG is a 2nd order nonlinear effect. When sending two signals with frequencies ω_1 and ω_2 in a nonlinear material, such as a $LiIO_3$ crystal, and under specific conditions, a third signal will be created, with a frequency $\omega_3 = \omega_1 + \omega_2$ [73]. This phenomenon is illustrated on Figure 2.21. It should be noted that the power of the input signals must be high enough and that quasi-phase matching of the signals has to be achieved in order to get SFG

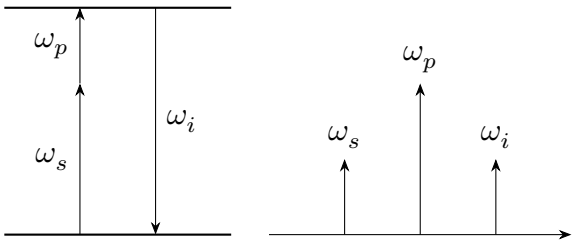

Figure 2.21: Sum frequency principle

In order to create an optical gate from this phenomenon, ω_p is used for the pump, with high power, low FWHM pulses, and ω_s is used for the signal. When an ω_p pulse is then present, an ω_i pulse can be created, and the intensity of this pulse will be proportional to the intensity of the ω_s signal at this time. With this configuration, the ω_p signal is the trigger for the optical gate, allowing signal to go through only when it is present.

This phenomenon has been studied extensively over the years[58–60,62], leading to a lot of improvements allowing for sampling of pulses with a bandwidth of 1 THz, covering the C-band and L-band[61], and has been used more recently in the detection of extreme events measurements[74].

Four wave mixing

It is also possible to create an optical gate from FWM, the phenomenon of FWM being illustrated in Figure 2.22. For this, either a Semiconductor Optical Amplifier (SOA)[75] or an optical fiber[76] can be used. In both case, a high power pulsed pump at ω_p is sent copropagating with the signal to be sampled at ω_s. The nonlinear interactions in the device (either SOA or optical fiber) creates through FWM an idler signal at a frequency of ω_i consisting of pulses intensity modulated by the input signal, allowing for measurement using slow speed detectors.

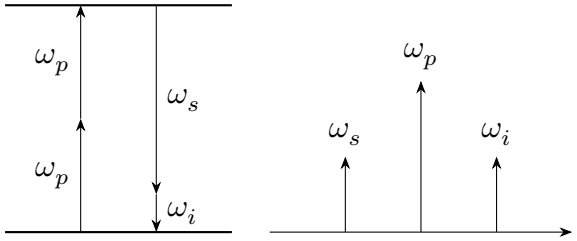

Figure 2.22: FWM principle

It is interesting to note that it took multiple years between the discovery of this method and its actual use in optical fibers. Indeed, the early fibers did not show enough nonlinearity that the pulse would go through without dispersion deformation and generate a sufficient FWM idler, making the method impractical.[65].

2.2.2 Principle of our method

Similarly to the previous experiment Section 2.1, sampling and magnification is performed using two orthogonally polarized waves. On one axis of polarization is sent the pump, a high power high frequency sinusoidal wave. On the second axis of polarization is sent the signal, a wave with significantly lower power than the pump. The signal can be random as long as the variations of its intensity profile are slow enough and can be considered locally continuous compared to the pump. Indeed, the sampling will done at the frequency of the pump sinusoidal intensity profile, thus for the sampling to be accurate, the signal seen during the sampling time must remain approximately constant.

As illustrated in Fig. 2.23a, the pump pulses undergo reshaping during propagation through SPM and chromatic dispersion, first into parabolic pulses, then into

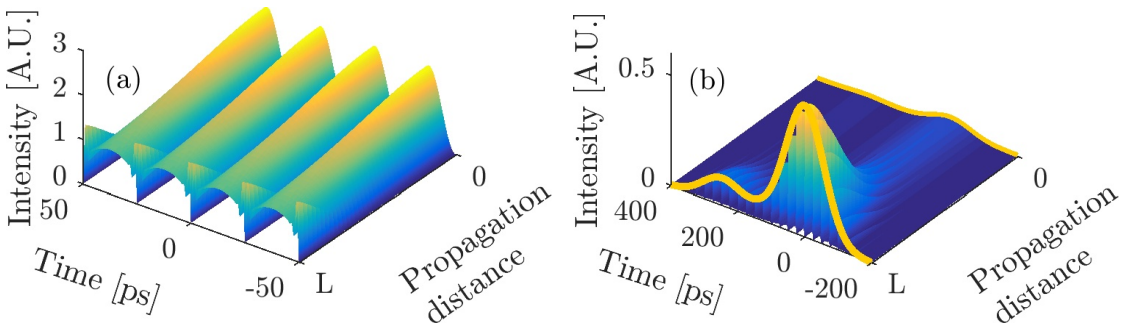

Figure 2.23: Evolution of (a) the pump (b) the signal during their copropagation in a normal-dispersion fiber. The signal is sampled and magnified, and the pump edges sharpen and create a thin dark structure between the pulses

sharp-edge square pulses, creating a small dark structure in between two pulses. Similarly to Section 2.1, a chirp is induced on the signal pulses through XPM. The combination of this chirp and the dispersion observed by the signal pulses during propagation leads to the creation of a local periodic focusing regime. The energy of the signal wave is thus attracted towards the position of the dark structures that formed in the pump wave, leading to the creation of a pulse train on the signal. The envelope of this pulse train follows the shape of the initial signal but with higher peak powers, magnifying the observable envelop. The progressive apparition of the pulse train during propagation and the magnification of the signal envelope can be observed on Fig. 2.23b. To observe the efficiency of the sampling, numerical simulation of the phenomenon were performed. Experiments using the same parameters were then carried out in order to validate the model.

2.2.3 Simulations

The phenomenon of sampling was first studied through numerical simulation using the split-step Fourier method as described in Section 1.3, using the simplified model with the equations Eq. (2.4). As a reminder, those equations were derived by introducing the assumption that the pump wave has a much higher power than the signal wave, thus neglecting the signal-induced nonlinear effects.

An arbitrary shaped weak signal is first injected into the fiber. This signal is composed of the combination of two interleaving gaussians and has an average power of 10 dBm. A second wave, the pump, is injected with an orthogonal state of polarization to the signal. This wave is a pure-sinusoidal wave with a high average power of 26.5 dBm. The fiber used for the numerical simulation was characterized by a length of $L = 5\,\text{km}$, a chromatic dispersion of $\beta_2 = 3.2\,\text{ps}^2\,\text{km}^{-1}$, a nonlinear Kerr coefficient of $\gamma = 1.7\,\text{W}^{-1}\,\text{km}^{-1}$, and a loss coefficient $\alpha = 0.2\,\text{dB}\,\text{km}^{-1}$,

which is exactly the same fiber as the one used previously. The results of these simulations are displayed on Fig. 2.24.

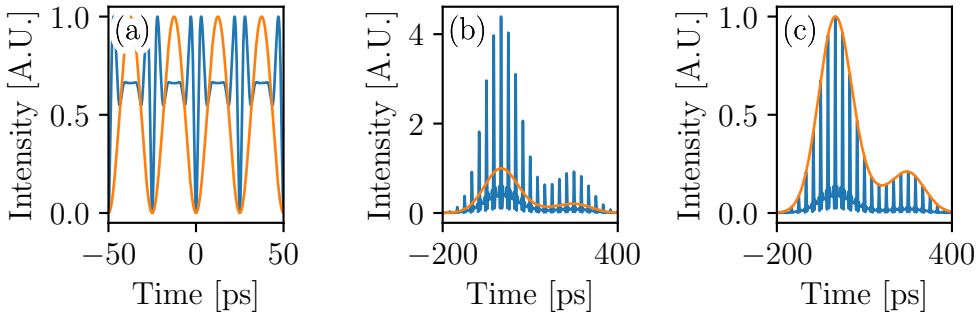

Figure 2.24: Sampling of a signal composed of two gaussians at a frequency of 40 GHz (a) Pump in (orange) and pump out (blue). (b) Signal in (orange) and signal out (blue). It can be observed that the signal is amplified four-fold. (c) Signal in (orange) and signal out (blue) normalized to 1. The sampled signal kept the initial signal envelope.

Fig. 2.24a illustrates the evolution of the pump. It is clearly seen that the pump pulses undergo reshaping during propagation, which leads to a wave-breaking of the pulses and creates very sharp edges, as was observed previously in Section 2.1.4. This reshaping indeed leads to the creation of a pulse train on the signal, as illustrated by Fig. 2.24b, where the pulse train is indeed observed at the end of the fiber. Magnification is also observed, as the energy of the signal is redistributed into compressed short pulses. The envelope of this pulse train conserves the shape of the input signal as displayed on Fig. 2.24c, where the input and output signal intensity of the simulation are normalized to 1 and superimposed, and the output pulses peaks are indeed shown to conserve the input envelope.

2.2.4 Theoretical model analysis

Seeing that this system answers to the same assumptions that were done in Section 2.1.5, the theoretical model developed previously can also be used. As the signal used in this sampling system is however different, the signal amplitude must be rewritten to take the initial envelope into account.

The cosines-like input $A_-(0,t) \equiv A_{-,\mathrm{in}}(t)$ pump reads as $A_{-,\mathrm{in}}(t) = P_0^{1/2}\cos(\omega_p t)$ to which corresponds two spectral components centered at $\pm\omega_p$. The weak input signal is assumed to be a slowly-varying waveform $A_+(0,t) \equiv A_{+,\mathrm{in}}(t)$, instead, whose corresponding optical spectrum is centered around $\omega = 0$ with a spectral

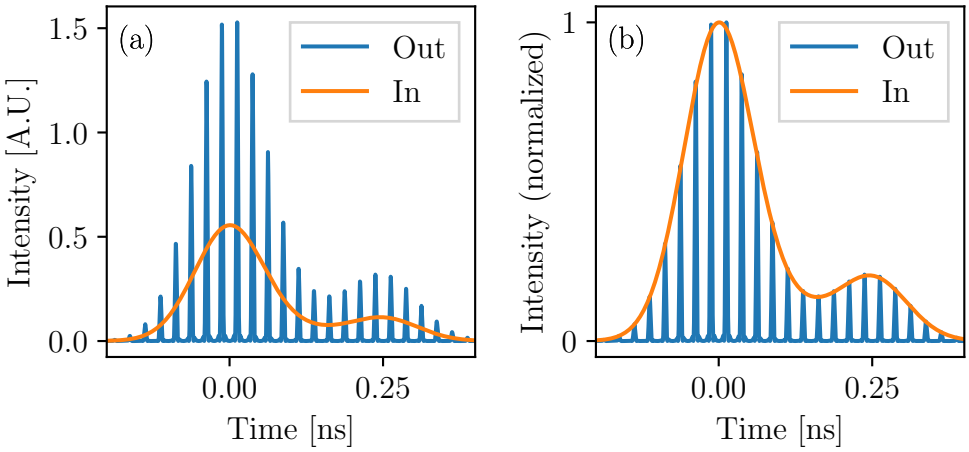

Figure 2.25: Results of numerical simulations obtained by solving the theoretical model. (a) Input (orange) and output (blue) signal. The magnification of the envelope of the pulses is clearly observed. (b) Input and output signal normalized, outlining the conservation of the input signal envelope.

extension well below ω_p. The FWM interaction among the sampling and signal waves leads to the generation of new spectral components centered around odd (even) multiples of ω_p in the pump (signal) spectrum. On the other hand, the different power-level of pump and signal makes their longitudinal evolution deeply different. As long as the fiber length does not exceed few nonlinear lengths, the level of the new spectral components generated by FWM in the pump spectrum remains 10 dB below the original components centered at $\pm\omega_p$ [77]. As in the previous section, the impact of these additional spectral components can thus be neglected as a first rough approximation, and it can be considered that the sinusoidal pump intensity profile is preserved upon propagation except for propagation losses, that is $|A_-(z,t)|^2 = P_0 \cos(\omega_p t)^2 \exp(-\alpha z)$. Note that this approximation remains still valid as long as the shock point undergone by the sampling wave only occurs in the last stage of propagation, which is the case for most of the power values considered in this section. In contrast, the generation of new spectral components cannot be neglected in the case of the weak signal, as their amplitude rapidly grows up to the peak-level of the input signal spectrum $\tilde{A}_{+,\mathrm{in}}(\omega)$. Replica of $\tilde{A}_{+,\mathrm{in}}(\omega)$ arise in the signal spectrum, centered around even-multiples of ω_p, to which the following ansatz $A_+(z,t)$ corresponds:

$$A_+(z,t) = A_{+,in}(t)\left(\sum s_n(z)\exp(i\omega_n t)\right) \tag{2.13}$$

The same LDE as in Section 2.1.4 can then be obtained by introducing Eq. (2.13) in

Eq. (2.4). By solving this equation system, reconstructing the solution by injecting the results in Eq. (2.13), a good estimation of the output signal can be calculated very quickly without having to use the time consuming split-step Fourier method.

Fig. 2.25 illustrates the results from the resolution of the theoretical model for a pump power of 26.5 dBm. Similarly to numerical simulations, a magnification is observed, as shown on Fig. 2.25a, where the envelope of the output pulses is clearly higher than the input signal. Equally, Fig. 2.25b displays that the output signal pulse train conserves the envelope of he input signal by plotting both normalized to 1.

2.2.5 Experiment

As the phenomenon of sampling and magnification through XPM-induced chirp focusing appears out of simulations, an experimental study was done, first to validate those results, then to determine the experimental limitations such a system would bring.

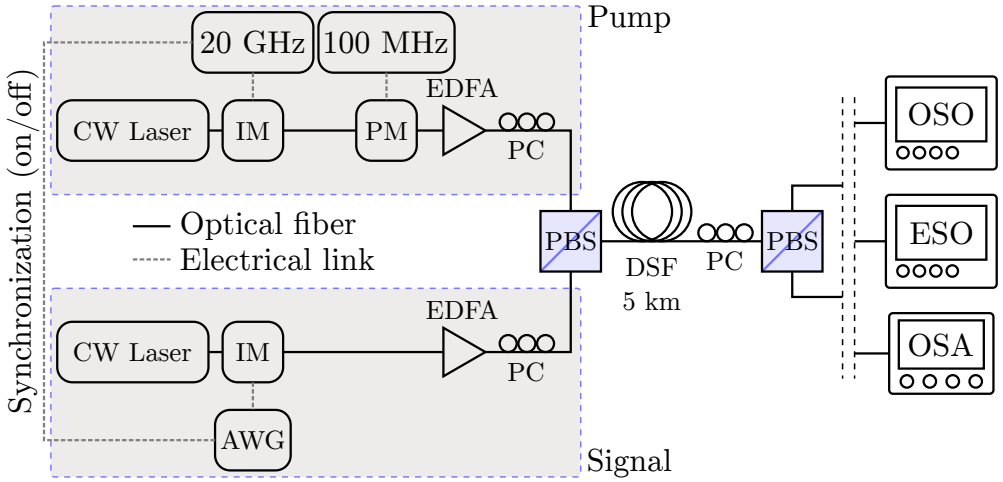

Figure 2.26: Arbitrary signal sampling experimental setup. continuous wave (CW), Experimental setup used to sample an arbitrary signal Intensity Modulator (IM), Phase Modulator (PM), Erbium-doped Fiber Amplifier (EDFA), Polarization Controller (PC), Polarization Beam Splitter (PBS), Arbitrary Waveform Generator (AWG), Dispersion Shifted Fiber (DSF), Optical Sampling Oscilloscope (OSO), Electrical Sampling Oscilloscope (ESO), Optical Spectrum Analyser (OSA)

The setup designed for this experiment is illustrated on Fig. 2.26. To generate the signal to be sampled, a Continuous Wave Laser (CW Laser) emitting at 1550 nm is modulated by an IM, driven by an Arbitrary Waveform Generator (AWG). With this, a concatenation of two unbalanced gaussian pulses for a total

duration of a few nanoseconds is created. The pump wave is created by modulating a CW Laser at 1550 nm through a IM driven at its null-transmission point by a 20 GHz frequency clock, in order to generate a pure carrier-suppressed 40 GHz sinusoidal wave. Moreover, on this axis, a phase modulation at around 100 MHz is added. As explained before in Section 2.1.3, this phase modulation helps to increase the Brillouin threshold above the power levels involved in our experiment[19]. Both components are then separately amplified through two independent EDFA, then are polarization-multiplexed in the fiber, using a PBS, ensuring their orthogonality at the input of the fiber. Both waves are then injected into a 5 km normally dispersive DSF ($\beta_2 = 3.2\,\mathrm{ps\,km^{-2}}$, $\gamma = 1.7\,\mathrm{W^{-1}\,km^{-1}}$, $\alpha = 0.2\,\mathrm{dB\,km^{-1}}$), then demultiplexed using a second PBS before being analyzed using either an Electrical Sampling Oscilloscope (ESO) or an OSO for the time domain, as well as an OSA to analyze the spectrum at the fiber output. Using this setup, it is possible to synchronize or not the intensity modulations of the signal and the pump, allowing for a study of the sampling either in the synchronized or random sampling scheme described in Section 2.2.1. A first experiment was thus carried out with synchronization to allow for the observation of the formation of a pulse train on the signal envelope, a clear signature of the sampling of the signal. Then, the synchronization was removed, allowing for random sampling of the signal, leading to a better temporal resolution of the output envelope.

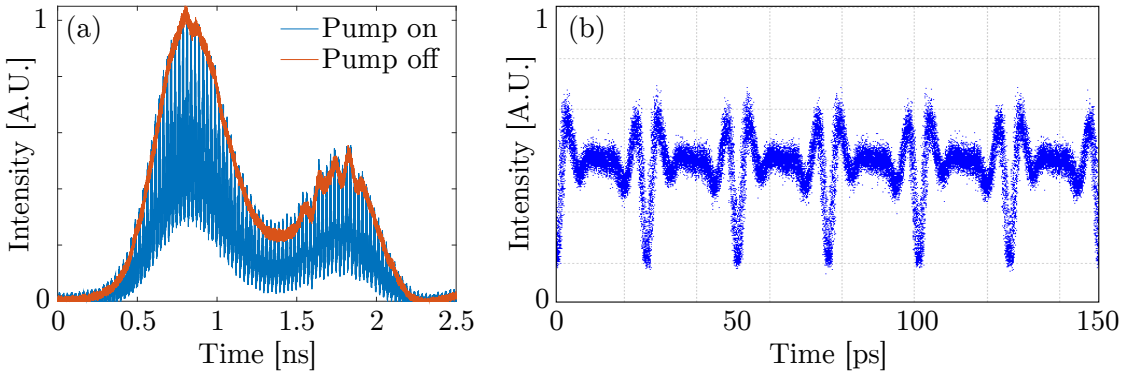

Figure 2.27: Normalized output in the temporal domain for an input pump power of 26.5 dBm (a) Sampled output signal (blue) and input signal (orange). The envelope of the signal is conserved by the generated pulse train (b) Output pump intensity profile, with apparent wave-breaking

The first experimental study was performed using the synchronisation between the signal and pump electrical waveform generators, to allow for the monitoring of the generation of the pulse train on the signal wave. Fig. 2.27 is obtained by sending a signal wave composed, similarly to Section 2.2.3, of two interleaved gaussian pulses, as displayed in orange on Fig. 2.27a, and the orthogonal sinusoidal

pump, at a high power of 26.5 dBm. At the output of the fiber, the high-repetition-rate pulse train generated through the sampling process on the signal wave is clearly observed, and the shape of its envelope exactly follows as the input signal, as expected from the simulations. Fig. 2.27b displays the output pump wave.

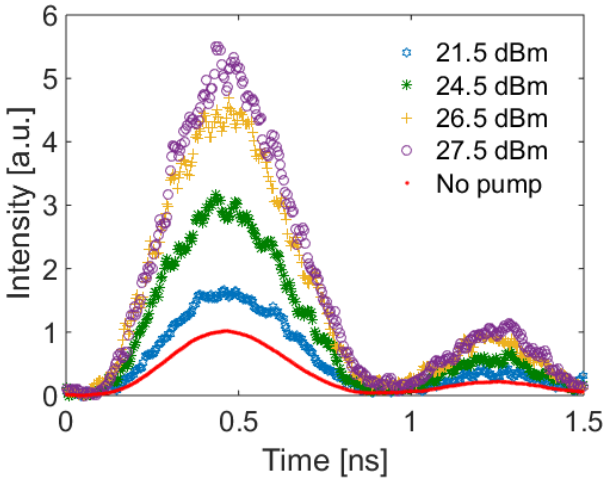

Figure 2.28: Evolution of the outer envelope of the signal with the pump power

However, in a multitude of systems, the signal and the pump will usually not be synchronized. Thus, new measurements were performed by removing the synchronization between the signal and the pump electrical modulation. In this configuration, the pulse train appearing on the signal cannot be resolved anymore. By acquiring multiple traces of the signal intensity and superimposing them, a cloud of points is thus obtained, of which the envelope correspond to the actual pulse train envelope, allowing for the measurement of the magnification factor. The resulting sampled signal is illustrated in Fig. 2.28 as a function of pump power. A magnifying coefficient up to 5.5 is then achieved.

By measuring the spectrum at the output of the fiber using an OSA, the spectrum of the signal was observed experimentally, and is illustrated on Fig. 2.29 for a pump power of 26.5 dBm. On this figure, the numerical spectrum is also shown. The theoretical points are the values of the factors s_n calculated by solving Eq. (2.11) for $z = L$, $n_c < 9$, and plotted at the wavelength equivalent to their associated frequency ω_n, considering the central peak to be 1550.11 nm, similarly to the experimental central peak. The spectrums were normalized so that the central peak intensity is 0 dBm. It can be observed that while the experimental spectrum matches very well with the numerical one, the two harmonics right next to the central one in the theoretical calculations do not match the experimental spectrum correctly. This comes from the fact that strong assumptions were done to

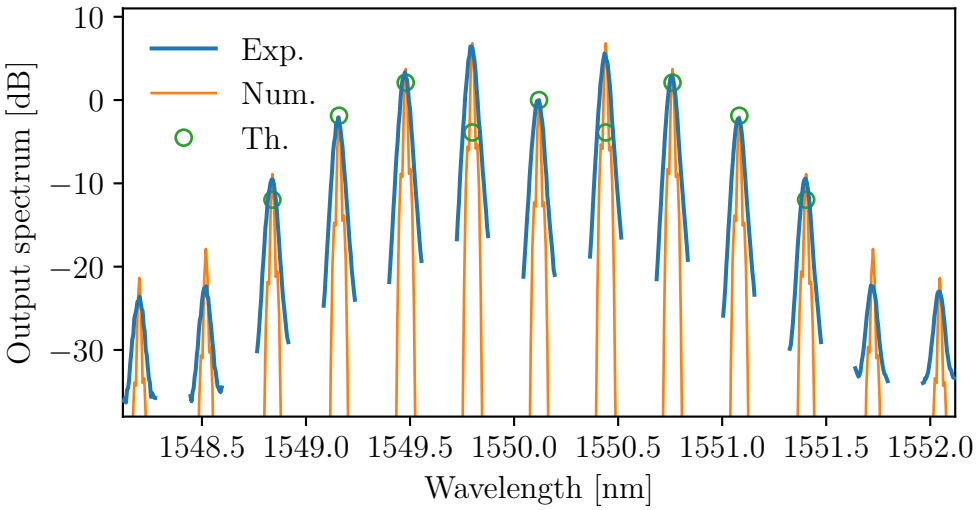

Figure 2.29: Illustration of the spectrum at the output of the fiber, experimentally, numerically and theoretically for a pump power of 26.5 dBm.

draw the theoretical model. Except from those points, the theoretical predictions fit correctly the overall spectrum.

The sampling and magnification of a signal through XPM was observed experimentally in this part, and confirmed through numerical simulations. A theoretical model that can be used for fast estimation of the output pulses and spectrum was also developed, and shown to be in good agreement with the experimental and numerical observations. As the main factor influencing the sampling is the XPM induced from the pump on the signal, which is directly linked to the pump power, the magnification factor evolution with pump power will be studied next.

2.2.6 Impact of the pump power on the sampling

As was explained in Section 2.2.2, the chirp induced by the pump through XPM on the signal wave is one of the main parameters that influences the strength of the sampling. In order to better understand its effect on the sampling, and particularly on the magnification factor of the signal, the pump power was varied from 16 dBm to 28 dBm experimentally, numerically and theoretically.

One first effect observed was the evolution of the magnification factor. As displayed on Fig. 2.30, the signal envelope is not magnified for low powers (at 16 dBm), while a factor up to 5 is achieved experimentally for a pump power of 27.5 dBm. While the curves are very close to one another at low powers, they start to drift apart for higher powers for two reasons. First, the Brillouin limits the

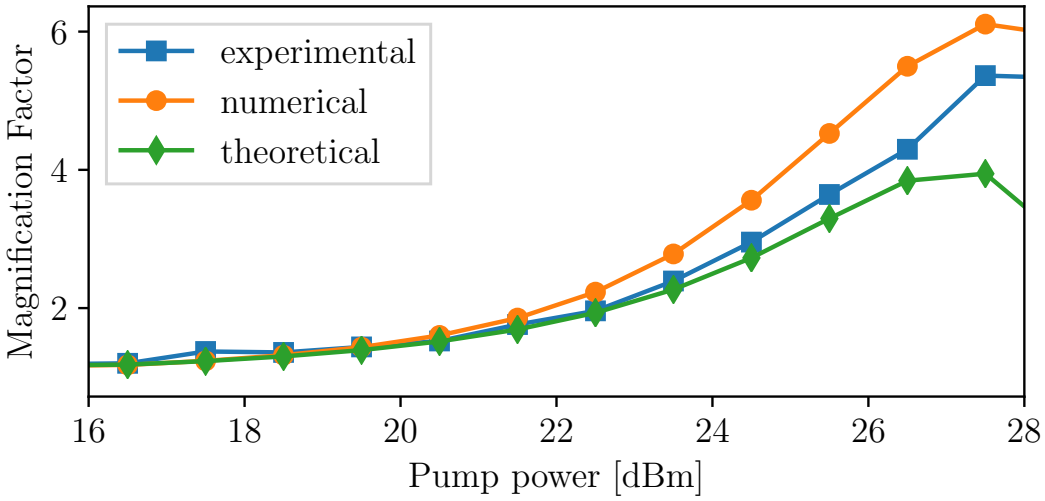

Figure 2.30: Evolution of the magnification factor of the envelope as a function of the pump power. Experimental (blue), numerical (orange) and theoretical (green) results are reported.

sampling in the experimental case, making the sampling less efficient than in the case of the numerical simulation, thus reducing the magnification. At the same time, the Brillouin was experimentally observed to be one of the reasons that the magnification factor saturated. In the theoretical case however, it was pointed out in Section 2.2.3 that the theoretical model developed is only true while the pump pulses do not undergo wavebreaking. As this condition is not respected anymore for higher pump powers, a drift between the theoretical solution and the experimental measurements appears.

The effect of magnification is directly linked to the efficiency of the signal sampling, as the whole pulse energy is compressed into smaller time frames, leading to higher peak powers. Thus, if the sampling is less efficient, *i.e.* at low pump power, the signal pulse train will be less well-formed, while it will improve at higher power, as illustrated by the simulation from Fig. 2.31. Then, as the power keeps increasing, the effects that were observed in Section 2.1.7, namely the pulses deformation and pedestals formation, will start to appear, reducing the quality of the pulse train and the magnification factor as well, as illustrated by the simulation at 30 dBm on Fig. 2.31.

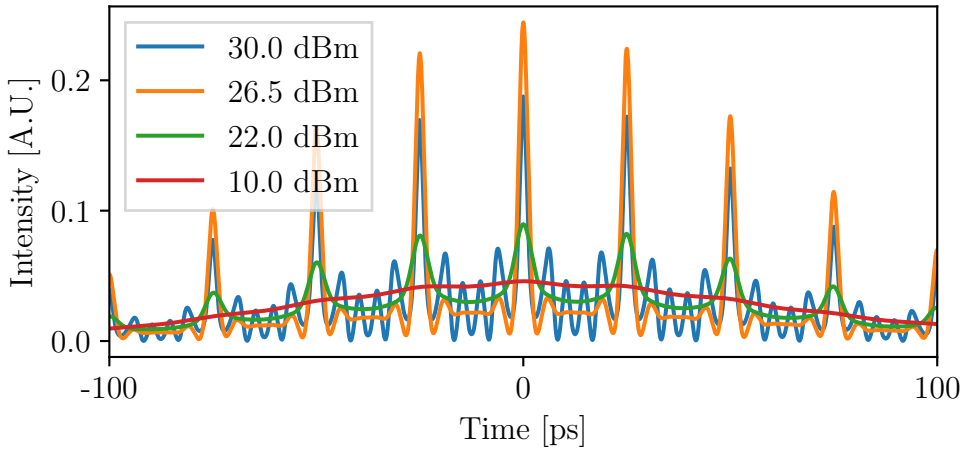

Figure 2.31: Evolution of the sampling pulse train with pump power. The pulses have a higher peak power at high pump power

2.3 Conclusion

In this chapter, two applications of Cross-Phase Modulation polarization were developed. First, a pulse generation system through the compression of a beat signal was created by sending two orthogonally polarized waves copropagating in a normally dispersive fiber, a low power sinusoidal signal and a high power interleaved pump. During propagation, the pump pulses broaden, leading to the formation of dark structures in between them at the point of highest intensity on the signal, leading to the induction of a chirp on the signal that creates a locally focusing regime on the signal pulses through Cross-Phase Modulation and dispersion, allowing the compression of the signal pulses. A simplified numerical model was developed, taking into account the large power difference between the pump and signal. This new model allowed for the derivation of a theoretical model based on LDE, allowing for a very fast approximation of the output pulses (under conditions) without having to solve the numerical model using the time consuming split-step Fourier method. Both numerical and theoretical computations were shown to be in accordance with the experimental observations, and thus validated. It was shown, however, that this process is limited by multiple factors, such as Brillouin scattering appearing out of the high power of the pump, potential compression saturation and pedestals apparition due to wave breaking, as well as pulse deformation due to bad interleaving of the input waves. To conclude, a 3.3 ps pulse train at a repetition rate of 40 GHz was created through this method, being the first single step method of pulse compression in normally dispersive fibers[77].

In a second part, a process based on the same physical effects was developed to sample and magnify an arbitrary signal. Similarly, two waves were injected and propagate with orthogonal polarization in a normal dispersion fiber, *i.e.* a high power sinusoidal pump and a low power signal for which the intensity variations are slow compared to the pump. By the same process of XPM induction, a chirp is generated on the signal wave, creating a locally focusing regime around the dark structures that appeared in the pump. Thus, the energy in the signal is redistributed into short pulses. The envelope of the newly created pulse train was demonstrated to be of the same shape as the input signal one, but magnified. To demonstrate this effect, the system was studied experimentally, allowing for both the observation of the pulse train in the signal wave and the study of the evolution of the magnification factor with the pump power, showing an increase in the magnification with increasing power until wave-breaking, which then leads to a degradation of the generated pulses, thus to a degradation of the magnification factor. Again, the Brillouin scattering also lead to a degradation of the results by limiting the pump power. Those results were validated using the same simplified Manakov model that was developed for the previously studied pulse generation, and theoretical model that was adapted to take into account for the envelope shape of the signal. A magnification factor up to 5 was observed[78].

The results obtained in both experiments demonstrate the possibility of compression of a signal at specific temporal location in a normally dispersive fiber. Thus, it is possible to think of multiple applications of this phenomenon such as the resynchronization of signals or clocking.

Chapter 3

Polarization Domain Walls

3.1 Introduction

A Domain Wall (DW) is a type of topological defect that connects two stable states of a physical system, topological meaning that the shape of the defect is conserved under continuous deformation. DWs are known to be formed, as a result of a spontaneous symmetry-breaking phase transition in a variety of contexts, among which the most common are magnetism[79], condensed matter[80], spinor Bose–Einstein condensates[81], biological physics (energy transfer in proteins and DNA fluctuations, deoxyribonucelic acid)[80], or particle physics and string theory[82]. They also appear as kink structures in close analogy with the celebrated kink solutions of the Sine-Gordon equation[80]. DW structures have been widely studied in ferromagnetic materials[79], in which they are known to bind regions in which all spins or magnetic dipoles are aligned in different directions[79,80,83–86]. Their unique properties are exploited in modern spintronic devices to store or transfer information[87–90]. Despite the fact that DWs have been the subject of numerous studies in ferromagnetism, it is important to note that their equivalent in optics have been poorly exploited so far. This work was done in close collaboration with Mr. Pierre-Yves Bony, Mr. Massimiliano Guasoni and Mr. Javier Nuño.

Optical Domain Walls

Originally, optical DWs referred to vectorial structures that had been predicted theoretically in the defocusing regime of an isotropic single-mode fibre more than 20 years ago[91–95]. They are fundamentally related to the Berkhoer and Zakharov modulational instability phenomenon[12]. The DW corresponds to a localized structure of the kink type that connects two regions of space with different polarizations, the kink structure being defined as the solitonic structure creating the transition from on polarization to the other. In the transition region, the electromagnetic

field switches between two stable states with orthogonal circular polarizations (note that in optical fibres the dynamics is purely temporal and the time along a pulse plays the role of the spatial variable) as illustrated in Fig. 3.1. In this framework, the fast polarization knots lead to two anticorrelated coupled twin waves, where the strong binding force imposed by the cross-phase interaction can compensate for linear and nonlinear impairments induced by normal chromatic dispersion and self-phase modulation, respectively[95]. The polarization distribution is then locked along the propagation within well-defined and robust temporal regions interconnected by Polarization Domain Walls (PDW)[93].

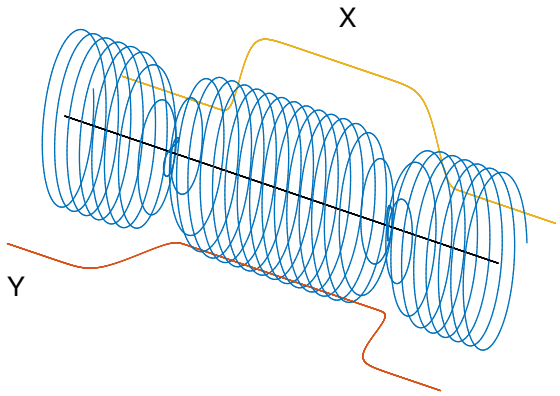

Figure 3.1: Polarization switch between two orthogonal circular polarizations

Owing to their topological nature, a transmission system based on PDWs simply relies on fast polarization switching along the domain edges. As a result, the domains of polarization can be of any time duration and thus can be encoded individually to carry optical data[96–98]. Similarly to the classical bright scalar solitons[99], the topological nature of PDWs makes them strongly robust with respect to external perturbations such as temporal or amplitude fluctuations[91,96]. This property is fundamentally linked to their topological nature, featuring an energy (Hamiltonian) minimum at both sides of the kink. Therefore, their robustness and attractive properties could find numerous applications in optical communications, all-optical processing, data storage and fibre laser devices. However, so far, PDWs remain essentially unexplored experimentally.

In 1999, Kockaert et al. experimentally investigated the vectorial modulational instability process in a small 1 m piece of isotropic fibre and reported an indirect observation of anticorrelated polarization dynamics[99,100], thus validating the theoretical predictions of Berkhoer and Zakharov. In a different context, antiphase behaviour on a nanosecond scale has been reported in fibre ring laser cavities[101,102] and interpreted recently in terms of PDW-like temporal structures[103,104]. Similar antiphase polarization switching has also been observed by Marconi and co-workers

in a vertical-cavity surface-emitting laser[105], which revealed a novel form of dissipative cavity soliton[105,106]. It is important to remember that PDWs reported in laser systems refer to a completely different physics: an optical cavity is inherently a dissipative system[107], which is a marked distinction from the conservative system considered here.

In this part, the observation of PDWs in the classical optical fibres commonly used in optical communications will be detailed. From a broader perspective, it is found that modern conventional fibres exhibit previously unrevealed peculiar properties, which are shown to support the existence of PDWs in any arbitrary polarization basis. For this reason, the novel class of polarization structures reported here has been termed as universal PDW. More specifically, a genuine demonstration of the existence of these fundamental structures and exploit their unique topological properties for optical data transmission beyond the nonlinear Kerr-induced limitations of classical normally dispersive fibres is provided. More unexpectedly, the robust attraction properties of these entities, manifested as the spontaneous emergence of synchronized PDWs from a system of incoherent random waves, leading to a phenomenon of polarization segregation, in analogy with the fundamental order-disorder phase transition in ferromagnetic materials is also highlighted. Finally, the present observation of PDWs in standard optical fibres raises important questions concerning the limits of the validity of the Manakov model for modern standard optical fibres. A new model is thus proposed, studied and linked to both the Manakov and the isotropic model, opening a new domain of exploration in between them.

3.2 State of the art

As the bright soliton and MI arise from a stable or unstable interaction of the dispersion and the SPM in anomalous dispersion fibers, it was intuited by Christodoulides and Joseph[108] and independently by Tratnik and Sipe[109] from the theoretical prediction of Polarization Modulation Instability (PMI)[12] that bound states similar to the bright soliton should exist, arising from the interaction between linear and nonlinear coupling effects between two orthogonal polarization states. Such bound structures were demonstrated in the way of coupled dark and bright soliton by Christodoulides[110] in birefringent media, and were shown to exist theoretically in non-birefringent media by Haelterman et al.[111,112].

Haelterman went further in studying the stability of the coupled system of

NLSE in the circularly polarized basis defined by

$$\begin{aligned} i\frac{\partial A_+}{\partial z} - \frac{1}{2}\frac{\partial^2 A_+}{\partial T^2} + \left(|A_+|^2 + \sigma |A_-|^2\right) A_+ = 0 \\ i\frac{\partial A_-}{\partial z} - \frac{1}{2}\frac{\partial^2 A_-}{\partial T^2} + \left(|A_-|^2 + \sigma |A_+|^2\right) A_- = 0 \end{aligned} \tag{3.1}$$

where A_+ and A_- are the envelopes of, respectively, the right-hand and left-hand circularly polarized components of the signal, z is the spatial position in the fiber, T is the time coordinate in a reference frame travelling at the group velocity of the light, and σ is the XPM coefficient. We are now looking for stationary periodic solution of the form

$$A_+ = u(T)\exp(i\beta z) \tag{3.2}$$

$$A_- = v(T)\exp(i\beta z) \tag{3.3}$$

where the functions u, v and the propagation constant β are real, that those functions follow a set of coupled ordinary differential equations given by

$$\begin{aligned} \frac{1}{2}\ddot{u} + \beta u - u^3 - \sigma v^2 u = 0 \\ \frac{1}{2}\ddot{v} + \beta v - v^3 - \sigma u^2 v = 0 \end{aligned} \tag{3.4}$$

that represent the equations of movement of a unit mass in a potential given by

$$V = \beta(u^2 + v^2) - \frac{1}{2}(u^4 + v^4) - \sigma(u^2 - v^2) \tag{3.5}$$

The solitary solutions to Eq. (3.1) correspond to the trajectories separating the maxima of this potential. The potential is plotted on Fig. 3.2, and the separatrices displayed represent the different solitonic structures. The separatrices joining the opposing maxima represent the circularly polarized NLSE dark soliton, while the separatrices joining the opposite saddle points represent the linearly polarized dark solitons. By studying the separatrices joining the adjacent maxima, it was shown that they also represent a solitonic structure, the PDW.

Those structures were later generated experimentally by Pitois et al.[113] in a 1 m fiber that could be considered isotropic. The same experiment allowed for the confirmation of the generation of PMI in isotropic-like fibers, indicating a link between the two phenomenon, similarly to the link observed between the bright soliton and scalar MI in anomalous dispersive fiber. The PMI characteristics theoretically described by Berkhoer and Zakharov[12] were demonstrated experimentally. The PMI

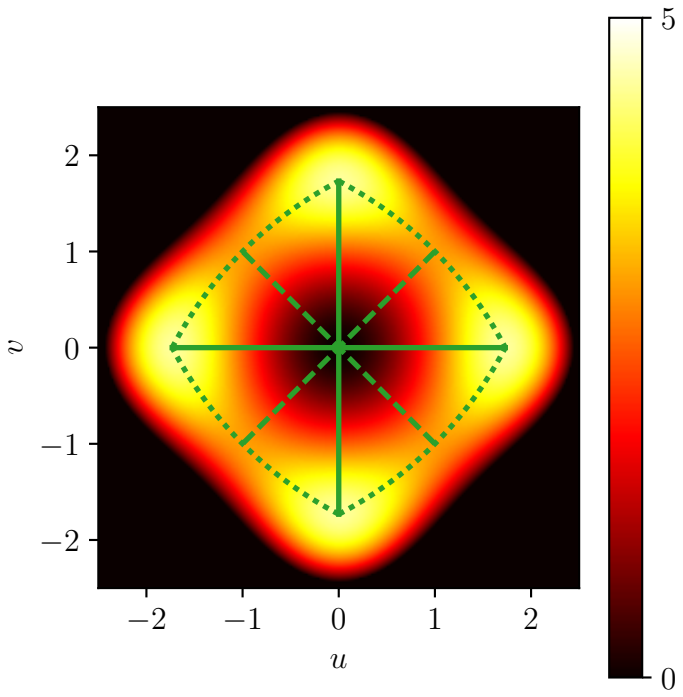

Figure 3.2: Plot of the potential V. Solid lines show the separatrices of the circularly polarized NLSE dark soliton, while dashed lines those of the linearly polarized dark soliton. Dotted lines represent the separatrices of the PDW.

bands generated were indeed proven orthogonal to the pump and the frequency cut and gain generated were in accordance with the theory.

From this point, the study of PDW is expanded by the following sections, first observing the formation and propagation of PDW in longer fibers, then by transmitting data using this phenomenon. As the previous model suggests, if PDW are observed in a fiber, PMI should also be observed. A study of PMI in the fibers used for the PDW transmission was also performed and an extended model was developed to explain the observations of this chapter.

3.3 Observation of polarization domain walls

In order to better understand the PDW, experimental and numerical generation of the structures were performed. The experimental generation and propagation through an optical fiber will be discussed before the corresponding simulations are done, using an adapted Manakov model that phenomenologically takes into account the intrinsic characteristics of the fiber, used so that the formation of

PDW is possible.

3.3.1 Experimental setup

In order to create PDW, a polarization switch between two orthogonal polarizations must be created, as illustrated by Fig. 3.1. A simple way to do this is to create a single periodic signal, in this case at a clock frequency of 28 GHz, divide it in two replicas then delay one of the two signal by half a period before recombining the signals using a PBS, to ensure that the signals are orthogonal. The interleaving of signals on the polarization axes will effectively create a polarization switch at the edges of the signals, the speed of the switch being determined by the raising and falling time of the pulses on each axis of polarization.

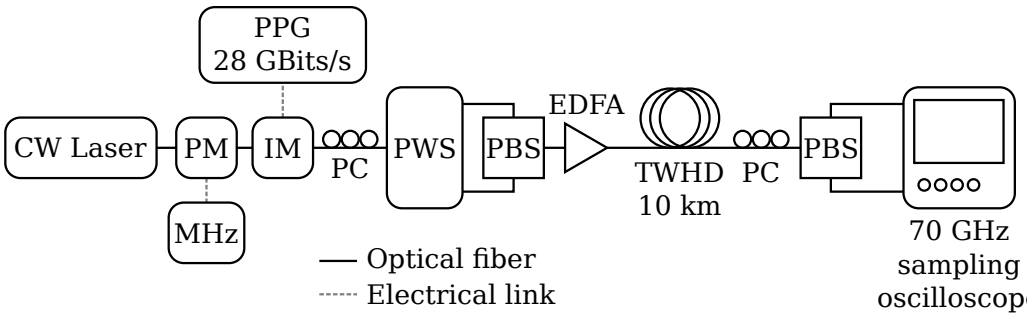

Figure 3.3: Experimental setup for the generation and transmission of PDW. CW: continuous wave, PM: Phase Modulator, IM: Intensity Modulator, PPG: Pulse Pattern Generator, PC: Polarization Controller, PWS: Polarization WaveShaper, PBS: Polarization Beam Splitter, EDFA: Erbium-doped Fiber Amplifier, TWHD: TrueWave High-Dispersion fiber.

To achieve this, the setup illustrated in Fig. 3.3 was used. A CW laser is first modulated by a Phase Modulator (PM) driven by a triple tone Radiofrequency (RF) signal, at frequencies of 52 MHz, 203 MHz and 506 MHz in order to reduce the Brillouin threshold and reach higher powers during the experiment[2]. The signal is then encoded in intensity using a 40 GHz bandwidth intensity modulator driven by a simple two bit sequence of 0 and 1 at a bit rate of 28 Gbits/s provided by the electrical multiplexing of two Non-Return to Zero (NRZ) Pulse Pattern Generator (PPG). The signal thus created consists in pulses with a duration of 30 ps (numerically fitted with a 2th order super-gaussian) at a repetition rate of 14 GHz, with a duty cycle of 1:2, as illustrated on Fig. 3.4. The rise and fall time of the pulses were measured to be 8 ps. This signal was then injected at 45° of the axes of a PWS. The PWS allowed to finely adjust for each arm power and delay, to obtain precise interleaving of the signals and the exact same power on

each polarization axis. At the output, both arms were recombined on orthogonal polarization axes using a PBS, ensuring the orthogonality of the signals. The full signal is then amplified through an EDFA, and sent in a 10 km TrueWave High-Dispersion fiber (TWHD) fiber, characterized by a chromatic dispersion of $D = -14.5\,\mathrm{ps\,nm^{-1}\,km^{-1}}$ at a wavelength of 1550 nm, a PMD of $0.02\,\mathrm{ps\,km^{-1/2}}$, a loss coefficient $\alpha = 0.2\,\mathrm{dB\,km^{-1}}$ and a nonlinear Kerr-coefficient of $\gamma = 2.5\,\mathrm{W^{-1}\,km^{-1}}$. After propagation, the signal was demultiplexed in polarization using a second PBS, associated with a Polarization Controller (PC). This allowed to observe each polarization axis independently on the input polarization basis, by visualizing them via a dual-input ESO inputting from two 70 GHz bandwidth photodiode. The input polarization basis was obtained by switching off one of the two input axes of polarization and minimizing the signal on one of the output PBS arms, ensuring that most of the output power is present on the second arm of the PBS.

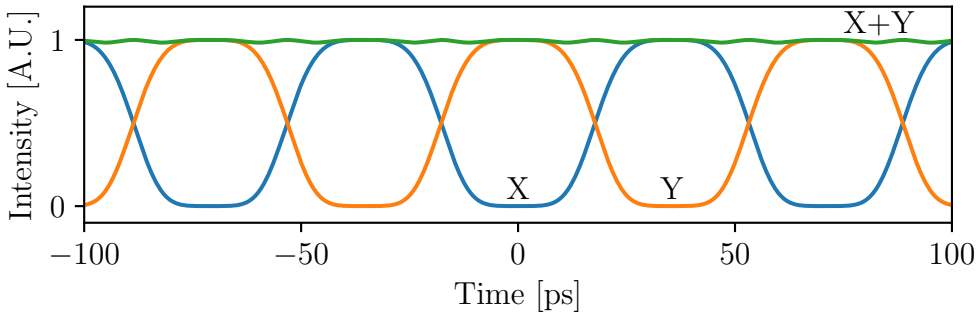

Figure 3.4: Experimental input signal intensities. The total intensity (sum of the two polarization components) is almost constant.

It is important to remark multiple characteristics for this setup. First, when recombined after the first PBS, the total signal intensity profile is almost constant, as observed on Fig. 3.4. This is indeed expected, as it is the polarization switch that creates the PDW, and having a constant total power indicates adequate interleaving and power equilibrium between the two orthogonal polarizations. It can also be noted that thanks to the PC before the fiber, the input polarization basis can be randomly chosen, making the PDW universal. As long as both polarization are orthogonal to one another and the kink structure is present, the input polarization basis seems to have no incidence, contrary to the results obtained by Haelterman et al.[91], which demonstrate the apparition of PDW only in the circular polarization basis.

Finally, it is important to note that the fiber that was used is equivalent to a standard telecommunication fiber in that it exhibits a randomly distributed

residual birefringence, and an imposed birefringence spinning aimed at controlling the natural birefringence fluctuations. This spinning and its effect will be explained in more details in Section 3.6.3.

3.3.2 Experimental results

To assess the apparition of the PDW during propagation, the same signal was sent propagating, with and without the polarization knots, which in effect was equivalent to sending one polarization axis or both of them. By increasing the average power of the input signal, the nonlinear effects (SPM, and eventually XPM) undergone during propagation increase. As the power increases, the equilibrium created between the chromatic dispersion, SPM and XPM when the kink structures are present is expected to be apparent by observing almost undistorted output signals in each of the orthogonal polarization components.

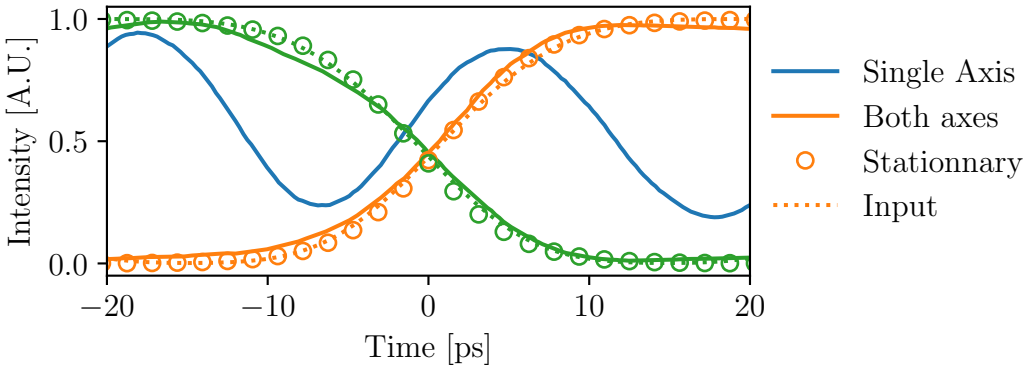

Figure 3.5: Output of one polarization axis of the fiber with and without the second axis of polarization at an average power of 26 dBm. Dashed: input signal, blue: output for a single axis of polarization propagating, green and orange solid: experimental data for the two axes of polarization copropagating, circles: simulated stationary state for two copropagating polarization.

As can be seen on Fig. 3.5, when a single axis of polarization is transmitted trough the fiber, the signal undergoes the standard chromatic dispersion and SPM effects, leading to a rapid deterioration of the signal and loss of the initial shape, increased by overlapping between adjacent pulses. However, when the second polarization axis is copropagating, interlock between both signals leads to a propagation without deformation, highlighting the propagation of PDW structures. The edges of the two orthogonal signals are clearly conserved, even if slightly deformed, indicating the presence of a solitonic structure at the polarization switch location. The simulation was also performed until the stationary state in which there were

no deformation of the signal anymore appeared. It can be observed that the experimental results are very close to this state, confirming the robustness of the equilibrium.

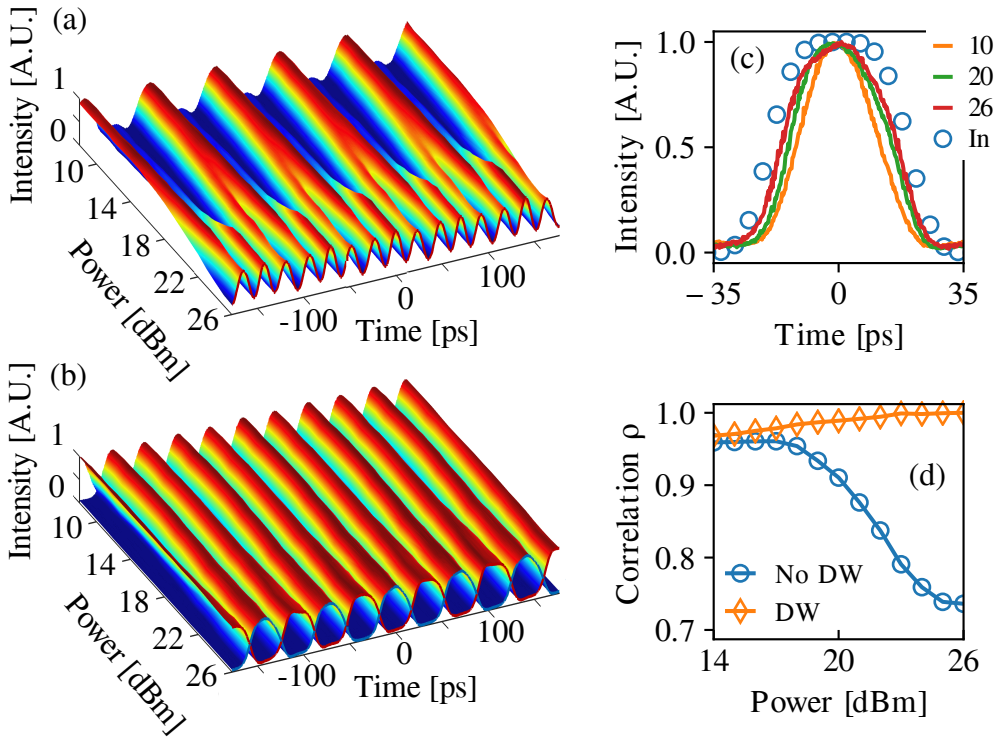

Figure 3.6: Observation of PDW solitons. (a) Normalized Output signal without the orthogonal axis of polarization copropagating (b) Normalized Output signal with orthogonal axis (c) Evolution of the pulses edges of the PDW with input power (on a single axis), orange: 10 dBm, green: 20 dBm, red: 26 dBm (d) Evolution of the correlation factor between input and output with injected power, circles: single signal propagation, diamonds: two signals copropagating

Fig. 3.6a displays the experimental intensity profile as a function of injected power and time. Even though the signal can be injected and retrieved with relatively low error at weak average powers when sent alone, the wave-breaking at high powers will completely change the energy distribution of the signal, making telecommunication transmission impossible. However, Fig. 3.6b shows that when the complementary signal is injected and copropagates on the orthogonal axis of polarization through the fiber, the created interlock leads to a high quality transmission of the input signals. The PDW were not observed at higher power than 26 dBm as Brillouin scattering becomes too significant.

Finally, Fig. 3.6d shows the evolution of the correlation between the input and output signals. The correlation is calculated by Eq. (3.6)[114]:

$$\rho(U_{in}, U_{out}) = \frac{\langle U_{in} U_{out} \rangle}{\sqrt{\langle U_{in}^2 \rangle \langle U_{out}^2 \rangle}} \tag{3.6}$$

with U_{in} and U_{out}, respectively the input and output signal intensity. This correlation coefficient is close to 1 when the signals are correlated, to 0.5 when no correlation is observed and to 0 when the signals are anti-correlated. This means that on Fig. 3.6d, when the coefficient is close to 1, the shape of the output is very close to the one of the input signal. Thus it can be seen that when sending a single polarization axis, the input signal is quickly lost, with almost no correlation with the shape of the input signal, while it is very well conserved and even improves at higher power levels when sending both polarization axes. While at low powers the signals undergo only chromatic dispersion as a significant effect during propagation, increasing power enhances the nonlinear effects, thus allowing for PDW propagation and better conservation of the initial edges.

3.3.3 Simulations results

As shown by Haelterman et al.[91], the Manakov model does not allow for the generation of PDW when the random birefringence is taken into account, as the ratio between XPM and SPM is 1. Extending the Manakov model, they introduced a new model, including a cross-phase modulation factor superior to 1. This model is defined by the coupled equations

$$i\frac{\partial A_+}{\partial z} = -\frac{\alpha}{2}A_+ + \frac{\beta_2}{2}\frac{\partial^2 A_+}{\partial t^2} - \gamma\left(|A_+|^2 + C_{XPM}|A_-|^2\right)A_+ \tag{3.7}$$

$$i\frac{\partial A_-}{\partial z} = -\frac{\alpha}{2}A_- + \frac{\beta_2}{2}\frac{\partial^2 A_-}{\partial T^2} - \gamma\left(|A_-|^2 + C_{XPM}|A_+|^2\right)A_- \tag{3.8}$$

where A_+ and A_- are the orthogonal polarization components of the signal, z is the propagation coordinate along the fiber, T the local time in the reference frame of the fields, β_2 the chromatic dispersion coefficient of the fiber, γ the nonlinear coefficient of the fiber, α the losses coefficient of the fiber, and C_{XPM} the XPM coefficient being intrinsic to the fiber material. By fitting the experimental data numerically, an XPM value of 1.3 was obtained, which also fits properly the stationary solution. It must be noted that the coefficient determined will only be valid for the fiber used during the experiment, the factor being material dependant[93].

Using this cross-correlation coefficient, simulations were done to explore the behaviour of the PDW outside the limitations of the experiment. Fig. 3.7a and

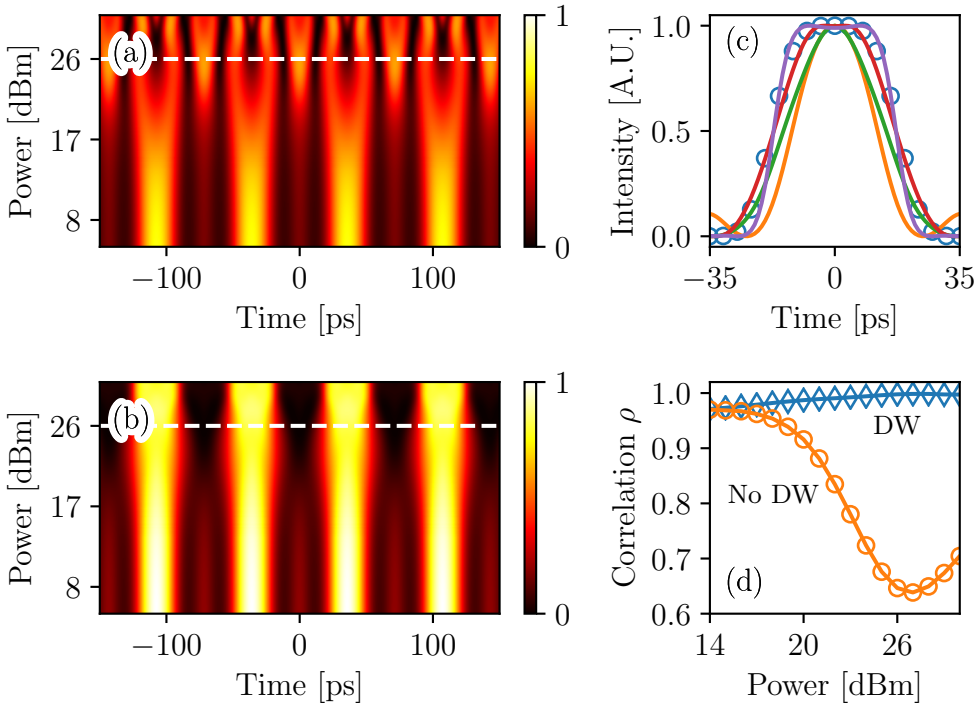

Figure 3.7: Simulation of PDW solitons. The white dashed line is the power at which the experiment stopped (a) Output signal without the orthogonal axis of polarization copropagating, (b) Output signal with orthogonal axis, (c) evolution of the pulse edges with input power, orange: 5 dBm, green: 20 dBm, red: 26 dBm, purple: 30 dBm, circles: input (d) Evolution of the correlation factor between input and output with output power, circles: single signal propagation, diamonds: two signals copropagating

Fig. 3.7b respectively display the output signal of the fiber when a single or both signals are sent copropagating. The white dashed line shows the limit of the experimental results. Similarly to the experimental case, Fig. 3.7a displays that the input signal shape is quickly lost as the power increases, while it is well conserved with the copropagating wave, as shown in Fig. 3.7b However, it can be observed that at low powers, a similar feature appears for both cases, which was not observed during the experiment while the two waves were copropagating. A small peak appears in between the main pulses, and increases when the power increases in the single polarization propagation case, but disappears completely at high power when propagating PDW. This feature comes from the dispersion of the pulses, and is pushed back away to the main pulses as the power increases by the chirp

generated by the pulses on the other polarization axes. This can be observed on Fig. 3.7b between 17 dBm and 26 dBm, where the small bump disappears and the main one broadens. Fig. 3.7c shows the evolution of the pulses with power. Broadening similar to Fig. 3.6c can be observed, the curve colors between the two figures being for corresponding powers. However, a curve at 30 dBm was also plotted here, and displays the behaviour of the PDW for increasing power when the equilibrium is reached. As can be seen, the pulse edges sharpen significantly when the power goes from 26 dBm to 30 dBm, becoming even sharper than the input pulse edges. This validates the assumption that SPM, XPM and chromatic dispersion all play a part in the generation of PDW, making them of a different nature to those observed in the backward wave configuration by Pitois et al.[115].

Finally, Fig. 3.7d exhibits the same correlation as for the experimental data reported on Fig. 3.6, meaning that the single propagating wave sees a drop in correlation with the input signal as the power increases, while the dual propagating wave sees no change, and is even better correlated to the input for higher powers. At the highest powers (> 26 dBm), the correlation goes back up for the single propagating wave. However, as can be clearly seen on Fig. 3.7a, the signal is completely lost and the slight correlation improvement is not significant of an increase of the transmission quality.

3.3.4 Limitations and perspectives

Similarly to the limitations encountered in Chapter 2, Brillouin scattering is one of the main limitations of this experiment. The increase of the Brillouin threshold gained using the triple-tone phase modulation, however, allowed for a maximum mean power of 29 dBm which permitted for first observations of the PDW. Attaining higher pulse peak powers can be achieved by carving the signal in half and leaving the rest to 0, then amplifying the newly created signal. This method will be explained in more details and used in Section 3.4.

The PDW were, in this section, generated using pulses with a fixed rising and falling time, which were modified with the equilibrium formed by the SPM, XPM and chromatic dispersion. By varying the parameters of the gaussian (order, width), a range of rising and falling times would be available to study, and the limits of the equilibrium could be studied in more details, such as the minimum and maximum limit rising time allowing for the formation of PDW, and the possible convergence of the rising and falling times for a given power after propagation over very long distances.

3.4 Transmission of data encoded as polarization domain walls

In Section 3.3, it was demonstrated that it is possible to transmit signals with almost no deformation of its temporal intensity profile, by creating a periodic PDW. In this previous experiment, what was effectively achieved was the transmission of signals composed of alternating 1 and 0. In order to extend on the idea of transmitting an NRZ encoded signal, a new experiment was designed, allowing to sent any arbitrary data using PDW solitons. Transmitting such an energy distribution without deformation would also prove the localized nature of the PDW by showing the same repartition of energy after propagation, demonstrating their individual nature and robustness to external factors.

As a proof of concept, the name of the European project financing this thesis, 'PETAL', was transmitted in ASCII and encoded as an NRZ signal through 50 km of TWHD fiber, with its complementary signal copropagating on the orthogonal axis of polarization in order to create polarization knots. The setup used to generate this transmission is first detailed, expliciting the signals used, before the results obtained by the transmission of the encoded waves are displayed and analyzed. The impact of the generation of PDW on the data transmission will be explained and a conclusion on the characteristics of the PDW demonstrated by this experiment will be drawn.

3.4.1 Experimental setup

The basic principle of creation of a switching polarization wave encoded as NRZ is the same as was previously described in Section 3.3.1. By introducing the signal on one axis of polarization and its complementary on the orthogonal polarization, a signal of constant total power with switches at the rising and falling edges of the signal is created, thus forming kink structures. The signal that was encoded in the wave as an NRZ signal was the word 'PETAL', the name of the European project that financed this PhD, translated as an ASCII bit-word, which is translated on Eq. (3.9). Its complementary was also translated on Eq. (3.10) At the beginning of the signal were added 6 extra 1 bits, as illustrated in Fig. 3.8 that act as buffer to protect the edge bits from deformation induced by chromatic dispersion, SPM, and XPM, while those 6 extra bits were added at the end of the complementary signal, to protect the end of the word. Similarly, both buffers could have been added to either the signal or its complementary wave and have the same protection effect, as long as the buffer was large enough.

$$data \rightarrow \quad 01010000010001010101010001000000101001100 \tag{3.9}$$

$$\overline{data} \rightarrow \quad 10101111101110101010101110111111010110011 \tag{3.10}$$

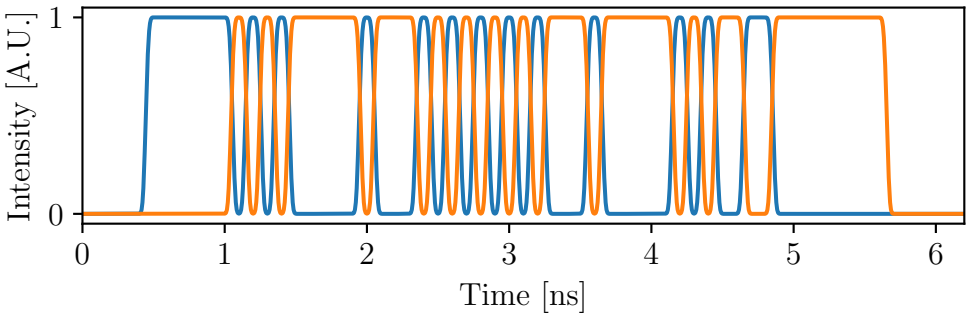

Figure 3.8: Encoded signal and its complementary interleaved.

In Section 3.3.4 was introduced the concept of signal cutting, to increase the peak power of the pulses injected into the fiber. In the previous experiment, every bit of the 2-bit sequence was used, with one bit at 1 and one bit at 0. By amplifying to a average power of 20 dBm, the peak power of the pulses would be exactly this power, when sending both polarization axes, as the resulting total signal is constant in intensity. If, however, the length of the sequence is changed to a 4 bits, meaning having '1000' on one axis and '0100' on the second axis, the average power would still be 20 dBm, but a duty cycle of 1:2 over the whole signal is created, thus increasing the peak power of the pulses to 23 dBm, twice as much in the ideal case. When propagating data using PDW, the same principle was used. Indeed, the total length of the bit repeated pattern was of 128 bit, but the total used word length (meaning the word 'PETAL' as ASCII with the two 6 bit buffers) was of 52 bits. This results in a peak power 2.5 times larger as the average power of the amplified signal when both polarization are injected. However, this process is limited, and the background noise amplification and amplifier noise are not taken into account in those calculations. Thus, while the amplification will be higher for a single signal, the factor calculated previously will not be reached, and noise could be generated from the EDFA. This method of generation of pulses however allows to reach much higher peak powers with a low mean power, thus limiting the generation of Brillouin scattering that was the main limitation in the previous experiments.

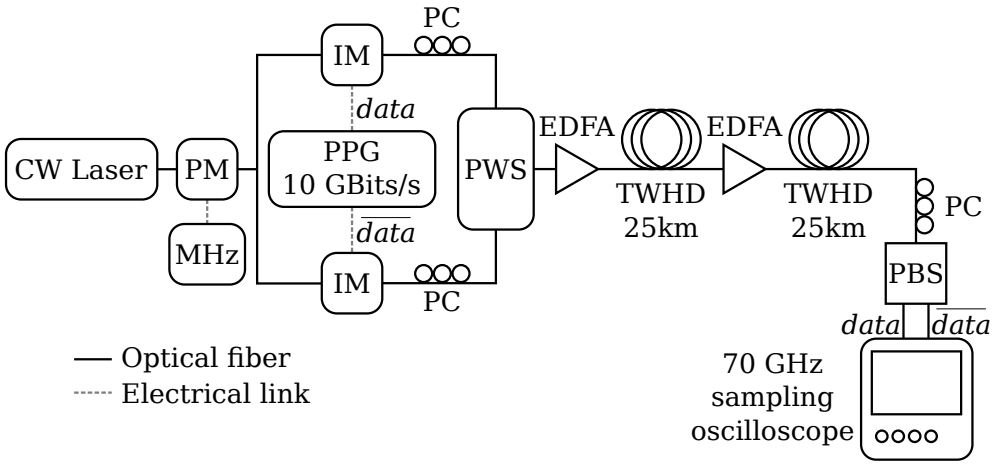

Figure 3.9: Experimental setup for the transmission of NRZ data in a 50 km fiber. CW: continuous wave, PM: Phase Modulator, IM: Intensity Modulator, PPG: Pulse Pattern Generator, PC: Polarization Controller, PWS: Polarization WaveShaper, EDFA: Erbium-doped Fiber Amplifier, TWHD: TrueWave High-Dispersion fiber, PBS: Polarization Beam Splitter

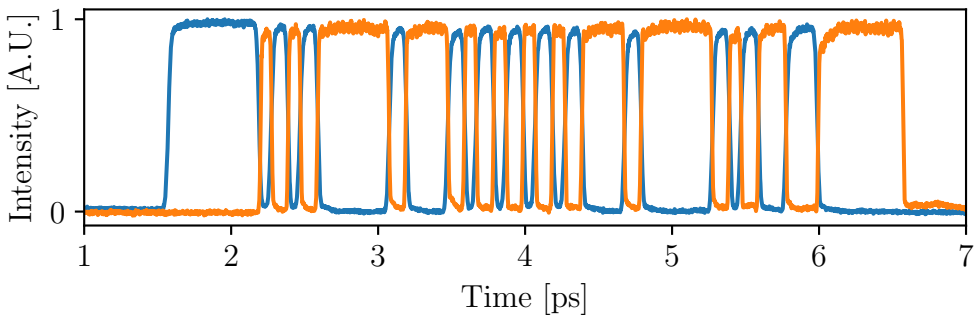

Figure 3.10: Encoded signal and its complementary interleaved, experimental input.

The experimental setup used to obtain this signal is illustrated on Fig. 3.9 and the inputs on Fig. 3.10. A CW laser was first phase modulated in order to reduce the Brillouin scattering using the same method as in Section 3.3.1 and the same triple-tone RF driving signal. This signal is then divided in two branches of equal intensity using a polarization maintaining 50:50 coupler. The replicas are then intensity modulated in parallel through two intensity modulators, one driven by the phase-matched *data*, the second by $\overline{data}$, to which the buffers had been added, given by the 10 Gbit s^{-1} NRZ PPG. The two signals are then synchronized in time,

adjusted in intensity and recombined on orthogonal polarization axes using a PWS. The total signal is then amplified using a 33 dBm EDFA and injected into a first 25 km spool of fiber (TrueWave high-dispersion fiber, characterized by a chromatic dispersion of $D = -14.5\,\mathrm{ps\,nm^{-1}\,km^{-1}}$ at a wavelength of 1550 nm, a PMD of $0.02\,\mathrm{ps\,km^{-1/2}}$, a loss coefficient $\alpha = 0.2\,\mathrm{dB\,km^{-1}}$ and a nonlinear Kerr-coefficient of $\gamma = 2.5\,\mathrm{W^{-1}\,km^{-1}}$, the same type of fiber as in Section 3.3.1). After propagation in the first fiber, the signal is reamplified using a second EDFA then sent into a second identical fiber, for a total propagation distance of 50 km, increasing the propagation length of the data by a factor of 5 compared to the experiment of Section 3.3. At the output of the second fiber, the signal is demultiplexed using the combination of a PC and a PBS allowing to observe both polarization components on a 70 GHz ESO, using the same method at the output as in Section 3.3.1.

3.4.2 Experimental results

The output signals were monitored and their evolution with input power was recorded. When a single axis of polarization was sent at the input (no formation of PDW), the data that can still be distinguished for the low input powers (in the linear regime) is completely lost when the power increases, the pulses being degraded through chromatic dispersion and SPM. This can be observed on Fig. 3.11a. On the other hand, when both orthogonal signals are propagating in the fiber (creation of PDW), it can be clearly seen on Fig. 3.11b that the energy is confined between the multiple PDW, leading to a conservation of the information sent at the input of the fiber, from as low power as 10 dBm to up to 26 dBm of average power. The output temporal profile for an initial power of 24 dBm is plotted on Fig. 3.11c. While the single propagating signal has been deformed by dispersion and SPM (in Green), the two copropagating signals can be seen to be still containing the input information (orange and blue).

Fig. 3.11b displays that while the data is indeed preserved, the extra buffer suffer from temporal deformation due to chromatic dispersion and SPM, thus protecting the actual data transmitted. Indeed, without the buffer, the first bits of the signal would have been the ones affected by deformation, leading to a degradation of the input signal. The buffer being large enough, the undesired effects did not reach the propagating signal for this length of propagation. In this configuration however, a longer propagation might indeed lead to loss of signal, the buffer not being large enough to protect the data packet.

Fig. 3.11d finally shows the effect of the formation of DW on the signal spectrum. When a single polarization is injected into the fiber, broadening of the spectrum by SPM is observed as expected. However, when the two polarizations are sent, the spectrum broadening is greatly reduced. Indeed, the chirp created by SPM is compensated by the XPM induced by the orthogonal polarization compo-

nent, leading to a conservation of the spectrum.

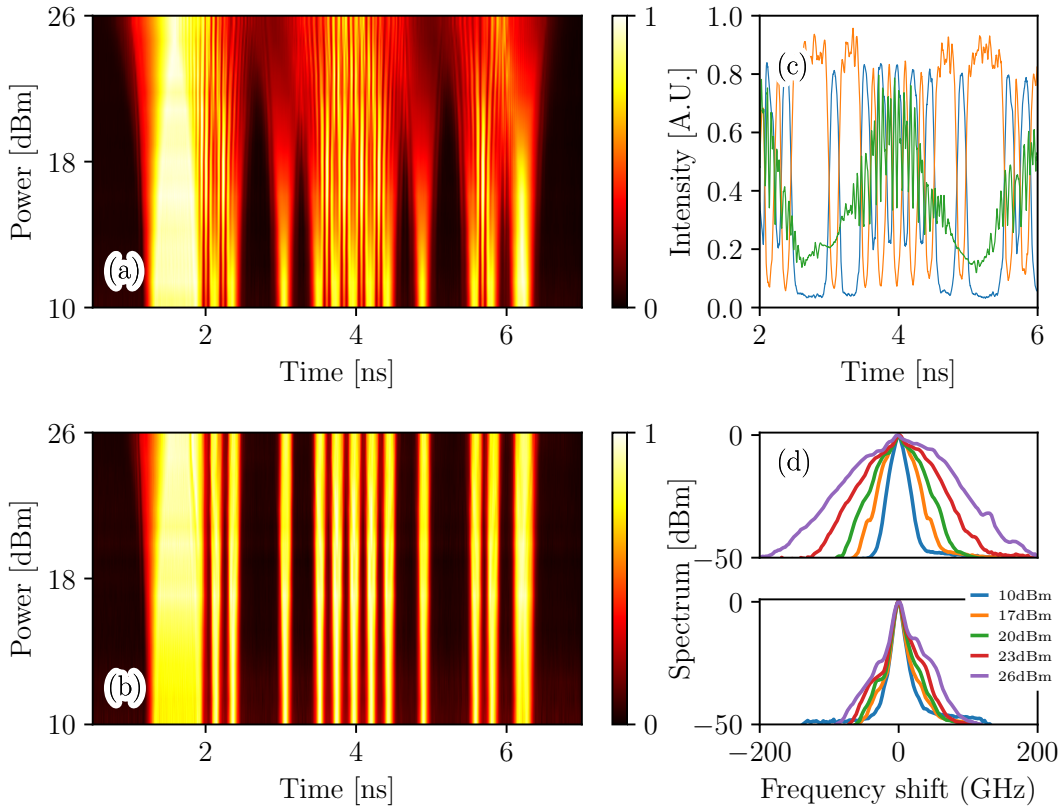

Figure 3.11: Evolution of the output signal with power after propagation in a 50 km TWHD (a) Single components of polarization at the input (b) Both components of polarization at the input (c) Temporal signal for an average input power of 24 dBm after propagation. Green: single components of polarization as input, orange and blue: copropagating orthogonal signals (d) Spectrum evolution with power, without (top) and without (bottom) the second signal copropagating.

3.4.3 Simulations results

After seeing that it is indeed possible to transmit data using PDW, it was necessary to validate that the phenomenological model developed in Section 3.3 is actually correct. For that, the same data than during the experiment was simulated to propagate through 2 successive 25 km fibers, in the same setup as during the experiment, with amplification in between the two fibers. For these simulations, the model described by Eq. (3.7) and Eq. (3.8) was used, with a cross-correlation

coefficient $C_{XPM} = 1.3$. The simulation was done in two steps, including the reamplification of the signal in between the two fibers.

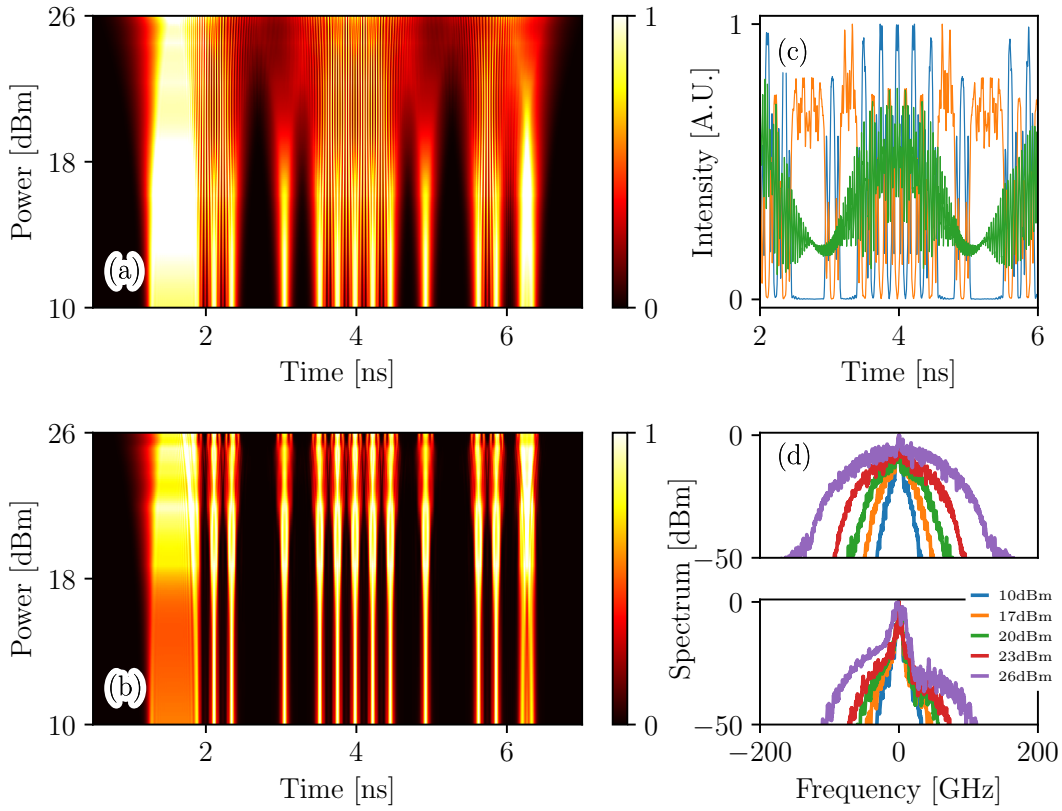

Figure 3.12: Numerical simulation of the evolution of the output intensity profiles as a function of power after propagation in a 50 km TWHD (a) Single component of polarization at the input (b) Both components of polarization at the input (c) Temporal signal for an average input power of 24 dBm after propagation. Green: single polarization component as input, Orange and blue: copropagating orthogonal signals (d) Spectrum evolution with power, without (top) and with (bottom) the second signal copropagating.

The simulation was done with the same fiber parameters and powers as the experiment. The input signals were *data* and $\overline{data}$, each pulse being modeled by a 4^{th}-order super-gaussian. The results can be seen on Fig. 3.12.

Similarly to the experimental results, Fig. 3.12a shows the output intensity profile after the propagation of a single component of polarization. It can be observed that the data are lost once again, due to chromatic dispersion and SPM inducing a deformation of the transmitted signal. Fig. 3.12b shows that when the second polarization component is copropagating in the fiber, effectively inducing the po-

larization switch needed for the generation of PDW, the energy included in the signal is confined to the domains defined by the PDW and very low deformation is observed, allowing for a conservation of the transmitted data. Fig. 3.12c displays the output temporal profiles obtained for an input average power of 24 dBm. It is clearly visible that similarly to the experiment, a single polarization axis propagated is completely deformed after propagation, while when the two axes propagate, the data are conserved, and the interlocking between the two axes can clearly be seen. Finally, the spectra shown in Fig. 3.12d display the same characteristics as the experimental ones, the spectral broadening due to SPM being greatly limited when PDW propagate instead of a simple polarization component.

3.5 Polarization segregation

In order to further assess the soliton characteristics of the PDW, their resilience, strength and stability, an other experiment was performed. In this case, the spontaneous apparition of PDW was observed from a partially incoherent signal.

Indeed, it is well known that when a pulse is close to the soliton solution in the focusing regime of an optical fiber, even if the solution is not perfect, its propagation through the fiber will make the pulse closer to the perfect soliton shape[2]. Similarly to the appearance of soliton like structures during the MI process, here the same phenomenon is expected. When the two orthogonal signals are close to a PDW structure, it is expected for this structure to be enhanced with propagation through the fiber, creating after a while well defined domains, with spontaneous polarization flipping.

In this section, this phenomenon will be studied. The experimental setup will first be explained, before showing the experimental results. After this, extended numerical simulations were performed, based on a thermodynamical approach of the system, expliciting the possibility of apparition of PDW depending on the input state of the system.

3.5.1 Experimental setup

For this experiment, the setup is illustrated on Fig. 3.13. An Amplified Spontaneous Emission (ASE) source (Erbium based optical source in the C-band) is first filtered in the spectral domain to get a 10 GHz bandwidth and divided in two orthogonal replicas thanks to a PWS. Those two replicas are then decorrelated using a different fiber length on each arm (a 1 km long SMF was introduced on one arm of the paths), before being recombined on orthogonal polarizations through two PC (one on each arm) that allows the alignment on the polarization axis of a PBS. The two incoherent waves were then amplified by a 33 dBm EDFA. The

amplified signal was then injected into a 10 km TrueWave fiber, the same type of fiber that was used in Section 3.3. At the output of the fiber, the two signals were demultiplexed by aligning the output signal onto the initial polarization basis using a PC, to observe each polarization component independently after the decoupling through a second PBS. Those signals were both observed simultaneously on a 33 GHz real-time oscilloscope through two 70 GHz bandwidth photodiodes.

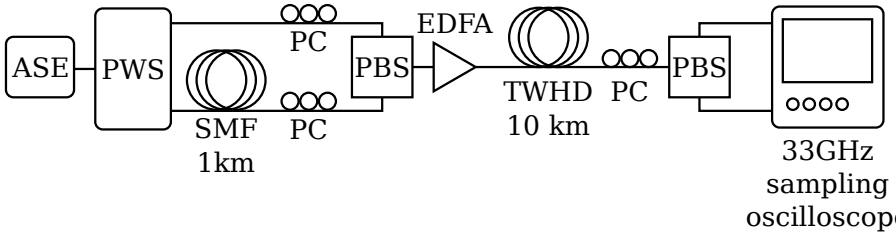

Figure 3.13: Experimental setup used for the observation of spontaneous generation of PDW. ASE: Amplified Spontaneous Emission, PWS: Polarization WaveShaper, SMF: Single Mode Fiber, PC: Polarization Controller, PBS: Polarization Beam Splitter, EDFA: Erbium-doped Fiber Amplifier, TWHD: TrueWave High-Dispersion fiber

3.5.2 Experimental results

In order to assess the actual appearance of PDW, a measurable quantity is needed to estimate of their appearance rate after propagation. This value must take into account both axes of polarization, and the expected structure of the PDW. For this purpose, a cross-correlation function was used which is defined by

$$\mu_{dw}(U,V)(\tau) = \frac{\langle U(t)V(t-\tau)\rangle - \langle U(t)\rangle\langle V(t)\rangle}{\sqrt{\mathrm{Var}(U(t))\,\mathrm{Var}(V(t))}} \tag{3.11}$$

This cross-correlation will be 0 when there is no correlation between the two signals. When the two signals are correlated, the value will get close to 1. Finally, and most importantly in our case, when an anti-correlation appears in between the signals (which is, in our case, a sign of the formation of PDW), the value of μ_{dw} will tend towards -1. One must note that this defines a cross-correlation function which allows to detect both correlation and anti-correlation between the two signals, while Eq. (3.6) only allows to measure the similarity between them. By just calculating this factor, it is possible to measure the appearance of an anti-correlation in between our orthogonal signals precisely, and the amplitude of the value (whether it is close or not to -1) will indicate the strength of the effect.

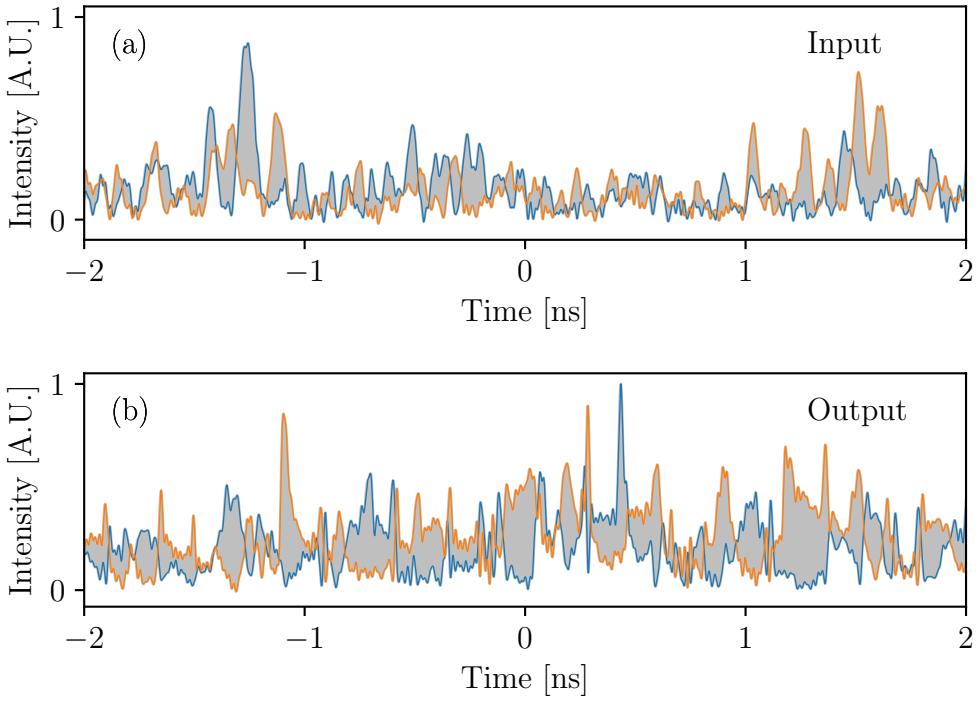

Figure 3.14: Spontaneous generation of PDW from the propagation of two incoherent signals in a 10 km fiber at 28 dBm. (a) Input signals (b) Output signals. The area between the curves is visibly larger than in (a)

Thus, it is considered that the closer to -1 the coefficient is, the better PDW are generated.

On Fig. 3.14a are plotted the input signals. As can be seen, there seem to be absolutely no correlation between the two components, which is what was expected from the individual ASE source. After propagation, the temporal intensity profiles were measured, and plotted on Fig. 3.14b. It can clearly be seen, even only visually, that domains of energy are actually created, and that there tends to be no energy on one of the axes of polarization when there is some on the orthogonal one, highlighting a segregation process. This is a first sign of PDW. But a simple observation is not enough, which is why the correlation coefficient was calculated at input and output.

Fig. 3.15 shows the evolution of the correlation function. As can clearly be seen, while the correlation stays at 0 for the input signal, indicating absolutely no correlation between the two signals, the coefficient dips down to almost -0.5 for a delay of $\tau = 0$. This means that an anti-correlation is actually appearing in

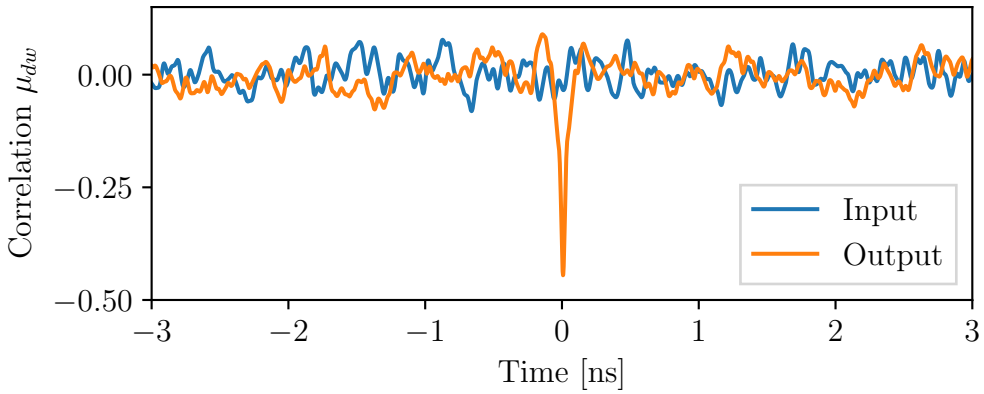

Figure 3.15: Cross-correlation function between the two orthogonal signals, input and output of the fiber for an average power of 28 dBm for a bandwidth of 10 GHz. Input signals spread over 40 ns, no averaging.

between the two axes of polarization, sign of the appearance of PDW. This confirms the previous visual observation that the signals are actually anti-correlated at the output of the fiber. Although the process is not perfect, this experiment shows that the kink solitonic structures are very robust, and that their behaviour corresponds to a soliton, even if the conditions for the soliton structure are not the perfect ones, the signal energy will be redistributed to get as close to the solitonic solution as possible, in this case leading to the spontaneous generation of PDW.

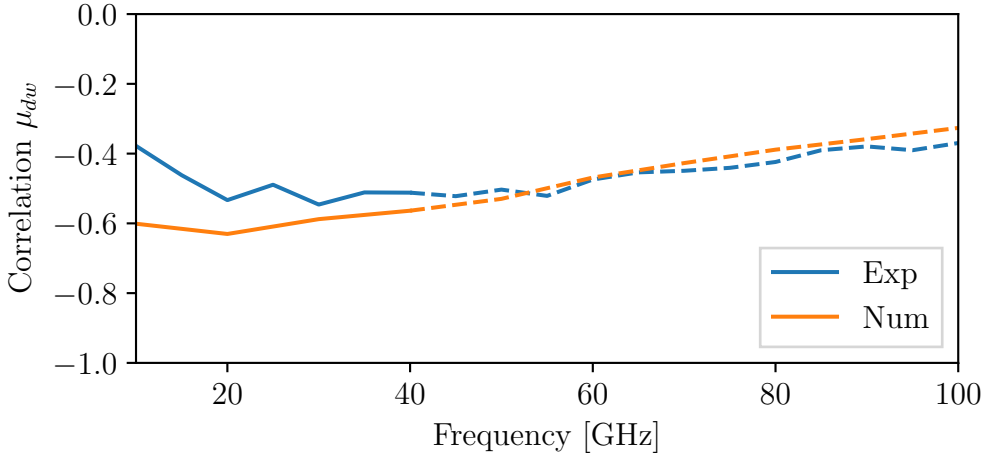

Figure 3.16: Evolution of the correlation coefficient with ASE bandwidth, experimental (blue) and numerical (orange) results for a mean power of 28 dBm.

On Fig. 3.16, the evolution of the cross-correlation coefficient as a function of the ASE bandwidth is plotted. As displayed, the experimental coefficient is shown to first go down with frequency increasing, meaning that the signals are more anti-correlated. It then goes up with the frequency, meaning a reduction of the anti-correlation towards no correlation. It should be noted however that we are limited by the photo-receiver bandwidth to 50 GHz, thus the results above this value may not be accurate. While those results seem validated by the simulations described later in Section 3.5.3, as a good agreement is observed for higher frequencies, there is a discrepancy for lower incoherence.

Finally, a study of the evolution of the cross-correlation coefficient with power was done for an incoherence bandwidth of 10 GHz. As can be observed on Fig. 3.17, as the power increases, the anticorrelation becomes larger, the coefficient going from 0 at 10 dBm down to −0.4 at a power of 32 dBm. As the power increases, so do the nonlinear effects in the fiber, leading to the formation of more PDW which is reflected by this increase in anti-correlation, with an excellent agreement between experimental measurements and numerical simulations.

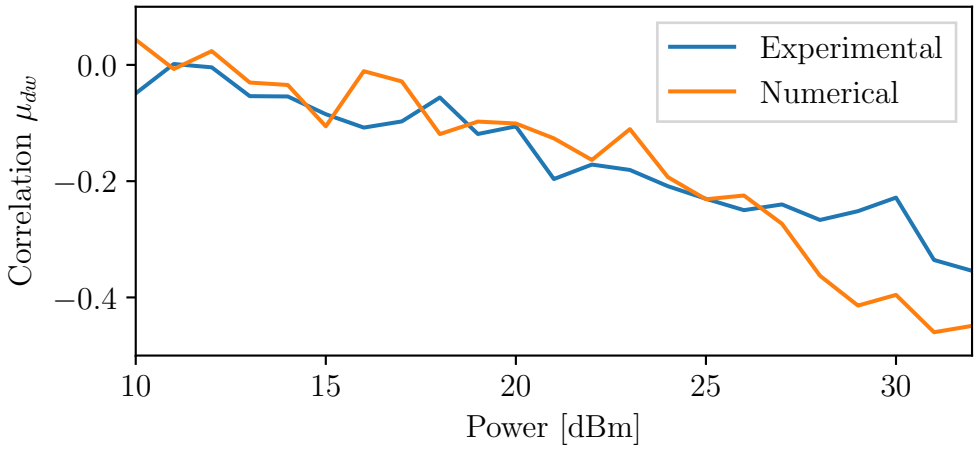

Figure 3.17: Evolution of the correlation coefficient with power, experimentally and numerically, for an incoherence of 10 GHz.

3.5.3 Simulation results

Experiments showed that PDW actually appear out of two orthogonal signals. In order to study this phenomenon in more details, simulations were performed.

In order to have a consistent value to describe the input signal, whether it is incoherent or coherent, a thermodynamical approach is taken in studying the

system, as inspired by the work of Antonio Picozzi[116]. Indeed, the phenomenon of segregation has an origin in thermodynamics. It is actually advantageous, in a thermodynamical sense, for the signal to create this segregation as it increases the amount of disorder. This might appear counter-intuitive, as there seems to be an organization of the signal. However, while the Hamiltonian of the signal will decrease close to the PDW, all the energy is stored in small scale variations, *i.e.* the kinetic energy of the signal, thus increasing disorder.

To implement this approach, the total input signal was described by its Hamiltonian, H, which is defined by the following terms

$$H = H_u + H_v + H_x + E_u + E_v \tag{3.12}$$

where

H Total Hamiltonian

H_u Self-Hamiltonian of the signal u

H_v Self-Hamiltonian of the signal v

H_x Hamiltonian of the interaction between u and v

E_u Kinetic energy of the signal u

E_v Kinetic energy of the signal v

In the case of a weakly nonlinear regime ($E_u + E_v \gg H_x$), the energy per particle E/N (with N the total power of each wave, defined as $N_j = \int |j|^2 \, dt, j = u, v$) provides an appropriate measure of the amount of incoherence, which is related to the normalized spectral bandwidth of the waves, in analogy with kinetic gas theory. For the details on the calculation of the different terms, see Appendix A.

The first objective was to generate signals with an increasing Hamiltonian, in order to see the evolution of the segregation after propagation depending on the Hamiltonian. It should be noted that the total Hamiltonian is a constant value, and so its value is the same at input and output.

First, incoherent signals, with a different bandwidth were input in the simulation, and are described in detail on Fig. 3.18. This allowed to get an Hamiltonian ranging from 3×10^{-3} to 3×10^{-2} and would allow for higher Hamiltonian values. Signals with different bandwidths are illustrated on Fig. 3.18a. Mathematically, the signal was generated from a gaussian spectrum of different bandwidths, with a random phase, as described by Eq. (3.13)

$$A(t, z) = \mathcal{F}^{-1} \left\{ \exp(-\omega^2 / 2\sigma^2) \exp(2i\pi\varphi_{\text{rand}}) \right\} \tag{3.13}$$

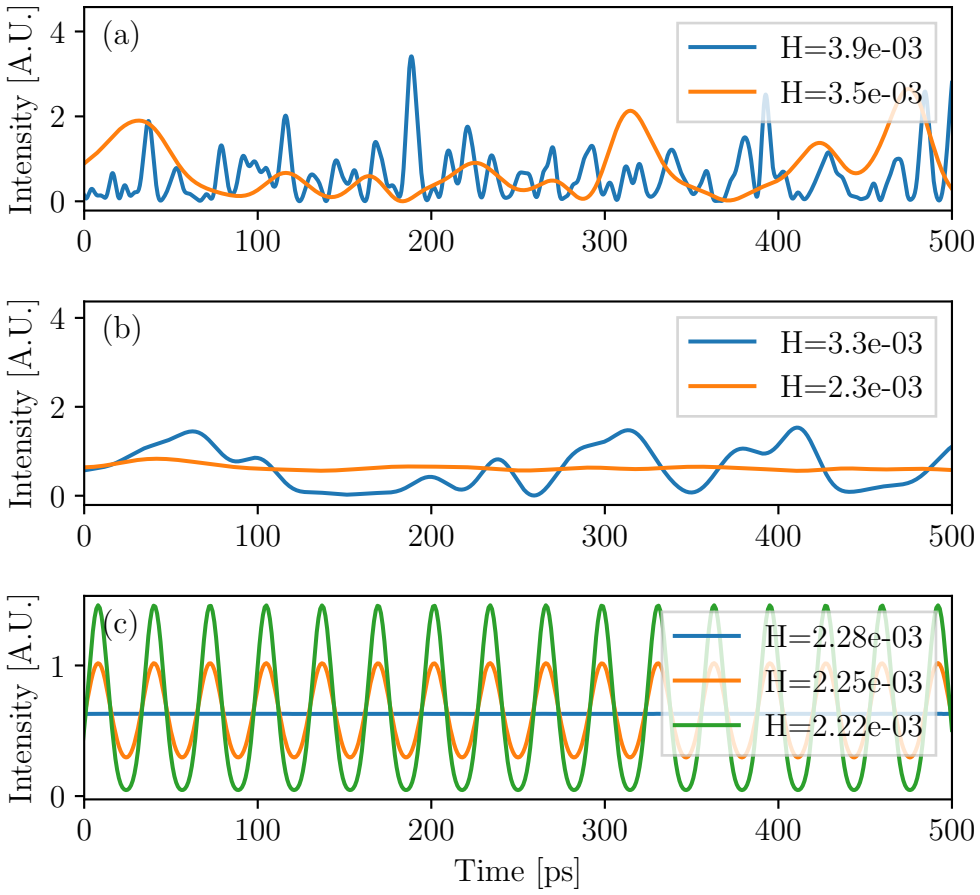

Figure 3.18: Illustrations of the different kinds of input used to get the full ranges of Hamiltonian and cross-correlation coefficient. (a) Incoherent signal at multiple bandwidths (50 GHz in blue, 10 GHz in orange) (b) Incoherent + continuous, with different ratios (1% continuous in blue, 100% continuous in orange) (c) Continuous + Sinusoidal, with different sinusoid depth (0% depth in blue, 30% depth in orange, 100% depth in green, the sinusoid with a frequency of 10 GHz are applied to the electric field)

where $\mathcal{F}$ is the Fourier transform operator, ω is the frequency of the signal, σ is the gaussian standard deviation and φ_{rand} represents the random phase of the signal.

To further reduce the Hamiltonian, an other approach is needed. So the second type of signal that was simulated to propagate was also based on an incoherent signal, but with an added continuous component, as described mathematically by Eq. (3.14).

$$A(t,z) = \mathcal{F}^{-1}\left\{\exp(-\omega^2/2\sigma^2)\exp(2i\pi\varphi_{\text{rand}})\right\} + C \tag{3.14}$$

with C being the continuous component of the signal. The ratio of continuous signal with incoherent signal allowed for the change of Hamiltonian of the signal, and increasing the ratio of continuous signal decreased the Hamiltonian. By doing this, it was possible to reach values of Hamiltonian ranging from 3×10^{-3} to 2.3×10^{-3}. An illustration of the evolution of the ratio is shown on Fig. 3.18b. This last approach however did not lead to a cross-correlation of -1, only to go down to -0.9.

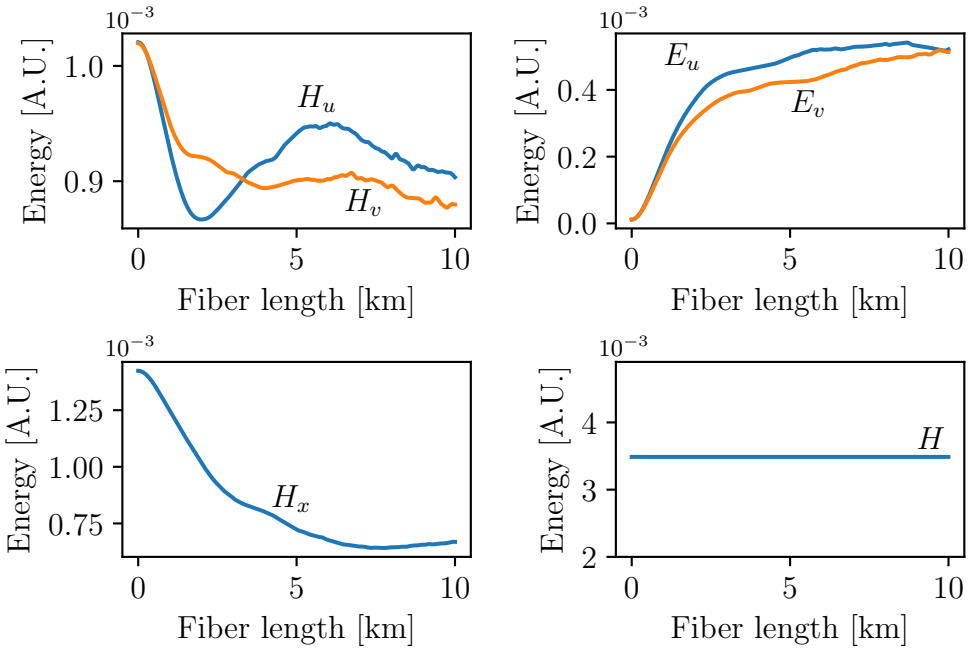

Figure 3.19: Evolution of the different energies during the simulation of the propagation in the fiber for a pure incoherent signal at a bandwidth of 10 GHz. (a) Self-Hamiltonian on each polarization axis (b) Kinetic energy on each polarization axis (c) Interaction Hamiltonian (d) Total Hamiltonian.

In order to achieve this value, a last approach was used. In that case, instead of a ratio of continuous with incoherent signal, a mix of continuous and sinusoidal signal was used, as explicited mathematically in Eq. (3.15).

$$A(t, z) = D * \sin(t) + C \tag{3.15}$$

where $0 \leq D \leq C$ is the depth of the sinusoidal wave and C the continuous component of the signal. By increasing or decreasing the ratio of sinusoidal signal added to the continuous signal, it was possible to get the missing points to get a complete curve of the evolution of the correlation with the Hamiltonian. In fact,

this is very similar to seeding the PMI process. This approach is illustrated in Fig. 3.18c.

The whole range of interest of the Hamiltonian and the cross-correlation coefficient being filled, the propagation of the different signals was simulated using the model described by Eq. (3.7) and Eq. (3.8), with $L = 10\,\mathrm{km}$, $\gamma = 2.5\,\mathrm{W^{-1}\,km^{-1}}$, $\beta_2 = 18.5\,\mathrm{ps\,km^{-2}}$ and using a cross-correlation coefficient of $C_{XPM} = 1.3$. It must be noted that the simulations here were done without taking the losses into account. Adding those to the simulations would only have as an effect to get the total Hamiltonian to decrease linearly along the fiber, making it possible to compare with the experimental Hamiltonian.

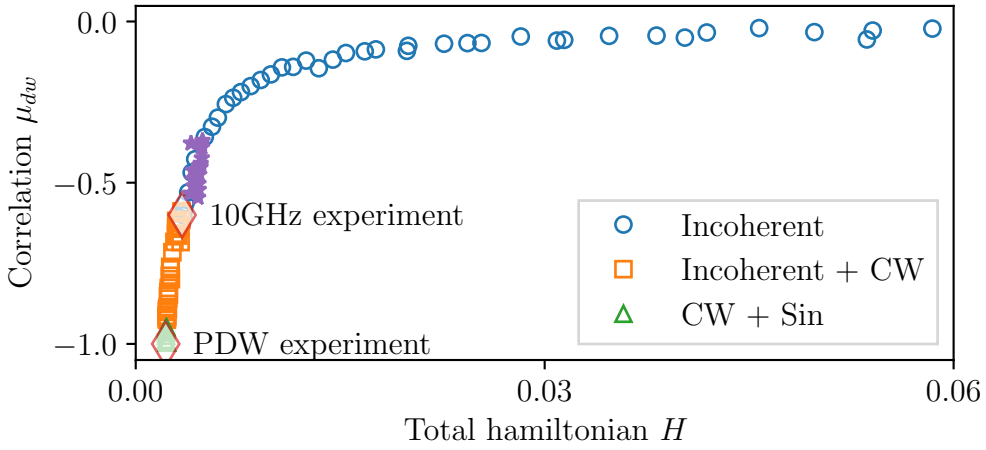

Figure 3.20: Evolution of the cross-correlation coefficient with the Hamiltonian of the signal. Continuous + sinus are plotted as triangles, incoherent + continuous are plotted as squares, pure incoherent are plotted as circles. The stars correspond to the experimental cases of Section 3.3 and Section 3.5.

On a single simulation, it is interesting to note the evolution of the different energies during propagation in the fiber. Fig. 3.19a shows the evolution of the Hamiltonians of each signal. These Hamiltonians will evolve differently depending on the input signal, and can either increase or decrease. On Fig. 3.19b, there is indeed an increase of kinetic energy of both signals, as was predicted previously by the thermodynamical approach. Figure 3.19c shows that the interaction Hamiltonian diminishes during propagation. Indeed, as more PDW are formed, an anticorrelation appears in the signal, reducing the effective interactions in between the two signals, thus reducing the Hamiltonian of interaction. Finally, it can be noted on Fig. 3.19d that the total Hamiltonian is indeed constant during propagation. While the ensemble of figures depicted in Fig. 3.19 is only for a single

simulation, with a given input having a given Hamiltonian, the same tendencies were found for each input configuration.

After simulating the propagation of all of the signals, the evolution of the cross-correlation coefficient was studied as a function of the total Hamiltonian. This evolution is shown in Fig. 3.20. It can be seen that the lower the level of the Hamiltonian, the lower the cross-correlation coefficient, and the higher segregation is achieved. For the lower values of the Hamiltonian, the segregation is not actually spontaneous, as the signal is already given a segregation pattern at the input. By placing the two experimental points previously obtained, it can be seen that the numerical model seems to be in excellent agreement with our experimental results.

3.6 Polarization Modulation Instability in telecommunication fibers

As described in Section 3.1, Haelterman et al. explained their observations of vectorial structures similar to the PDW by attributing them to the phenomenon of modulational instability demonstrated by Berkhoer and Zakharov[12]. The model explicited implies the use of an isotropic fiber, or a fiber that could be considered isotropic. However, the experiments performed in this chapter were done in fibers that cannot be considered isotropic, due to their length. This was also proven by the fact that the cross-correlation coefficient factor C_{XPM} was not found equal to 2 in Section 3.3.3. The phenomenological model introduced previously that well reproduces our experimental results does not explain physically the emergence of the PDW however, raising the question of the cause of the emergence of the kink solitons that were observed.

To answer this question, it will be shown that although the PMI can indeed be observed in short fiber lengths, it quickly disappears as expected theoretically. The longer fibers, however, displayed unexpected new sidebands that could not be accounted for previously. A new theory, taking into account the fabrication method of the fibers, was then developed that explains the formation of the PDW and the sidebands observed in this part.

3.6.1 PMI theory

Polarization Modulation Instability, also called vector modulation instability, extends from the scalar modulation instability, which was developed in Section 1.1.4. This expansion takes into account that the input signal excites both axes of polarization of the fiber, coupled by the cross-phase modulation components in the equations. Three different cases were distinguished, depending on the type of fiber studied, whether the fiber is low or highly birefringent, or isotropic. The fiber

used during the experiments having very low PMD, it cannot be considered as a highly birefringent fiber. Thus, only the low-birefringence and isotropic cases will be detailed.

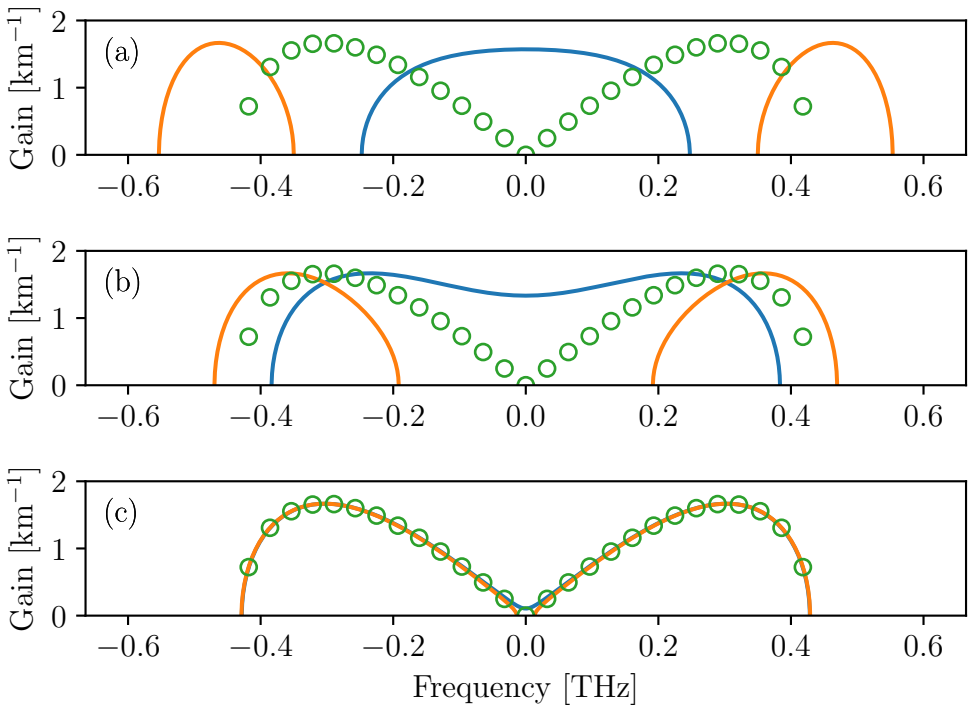

Figure 3.21: PMI bands for decreasing birefringence (from top to bottom). Blue and orange: central and side gain bands for a low-birefringence fiber, Green circles: gain bands for an isotropic fiber. $\gamma = 2.5\,\mathrm{W^{-1}\,km^{-1}}$, $\beta_2 = 18.5\,\mathrm{ps\,km^{-2}}$, $P = 1\,\mathrm{W}$

In a low-birefringence fiber, two main amplification bands generated by PMI can be observed, a large central one, centered on the pump frequency, and two distinct smaller bands on the sides, depending on the axis of observation. The shape of the bands is displayed on Fig. 3.21a. To define those bands were introduced multiple values. The gain $g(\Omega)$, that describes the gain over the frequency band. For the central band, on the fast axis of the fiber, the gain was calculated to be[2]

$$g(\Omega) = |\beta_2| \sqrt{(\Omega^2 + \Omega_{c2}^2)\,(\Omega_{c1}^2 - \Omega^2)} \tag{3.16}$$

with

$$\Omega_{c1} = \left(\frac{4\gamma}{3\beta_2}\right)^{1/2} \sqrt{P_0 - P_{\mathrm{cr}}} \tag{3.17}$$

$$\Omega_{c2} = \left(\frac{2\Delta\beta}{\beta_2}\right)^{1/2} \tag{3.18}$$

$$P_{\text{cr}} = \frac{3\,|\Delta\beta|}{2\gamma} \tag{3.19}$$

Where P_0 is the input power of the signal. From Eq. (3.16), it can easily be deduced that gain on the central band will only appear when $0 < |\Omega| < \Omega_{c1}$. Thus, Ω_{c1} is the cut frequency of the central band. Moreover, Ω_{c1} is a real number only in the case when $P_0 > P_{\text{cr}}$, as seen from Eq. (3.17), meaning that the input power must be over a given power that depends on the birefringence of the fiber and its nonlinearity. On the other hand, on the slow axis, the gain of PMI is defined by the gain

$$g(\Omega) = |\beta_2| \sqrt{(\Omega^2 - \Omega_{c2}^2)\,(\Omega_{c3}^2 - \Omega^2)} \tag{3.20}$$

with

$$\Omega_{c3} = \left(\frac{4\gamma}{3\beta_2}\right)^{1/2} \sqrt{P_0 + P_{\text{cr}}} \tag{3.21}$$

From Eq. (3.20) can be derived that the side bands gain will only appear when $\Omega_{c2} < |\Omega| < \Omega_{c3}$, making Ω_{c2} the low cut frequency and Ω_{c3} the high cut frequency of the band gain.

In the case of an isotropic fiber, which the fiber used during those experiments can be considered to be, the model that was developed for the low-birefringence fibers holds true. By setting $\Delta\beta = 0$, one can easily deduce that $P_{\text{cr}} = 0$, thus $\Omega_{c2} = 0$ and

$$\Omega_{c1} = \Omega_{c3} = \Omega_c = \left(\frac{4\gamma}{3\beta_2} P_0\right)^{1/2} \tag{3.22}$$

reducing the MI gain to

$$g(\Omega) = |\beta_2|\,\Omega\sqrt{\Omega_c^2 - \Omega^2} \tag{3.23}$$

This gain equation is similar to the scalar case, thus creating two bands that are displayed in Fig. 3.21b. However, the bands in this case can appear even in the case of a fiber with normal dispersion, while it is impossible in the scalar case. It must be noted that as the fiber is isotropic in this case, the only requirement for these equations to hold true is to have a linearly polarized signal as input, but their orientation is not important, as the fiber has no low or fast axis. However, it must be noted that the PMI develops orthogonally to the pump wave.

It can be noticed from Fig. 3.21 that while the bands are well separated for a low-birefringence fiber with high enough birefringence, the bands get closer to the isotropic model as the birefringence is reduced, until a perfect overlap between the bands is achieved.

3.6.2 Experimental observations

The first idea in order to explain the apparition of the PDW was indeed that the fiber that was used had so low PMD that even if it was very long, PMI would still appear. However, PMI bands did not appear in the output spectrums of the previous experiments due to Raman and SBS effects. To be able to start observing PMI, a 50 m long part of the TrueWave fiber was cut out, and unwrapped of the fiber spool, and put without constraints on a table, in a very large circle (with a diameter over 50 cm). Indeed, the PMI is very sensitive to the birefringence, and a small constraint of the fiber from being wrapped on a spool could reduce greatly the PMI gain. By unspooling it, those constraints were removed, theoretically increasing the gain of the PMI.

Experimental setup

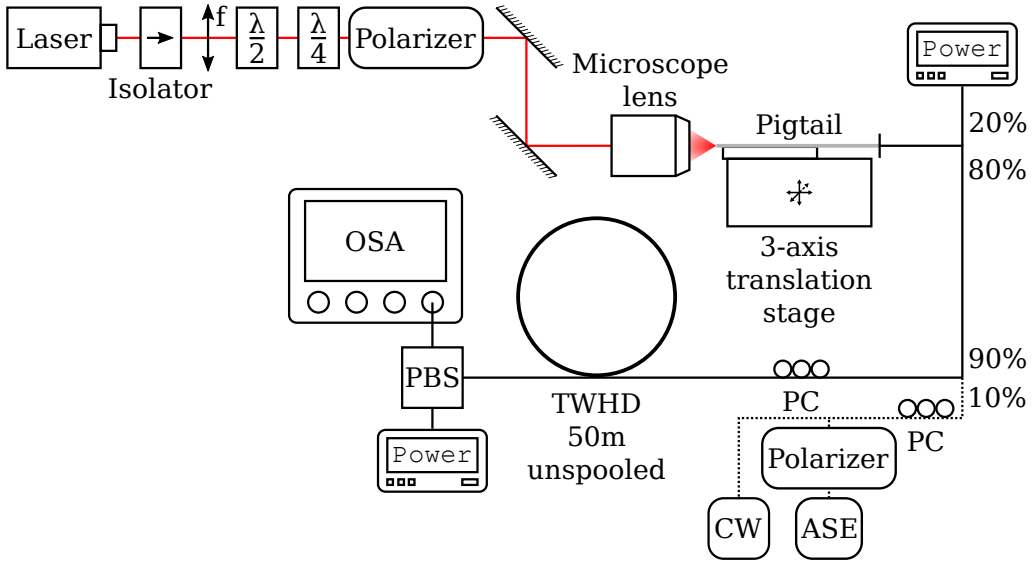

Figure 3.22: Experimental setup used in order to observe PMI. $\lambda/2$: Half-wave plate, $\lambda/4$: Quarter-wave plate, Microscope lens 10x, f = 10 cm, Amplified Spontaneous Emission (ASE), continuous wave (CW), Polarization Controller (PC), TrueWave High-Dispersion fiber (TWHD), Polarization Beam Splitter (PBS), Optical Spectrum Analyser (OSA)

The experimental setup can be seen on Fig. 3.22. A high peak-power nanosecond pulsed laser was sent through an isolator to avoid backwards reflections that would induce power variations of the laser. The beam is then sent through a focusing lens, in order to create a parallel beam. It then goes through a half-wave plate combined to a polarizer to modulate the output power of the laser, then through

a quarter wave plate that changes the polarization of the beam. Two mirrors are then used in order to get the beam through a microscope objective, used for injection into a fiber pigtail fixed onto a manual 3-way translation stage, to adjust the position for the best injection. The pigtail can then be connected to a fibered system, of which the elements can easily be switched, giving the system more flexibility. The pump is then divided using a 80:20 coupler, 20% of the signal going to a power meter allowing to measure the input power with no modification to the system. This ensures an easy and consistent measurement of the power along with the spectrum of the signal at the fiber output. The remainder of the pump then goes through a 90:10 coupler, in which it can be combined with either a tunable CW laser or a filtered and polarized ASE source, each of which polarization can be adjusted using a PC, allowing for the seeding of the pump on either axis of polarization. The whole signal then goes through a PC before being injected into an unspooled fiber of 50 m, 200 m, 500 m or a 1000 m formed by two of the previous 500 m fibers spliced together. The output signal is then demultiplexed using a PBS after alignment using an other PC. Each arm is observed independently, one on a power meter, that is used for alignment, the other on an OSA, to observe the spectrum of the signal after propagation.

Experimental results

When using a 50 m fiber, it was first possible to observe spontaneous PMI bands by simply sending a linearly polarized signal propagating in the fiber, adjusting the input State of Polarization (SOP) to be linear. As can be seen on Fig. 3.23a, the output of the 50 m fiber actually shows bands that are very consistent with bands of PMI. Indeed, in the case of an isotropic fiber, which was considered here due to the form of the band, the maximum gain frequency Ω_{max} can be calculated easily[2]

$$\Omega_{\text{max}} = \pm\frac{\Omega_{\text{c}}}{\sqrt{2}} = \pm\left(\frac{2\gamma P_0}{|\beta_2|}\right)^{1/2} \tag{3.24}$$

where $\Omega_{\text{c}}^2 = 4\gamma P_0/|\beta_2|$ is the cut frequency of the PMI bands, as seen previously in Eq. (3.22). As can be observed later in Fig. 3.27, for a fiber of 50 m, the position of the side bands are very close to the theoretical model, thus validating that the 50 m fiber can be considered isotropic. It should be noted that this behaviour was observed in the 50 m fiber wrapped on a standard spool as well as on the unwrapped fiber. Figure 3.23b shows the output of the fiber on the two orthogonal axes of polarization, one axis corresponding to the pump SOP. It can be seen that as expected of the PMI, the bands that appeared are orthogonal to the pump axis. Although the pump does not completely disappear on the PMI axis, there is a 10 dB attenuation on the pump peak. To observe the gain spectrum more easily,

an ASE seed was sent on the axis orthogonal to the pump, thus allowing to observe the gain spectrum at much lower pump power, as can be seen on Fig. 3.23c. This also helps limiting the Raman scattering created using a peak pump power ranging from 92 W to 228 W.

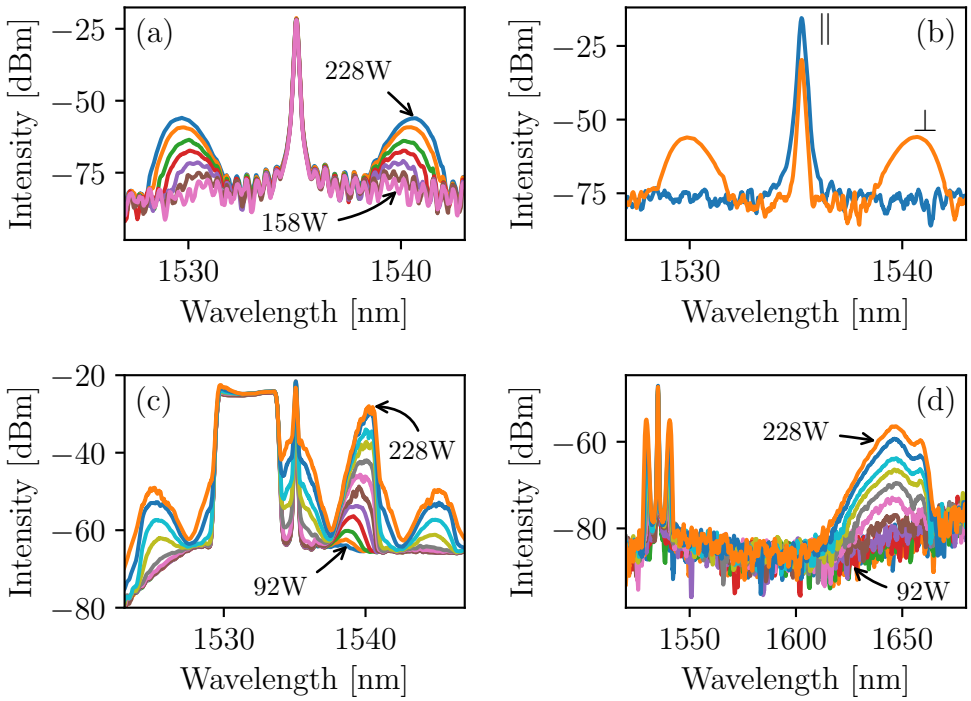

Figure 3.23: Spontaneous PMI in a 50 m fiber. (a) Evolution of the PMI bands with input power (peak power ranging from 158 W to 228 W) (b) Output on each axis of polarization. The bands appear on the polarization axis orthogonal to the pump polarization axis (c) ASE seeded gain spectrum (peak power ranging from 92 W to 228 W) (d) Raman spectrum (peak power ranging from 92 W to 228 W)

As the bands were observed on a 50 m fiber, the length was increased to see whether they keep appearing. For that, a 200 m-long fiber was unwrapped on the table, the same way the 50 m fiber was, in order to remove the constraints that could appear from spooling the fiber. The same experiment was then performed, varying the pump power and observing the output of the fiber on the two axes of polarization of the output PBS aligning one of the axes with the pump. As can be seen on Fig. 3.24a, it is still possible to observe spontaneous PMI in this fiber, see it evolve with power according to the theory when considering an isotropic fiber and observe the apparition of harmonics of the PMI, indicating a good gain of the PMI up to a certain power level. It can be observed that when the power reaches

a certain level, the gain spectrum stops to grow. This comes from the apparition of Raman scattering, which depletes the pump thus effectively capping the power available to be used in the PMI process. The apparition of Raman scattering was indeed observed, as can displayed by Fig. 3.24c. It can be seen that the Raman scattering is indeed having a huge impact on the pump depletion, as a second order Raman band appears after the first one, indicating significant Raman conversion, thus significant pump depletion.

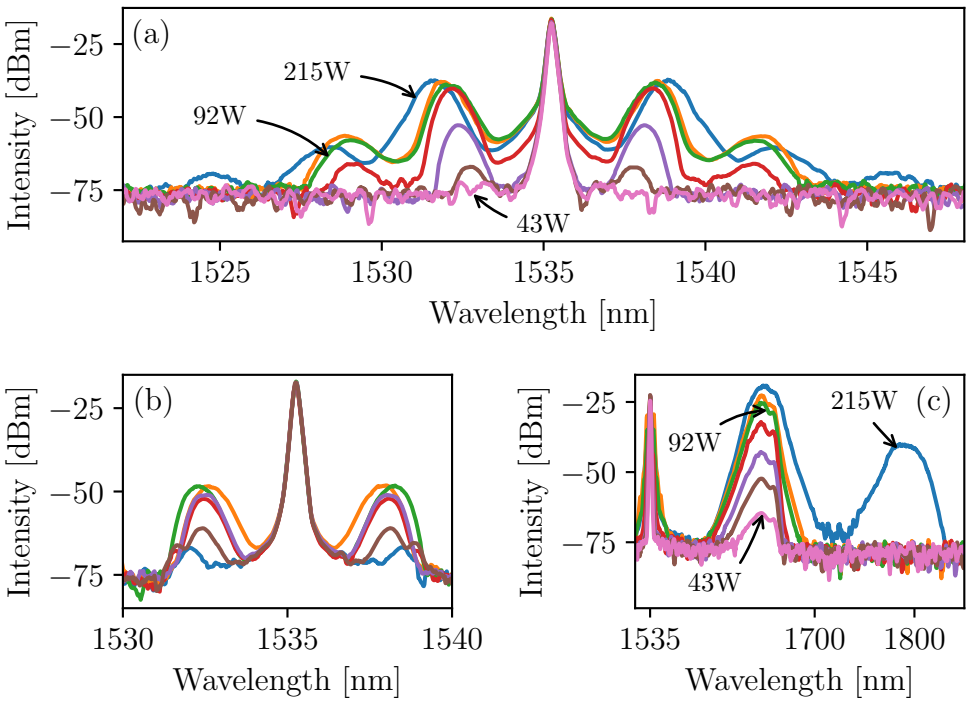

Figure 3.24: Sidebands evolution in a 200 m long fiber. (a) Evolution of the PMI bands with input power (b) Different gain spectrums at a peak power of 76 W for varying input polarization (c) Raman scattering at different pump powers. The peak power for the spectra plotted in (a) and (c) are 43 W, 55 W, 68 W, 80 W, 92 W, 105 W and 215 W, respectively

PMI bands in the 200 m fiber were observed, so the next objective was to observe the evolution of this gain in a longer fiber, namely 500 m. For this, unwrapping the fiber directly on the table would have been difficult, as the torsion induced by hand-unwrapping the fiber could create knots very easily in the unwrapped fiber. Thus, in order to study the PMI in longer fiber, spools of fibers with a diameter of 45 cm and a width around 40 cm were used. The fibers were very slowly respooled, with as low fiber tension as possible and no fiber empiling

to reduce the constraints to the minimum. Using this technique, two spools of 500 m-long fibers were created, then fitted with connectors for easy switching.

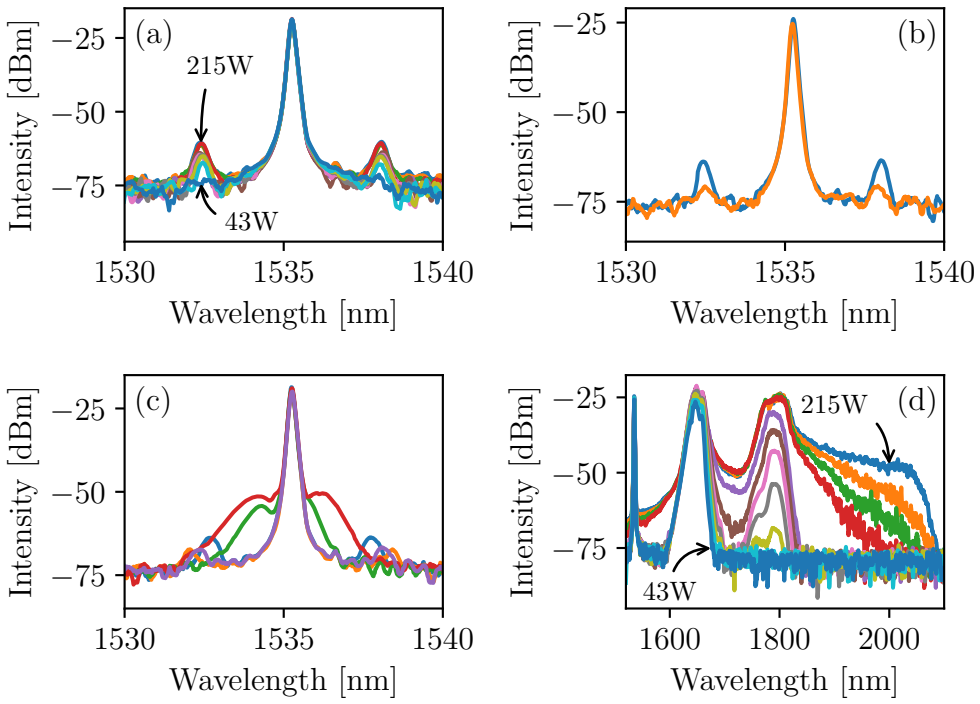

Figure 3.25: Sidebands evolution in a 500 m fiber. (a) Evolution of the bands with pump power (b) Output after PBS demultiplexing, on each axis of polarization at the output of the last PBS. (c) Different bands created depending on the initial polarization of the signal (d) Raman spectrum evolution with pump power For (a) and (d), the peak power ranges from 43 W to 215 W

As can be seen on Fig. 3.25a, PMI bands are still observed but the position of these MI are found to be independent of the injected power, which could be explained by the large amount of Raman scattering generated within the fiber, as seen on Fig. 3.25. More than that, the bands clearly do not have the shape of bands of PMI in an isotropic fiber. However, as was shown in [2], two other cases of PMI can be considered, one being for a low birefringence fiber, the other for high birefringence. If the fiber is highly birefringent, the PMI bands that appear would, theoretically, appear one on the fast axis of the fiber, the second on the slow axis. However, it was observed during the experiment that the two bands always appear. The case of highly birefringent fiber can thus also be excluded. The last case, for low birefringent fibers is still plausible but unlikely considering the manufacturing process.

Theory indicates that a central band forms, around the pump, and two sidebands are created. In the case of this experiment though, multiple issues arise that make it hard to conclude that these are similar to the ones predicted in the low birefringence model. First, even if the pump could be considered large, there is no significant broadening with the increasing power, which would happen in the case of a low birefringent fiber. As can be seen here from Eq. (3.21), the lowest value for the upper cut frequency is obtained for $P_{cr} = 0$ (which would be the isotropic case). In this case, it was calculated to be, for an input power of $P_0 = 200\,\mathrm{W}$, $\Omega_{c3,th} = 6\,\mathrm{THz}$. However, from the experiment, the higher cut frequency was measured, for the same power to be around $\Omega_{c3,exp} = 2.7\,\mathrm{THz}$, hence twice as low as the minimum cut power, making it impossible for this band to come from the PMI generated in a low birefringent fiber.

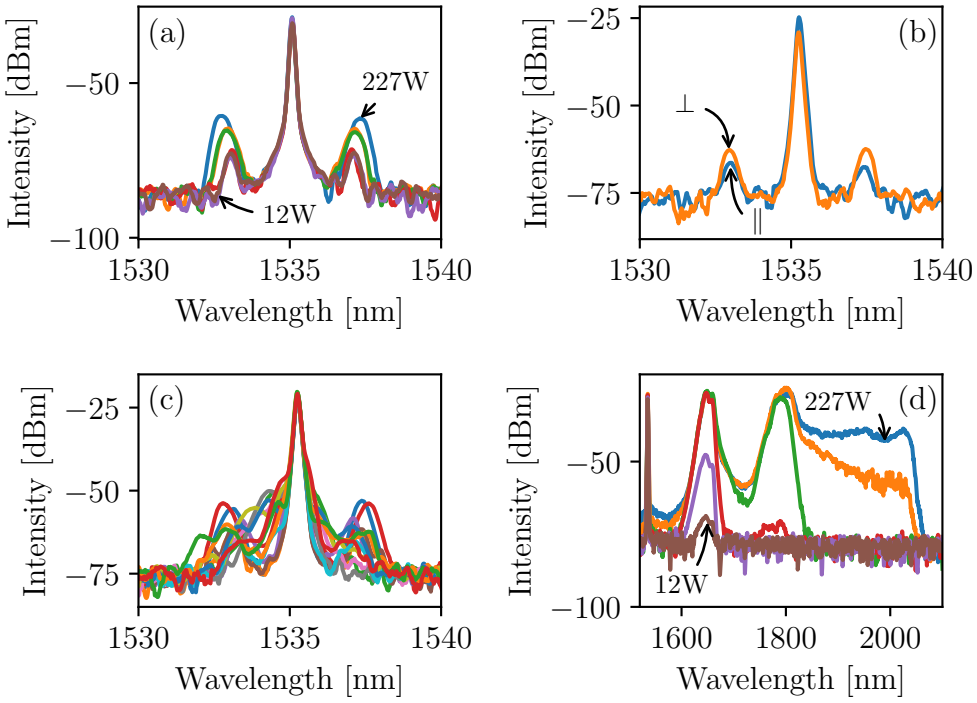

Figure 3.26: Sidebands evolution in a 1000 m fiber. (a) Evolution of the bands with pump power (b) Output after PBS demultiplexing, on each axis of polarization at the output of the last PBS. (c) Different bands created depending on the initial polarization of the signal (d) Raman spectrum evolution with pump power For a and d, the peak power ranges from 12 W to 227 W

In order to understand better where those bands come from, both 500 m fibers were spliced together, thus forming a 1000 m fiber, and the same experiment as

described previously was repeated. As can be seen on Fig. 3.26a, the bands that were previously observed in the 500 m were also still observed. Similarly to previously, different bands were also observed, depending on the polarization input, as illustrated by Fig. 3.26b. Fig. 3.26c shows the evolution of the Raman spectrum with input power, displaying the start of a supercontinuum generation, indicating a highly significant depletion of pump power. Finally, Fig. 3.26d show the output of the fiber after polarization demultiplexing, in order to observe the axis of the pump and its orthogonal axis independently. However, there is no significant difference between the two, except a small decrease in the sidebands gain.

It seems, after those experiments, that the fiber that was used can be considered isotropic up to almost 200 m, but that an other type of sidebands appears that is not accounted for by PMI. It can be seen on Fig. 3.27 that the peaks position for $L = 50\,\mathrm{m}$ follow the isotropic theory quite well, and that it does well at low power for $L = 200\,\mathrm{m}$, but then deviates from the theory completely. It appears that the peak shift from the pump is reduced with the fiber length, but that the peak position does not change when increasing the pump power.

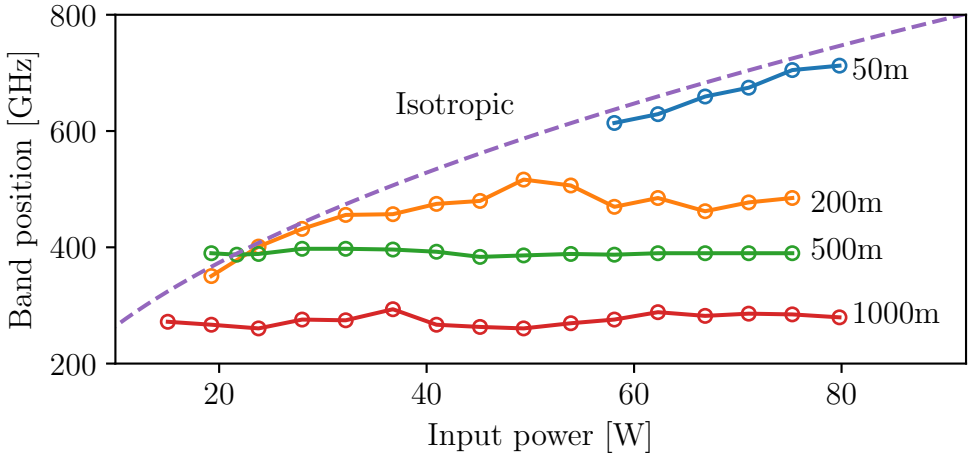

Figure 3.27: Evolution of the observed band position, with the theoretical isotropic model band position included. (in dashed line)

These observations validate the theory that the PDW comes (completely) from the PMI and undermine the Manakov model for longer modern telecom fibers. Indeed, by using the theory developed by Haelterman et al., the fiber must be isotropic in order to observe PDW. Even if the phenomenological model provided by Eq. (3.7) and Eq. (3.8) has proven very accurate, it does not explain where the extra coupling between the two orthogonal polarizations come from. Now, these experiments show that the XPM coefficient of modern telecom fibers is slightly

higher than the 1 commonly used in the Manakov model. Thus, the next section will develop a new model that helps explain the formation of the PDW and the sidebands that were observed in this section.

3.6.3 The SPUN model

The observations of the PDW question the validity of the usual Manakov model, that is commonly accepted to describe the propagation of light in standard telecommunication optical fibers, like the fiber that was used in those experiments. It was supposed previously that contrary to what was initially suggested, the PDW do not originate from PMI induced in the fiber, as the fiber cannot be considered isotropic either on 10 km nor on 50 km. However, several contacts with the manufacturer OFS, it was found that in order to decrease those fiber birefringence, the fiber undergoes a specific process of spinning during fabrication, that induces a fast spinning of the birefringence axes of the fiber[117–122]. This fast spinning induces an averaging of the natural birefringence of the fiber, thus limiting greatly the PMD. One spinning profile that is commonly used has a sinusoidal shape, that is described by a rotation of the birefringence axes following the angle α defined by

$$\alpha(z) = \alpha_0 \sin(2\pi z/L_{spin}) + \eta(z) \tag{3.25}$$

where L_{spin} is the smallest spatial scale of the problem, usually in the order of a few meters, α_0 is the amplitude of the spinning which can be as large as a few hundreds rad m^{-1}[122]. The stochastic contribution $\eta(z)$ cannot be avoided, as it originates from and represents the residual natural fiber birefringence fluctuations. This random function, $\eta(z)$ has a theoretical mean of 0, and can be characterized by a correlation function $R(z/L_c)$, where L_c is the correlation length of the birefringence fluctuations. Note that the random contribution can be considered as a perturbation with respect to the imposed sinusoidal spinning $\eta_0 = \sqrt{\langle \eta^2 \rangle} \ll \alpha_0$. By using a homogenization theorem[123] and the Jacobi extension $\exp\left(2i\alpha_0 \sin(2\pi z/L_{spin})\right) = J_0(2\alpha_0) + \sum_{n=1}^{\infty} J_n(2\alpha_0)[e^{inkz} + (-1)^n e^{-inkz}]$, light propagation in the fiber can be shown to be described by the following reduced model:

$$\begin{aligned} i\frac{\partial \tilde{u}}{\partial z} &= \frac{\beta_2}{2}\frac{\partial^2 \tilde{u}}{\partial t^2} - \frac{\Delta\beta}{2} J_0(2\alpha_0)\,\tilde{v} + \varepsilon\tilde{u} - \frac{2\gamma}{3}\left(|\tilde{u}|^2 + 2|\tilde{v}|^2\right)\tilde{u} \\ i\frac{\partial \tilde{v}}{\partial z} &= \frac{\beta_2}{2}\frac{\partial^2 \tilde{v}}{\partial t^2} - \frac{\Delta\beta}{2} J_0(2\alpha_0)\,\tilde{u} - \varepsilon\tilde{v} - \frac{2\gamma}{3}\left(|\tilde{v}|^2 + 2|\tilde{u}|^2\right)\tilde{v} \end{aligned} \tag{3.26}$$

where $\tilde{u}$ and $\tilde{v}$ refer to the circular polarization components of the filed, $\Delta\beta$ is the propagation constant difference between the axes, $J_0(x)$ is the zeroth-order Bessel function of the first kind[121] and $\varepsilon(z) = \partial_z \eta(z)$ models the random contribution of the birefringence. As revealed by Eq. (3.26), the fast fiber spinning introduces a controlled polarization mode coupling through an effective beat length, defined as $L_{\mathrm{B}}^{\mathrm{eff}} = 2/\left[\Delta\beta J_0(2\alpha_0)\right]$. In the experiments of this chapter, the nonlinear and dispersive effects act in the km range, while the correlation length of polarization fluctuations ($L_c \sim 50$ m) is typically much shorter than the effective beat length, $L_{\mathrm{c}} \ll L_{\mathrm{B}}^{\mathrm{eff}}$, with $L_{\mathrm{B}}^{\mathrm{eff}}$ of a few hundred meters. In this way, random birefringence

fluctuations are essentially averaged out during the propagation. To properly understand such an averaging process, we follow the general procedure originally introduced by Wai and Menyuk[53] to describe the distribution of the Stokes vector of the optical field over the Poincarré sphere through analysis of the effective birefringence ($L_{\mathrm{B}}^{\mathrm{eff}}$) and random birefringence (L_{c}). Making use of the diffusion approximation theorem[124], a Fokker–Planck-like equation governing the evolution of the probability density of the Stokes vector on the surface of the Poincarré sphere was derived. This equation reveals two fundamental limiting cases. First, when $\left(L_{\mathrm{B}}^{\mathrm{eff}}\right)^2 / \left(\psi(\eta_0) L_{\mathrm{c}}\right) \ll L_{\mathrm{nl}}$, with $\psi(\eta_0) = 2\exp\left(-4\eta_0^2\right) \int_0^\infty \sinh^2\left(2\eta_0^2 R(s)\right) \mathrm{d}s$, then the Stokes vector becomes uniformly distributed over the Poincaré sphere before the onset of nonlinear effects. In this way, the averaging of the nonlinear terms leads to the usual Manakov system[53,125]. On the other hand, when $\left(L_{\mathrm{B}}^{\mathrm{eff}}\right)^2 / \left(\psi(\eta_0) L_{\mathrm{c}}\right) \gg L_{\mathrm{nl}}$, it is possible to show that the optical field is governed by a set of equations formally analogous to those of a low birefringent (or isotropic) fibre, with an effective birefringence length, $L_{\mathrm{B}}^{\mathrm{eff}} \exp\left(2\eta_0^2\right)$. The experimental observations from this chapter place modern manufactured optical fibers between those two limits. Unfortunately, the evolution of the optical field in this intermediate regime cannot be described by deterministic equations, but by a set of coupled stochastic nonlinear Schrödinger equations.

3.7 Conclusion

In this chapter, the generation and propagation of PDW was studied. A first experiment allowed, through the creation of kink soliton and their propagation in a TWHD fiber, to confirm their solitonic nature, in spite of their theoretical seemingly impossible existence. A phenomenological model[91] that allows for their formation was successfully fitted to the experimental results, yielding a cross-correlation coefficient of $C_{\mathrm{XPM}} = 1.3$.

As the structures seemed to be localized in time, and were proven stable through propagation, an NRZ-encoded bit signal representing the word 'PETAL' encoded in ASCII was transmitted, by sending its complementary wave on an orthogonal SOP, in order to create the kink structures that lead to the creation of PDWs. A successful propagation of this signal through 50 km of fiber confirmed the individual and localized nature of the PDWs. This experiment also confirmed the possible application of PDW for telecom applications and propagation of pulses in highly nonlinear regime in normal dispersive fibers.

Due to the resilience of the PDW that was observed through the two previous experiments, it was suspected that the structures would appear spontaneously from an incoherent signal during propagation. By sending two uncorrelated signals copropagating on two axes of polarization of a 10 km TWHD fiber, a segregation

phenomenon was observed and a cross-correlation coefficient (Eq. (3.11)) was used to quantify the segregation. The system was then reduced to a thermodynamical system, allowing for the measurement of the disorder of the signal through its Hamiltonian, and simulations showed the expected evolution of the segregation depending on the signal Hamiltonian. It was shown that the kink structure is actually the one that minimizes the order by storing the disorder as very fast oscillations.

Finally, the question of the phenomenon responsible for the appearance of the PDW was posed. Haelterman et al. showed the appearance through PMI of those structures in very short fibers, that can be considered isotropic. Indeed, the PDW can be observed in the perfect case of the isotropic model, but not in the Manakov model. High power pulses were thus sent in shorter lengths of TWHD fiber, to observe the PMI and its evolution with length. While the observations in short (50 m and 200 m) fibers confirmed the apparition of PMI, the phenomenon became more complex in longer fibers (500 m and 1000 m). New behaviours however appeared in longer fibers, with potentially new sidebands and their high sensibility to input polarization. However, higher order effects such as Raman scattering become very intense and makes highly challenging the interpretation of such experimental observations. This work is still in progress. To go further into the analysis of this phenomenon, a model that includes the method of fabrication of the fiber, a very fast spinning of the preform during drawing shown to reduce the residual birefringence of the fiber[117–122], was designed. This new set of two coupled stochastic nonlinear Schrödinger equations however, does not deterministically describes the propagation of an electrical field in an optical fiber.

The observations described in this chapter give a better understanding of what happens during the propagation of light in a SPUN fiber and open the way to new applications of those fibers, such as high power pulse transmission, transmission of signal with low deformation in normal regime fibers, and clock synchronization. More importantly, these results can be considered the first experimental demonstration of symbiotic self-organization in optical fibers, as the first kink-soliton transmission in nonlinear optical fiber.

Conclusion

In this work, multiple applications of cross-phase modulation induced effects were studied through different experiments inside normal dispersion fibers. All those experiments are based on the principle that when one sends two orthogonally polarized signals in a fiber, a nonlinear interaction is created between the two. By changing the shape of those two signals, two all-optical applications were created.

First, a pulse generator was made by sending two 40 GHz sinusoidal waves with out-of-phase intensities on orthogonal polarizations with a high average power difference in a fiber. During propagation, the high power pulses were observed to broaden under the influence of SPM and chromatic dispersion, leading through XPM to the apparition of a compression effect on the pulses of the sinusoid from the second axis of polarization. It was shown that the compression was improved as the pump power increased until Brillouin scattering limited the power that could be transmitted. The resulting train at a power of 26.5 dBm was composed of 3.3 ps short pulses at a repetition rate of 40 GHz, giving a compression ratio around 4.

Observing the compression of the pulses energy through this technique, the low power sinusoidal wave was replaced by a couple of gaussian pulses with a FWHM in the nanosecond scale, or about 10 times longer than the pump pulses. Similarly to the previous experiment, the energy of the gaussian pulse was compressed into a train of pulses, which now followed the envelope of the initial signal, but with a higher peak power. The input was thus both sampled and magnified. In order to quickly predict such sampling, a theoretical model based on the assumption that the power difference is so large that the nonlinear effects coming from the low power signal can be neglected was developed, allowing by the resolution of a simple LDE system to evaluate the output signal.

Building on those observations, the idea of a soliton based on the equilibrium between dispersion and XPM emerged. While such an experiment would have been impossible previously as the PMD of the optical fibers were too high, new technology allowing for its averaging over long distance brought the idea back. Such an equilibrium only theoretically appears for isotropic fiber. During this work, the first Polarization Domain Walls were observed experimentally in a TWHD fiber. First, simple train of such solitons were transmitted in a 10 km-long fiber by

sending two signals with orthogonal polarizations and complementary intensities copropagating. After propagation and redecomposition of the two axes of polarization, the pulse trains was show to have conserved its profile, while sending only one of those two axes demonstrated a complete loss of information. Built on these observations, a XPM coefficient of 1.3 was determined by determining numerically the best fit to the experimental observations of the model developed by Haelterman[93]. In a second part, and based on the same principle, a NRZ-encoded signal, the title of the project 'PETAL', was transmitted over a 50 km normal dispersion TWHD fiber with no loss of information and no reconstruction of the signal at the output. A last study was performed showing the robustness of the PDW, by observing their spontaneous apparition. Sending two bandwidth-controlled non-correlated incoherent signals on the two axes of polarization, the experimental appearance of an anti-correlation was observed after their propagation and redecomposition at the output of the fiber. It was then shown numerically that the segregation between the two signals is higher for a lower Hamiltonian value of the signal.

Finally, the PMI phenomenon responsible for the apparition of PDW was studied. Sending a high peak power pulse in the same TWHD normal fibers but with a shorter length, we were able to see the appearance of PMI bands over 50 m and 200 m proving that on such distances, this fiber can be considered to be isotropic. At higher fiber lengths, new unexplained bands were observed to appear, but could not be explained by the simple model used previously. A new model taking into account the spinning induced on the fiber during manufacturing was developed, and its study will be done in the future.

Perspectives

Those last observations lead to the development of a new model based on the physical structure of the fibers. As a manufacturing process, and in order to reduce the previously mentioned PMD, the fiber preforms are spinned during the drawing phase. This new model takes into account such a rotation with the random natural birefringence to simulate propagation of signals in the fiber. By studying such model, one could explain both the physical origin of the PDW that are not described by the Manakov model, along with the rise of the bands that were observed in the last experiment of this study. This new model was shown to be an intermediate between Manakov and the ideal isotropic case, which fits with the model of an XPM coefficient between 1 and 2 as was determined in the experiments of this manuscript. Such a model could give new insights allowing to reduce PMD further by enabling the simulation of this spinning or offering the capability to determine numerically the best spinning parameters.

Further exploration of the PDW is currently being performed by propagation in a fibered cavity of 10 m[126], demonstrating possible application of PDW for all-optical data storage. Simultaneously, modulation instability was observed to appear in between modes of a bimodal fiber by Dupiol et al.[127], showing the first traces of the possible existence of spatial domain walls, as inter-modal MI would be an indicator, similarly to the case of the PDW, of their appearance.

Appendix A

Hamiltonian calculation

In Chapter 2, the Hamiltonian of both signals was calculated during their propagation through the fiber. As this calculation is not trivial, it is detailed in the following annex. First, the Hamiltonian will be demonstrated for the case of scalar propagation, then the model will be extended to vectorial propagation. A summary of the different equations will then be given as a quick reference.

A.1 Calculation of the Hamiltonian in the scalar regime

In the scalar regime, the NLSE can be expressed, as seen in Chapter 1 :

$$i\frac{\partial A}{\partial z} - \frac{\beta_2}{2}\frac{\partial^2 A}{\partial T^2} + \gamma \left|A\right|^2 A = 0 \tag{A.1}$$

Two new equations can be obtained from this one. The first, by multiplying it by $\partial A^*/\partial z$, the conjugate vector of the signal electrical field :

$$\frac{\partial A^*}{\partial z} i\frac{\partial A}{\partial z} = -\frac{\beta_2}{2}\frac{\partial A^*}{\partial z}\frac{\partial^2 A}{\partial T^2} + \gamma \frac{\partial A^*}{\partial z}|A|^2 A \tag{A.2}$$

Then by taking the conjugate of this equation

$$-\frac{\partial A}{\partial z} i\frac{\partial A^*}{\partial z} = -\frac{\beta_2}{2}\frac{\partial A}{\partial z}\frac{\partial^2 A^*}{\partial T^2} + \gamma \frac{\partial A}{\partial z}|A|^2 A^* \tag{A.3}$$

by adding those two equations, we then get:

$$0 = -\frac{\beta_2}{2}\left(\frac{\partial A^*}{\partial z}\frac{\partial^2 A}{\partial T^2} + \frac{\partial A}{\partial z}\frac{\partial^2 A^*}{\partial T^2}\right) + \gamma|A|^2\left(A\frac{\partial A^*}{\partial z} + A^*\frac{\partial A}{\partial z}\right) \tag{A.4}$$

This last equation is then integrated on the time axis :

$$0 = -\frac{\beta_2}{2}\int_T \left(\frac{\partial A^*}{\partial z}\frac{\partial^2 A}{\partial T^2} + \frac{\partial A}{\partial z}\frac{\partial^2 A^*}{\partial T^2}\right)\partial T + \gamma|A|^2\int_T \left(A\frac{\partial A^*}{\partial z} + A^*\frac{\partial A}{\partial z}\right)\partial T \quad \text{(A.5)}$$

To go further, the two parts of this equation will be simplified separately. They will be noted as :

$$a = \int_T \left(\frac{\partial A^*}{\partial z}\frac{\partial^2 A}{\partial T^2} + \frac{\partial A}{\partial z}\frac{\partial^2 A^*}{\partial T^2}\right)\partial T \quad \text{(A.6)}$$

$$b = \int_T \left(A\frac{\partial A^*}{\partial z} + A^*\frac{\partial A}{\partial z}\right)\partial T \quad \text{(A.7)}$$

A.1.1 Simplification of a

Let's separate the members in the first integral:

$$a = \int_T \frac{\partial A^*}{\partial z}\frac{\partial^2 A}{\partial T^2}\partial T + \int_T \frac{\partial A}{\partial z}\frac{\partial^2 A^*}{\partial T^2}\partial T \quad \text{(A.8)}$$

by integrating by parts the first of those integrals:

$$\int_T \frac{\partial A^*}{\partial z}\frac{\partial^2 A}{\partial T^2}\partial T = \left[\frac{\partial A^*}{\partial z}\frac{\partial A}{\partial T}\right]_0^T - \int_T \frac{\partial^2 A^*}{\partial T\partial z}\frac{\partial A}{\partial T}\partial T \quad \text{(A.9)}$$

By taking a periodical limit condition, the primitive term of this equation is equal to 0. The same method is then applied to the second term of a, and both expressions are injected back in Eq. (A.8), resulting in

$$a = -\int_T \left(\frac{\partial^2 A^*}{\partial T\partial z}\frac{\partial A}{\partial T} + \frac{\partial^2 A}{\partial T\partial z}\frac{\partial A^*}{\partial T}\right)\partial T \quad \text{(A.10)}$$

Then, by using the formula for the derivative of a product

$$a = -\int_T \frac{\partial}{\partial z}\left(\frac{\partial A^*}{\partial T}\frac{\partial A}{\partial T}\right)\partial T = -\int_T \frac{\partial}{\partial z}\left(\left|\frac{\partial A}{\partial T}\right|^2\right)\partial T \quad \text{(A.11)}$$

$$a = -\frac{\partial}{\partial z}\left(\int_T \left|\frac{\partial A}{\partial T}\right|^2 \partial T\right) \quad \text{(A.12)}$$

By then using the Plancherel theorem

$$\int_{-\infty}^{+\infty} |f(x)|^2\, dx = \int_{-\infty}^{+\infty} \left|\tilde{f}(\xi)\right|^2 d\xi \quad \text{(A.13)}$$

the following expression is obtained :

$$a = -\frac{\partial}{\partial z}\left(\int_{\omega}\left|\tilde{f}\left\{\frac{\partial A}{\partial T}\right\}\right|^{2}\partial\omega\right) \tag{A.14}$$

from the properties of the derivative of the Fourier transform

$$\tilde{f}\left\{\frac{\partial A}{\partial T}\right\}(\omega) = (2i\pi\omega)\tilde{A}(\omega) \tag{A.15}$$

so by replacing in the last expression of a, we get

$$a = -\frac{\partial}{\partial z}\left(\int_{\omega}\left|(2\pi i\omega)^{2}\tilde{A}\right|^{2}\partial\omega\right) \tag{A.16}$$

ending in

$$a = (2\pi\omega)^{2}\frac{\partial}{\partial z}\left(\int_{\omega}\left|\tilde{A}\right|^{2}\partial\omega\right) \tag{A.17}$$

A.1.2 Simplification of b

Let us remember the expression of b

$$b = \int_{T}|A|^{2}\left(A\frac{\partial A^{*}}{\partial z} + A^{*}\frac{\partial A}{\partial z}\right)\partial T \tag{A.18}$$

Using the properties of the product of the derivation :

$$b = \int_{T}\frac{\partial\left|A\right|^{2}}{\partial z}\left|A\right|^{2}\partial T \tag{A.19}$$

Then using properties of the derivative of the square of a function :

$$b = \partial_{z}\left(\frac{1}{2}\int_{T}|A|^{4}\partial T\right) \tag{A.20}$$

A.1.3 Final equation

By replacing a and b in A.8

$$0 = \frac{\partial}{\partial z}\left(\frac{\beta_{2}}{2}\int_{\omega}(2\pi\omega)^{2}\left|\tilde{A}\right|^{2}\partial\omega + \frac{\gamma}{2}\int_{T}\left|A\right|^{4}\partial T\right) \tag{A.21}$$

By then writing the Hamiltonian as :

$$H = E_{A} + H_{A} \tag{A.22}$$

with

$$E_A = \frac{\beta_2}{2} \int_\omega (2\pi\omega)^2 \left|\tilde{A}\right|^2 \partial\omega \tag{A.23}$$

$$H_A = \frac{\gamma}{2} \int_T |A|^4 \partial T \tag{A.24}$$

we obtain that the Hamiltonian of the signal must stay constant during propagation through the fiber. As a side effect, the expressions of E_A and H_A are now very easy to numerically compute.

A.1.4 Extension to the vectorial case

By now using the coupled NLSE equations Eq. (1.19), a new term will be added to the equation similar to A.8 for each of the nlse equation. After adding up everything, and simplifying, using the previous notations

$$\begin{aligned} 0 = \frac{\partial}{\partial z}\left(H_{A_+} + H_{A_-} + E_{A_+} + E_{A_-}\right) + \\ \frac{\partial}{\partial z}\left(\gamma C_{XPM} \int_T \left[|A_-|^2 \frac{\partial}{\partial z}(|A_+|^2) + |A_+|^2 \frac{\partial}{\partial z}(|A_-|^2)\right] \partial T\right) \end{aligned} \tag{A.25}$$

Using again the properties of the derivative of a product

$$0 = \frac{\partial}{\partial z}\left(H_{A_+} + H_{A_-} + E_{A_+} + E_{A_-} + \left(\gamma C_{XPM} \int_T |A_+|^2 |A_-|^2 \partial T\right)\right) \tag{A.26}$$

then, by introducing the notation

$$H_x = \gamma C_{XPM} \int_T |A_+|^2 |A_-|^2 \partial T \tag{A.27}$$

And reinjecting in Eq. (A.25) :

$$0 = \frac{\partial H}{\partial z} = \frac{\partial}{\partial z}\left(H_{A_+} + H_{A_-} + E_{A_+} + E_{A_-} + H_x\right) \tag{A.28}$$

thus giving

$$H = H_{A_+} + H_{A_-} + E_{A_+} + E_{A_-} + H_x \tag{A.29}$$

Having this result proves that the total Hamiltonian is indeed also constant during propagation in the vectorial case. Similarly, the equations show that the calculation of those terms numerically is quite easy.

A.2 Hamiltonian expression summary

When using the following propagation equations

$$\frac{\partial A_+}{\partial z} + \frac{i\beta_2}{2}\frac{\partial^2 A_+}{\partial T^2} = \frac{2i\gamma}{3}\left(c_{SPM}\left|A_+\right|^2 + c_{XPM}\left|A_-\right|^2\right)A_+ \tag{A.30}$$

$$\frac{\partial A_-}{\partial z} + \frac{i\beta_2}{2}\frac{\partial^2 A_-}{\partial T^2} = \frac{2i\gamma}{3}\left(c_{SPM}\left|A_-\right|^2 + c_{XPM}\left|A_+\right|^2\right)A_- \tag{A.31}$$

The Hamiltonian and its different components can be calculated using

$$h = h_u + h_v + h_x + e_u + e_v H = H_{A_+} + H_{A_-} + H_x + E_{A_+} + E_{A_-} \tag{A.32}$$

$$H_{A_+} = \frac{\gamma}{2}\int_T \left|A_+\right|^4 \partial T \tag{A.33}$$

$$H_{A_-} = \frac{\gamma}{2}\int_T \left|A_-\right|^4 \partial T \tag{A.34}$$

$$H_x = \frac{\gamma}{2} C_{XPM}\int_T \left|A_+\right|^2 \left|A_-\right|^2 \partial T \tag{A.35}$$

$$E_{A_+} = \frac{\beta_2}{2}\int_\omega (2\pi\omega)^2 \left|\tilde{A_+}\right|^2 \partial\omega \tag{A.36}$$

$$E_{A_-} = \frac{\beta_2}{2}\int_\omega (2\pi\omega)^2 \left|\tilde{A_-}\right|^2 \partial\omega \tag{A.37}$$

With the terms corresponding to:

H Total Hamiltonian

H_{A_+} Hamiltonian of A_+

H_{A_-} Hamiltonian of A_-

H_x Interaction Hamiltonian

E_{A_+} Kinetic energy of A_+

E_{A_-} Kinetic energy of A_-

Journal publications

- Marin Gilles, Pierre-Yves Bony, Jocelin Garnier, Antonio Picozzi, Massimiliano Guasoni, and Julien Fatome. Topological Bits for Data Transmission. Nature Photonics, 11(January):102–107, 2017
- Javier Nuño, Marin Gilles, Massimiliano Guasoni, Bertrand Kibler, Christophe Finot, and Julien Fatome. 40 GHz pulse source based on cross-phase modulation-induced focusing in normally dispersive optical fibers. Optics letters, 41(6):1110–1113, 2016
- Javier Nuño, Marin Gilles, Massimiliano Guasoni, Christophe Finot, and Julien Fatome. All-optical sampling and magnification based on XPM-induced focusing. Optics Express, 24(22):986–988, 2016
- J. Nuño, M. Gilles, M. Guasoni, C. Finot, and J. Fatome. All-optical sampling and magnification based on XPM-induced focusing. Optics Express, 24(22), 2016

Conferences

- M. Gilles, P.-Y. Bony, J. Garnier, A. Picozzi, M. Guasoni, and J. Fatome. Universal polarization domain walls in optical fibers as topological bit-entities for data transmission. In Optics InfoBase Conference Papers, 2016
- J. Nuno, M. Gilles, M. Guasoni, B. Kibler, C. Finot, and J. Fatome. 40-Ghz pulse source based on XPM-induced focusing in normally dispersive optical fibers. In 2016 Conference on Lasers and Electro-Optics, CLEO 2016, 2016
- J. Nuño, M. Gilles, M. Guasoni, C. Finot, and J. Fatome. Sampling and magnification technique based on XPM-induced focusing in normally dispersive optical fibers. In Optics InfoBase Conference Papers, 2016
- J. Nuno, M. Gilles, M. Guasoni, and J. Fatome. Amplification technique based on XPM-induced focusing in normally dispersive optical fibers. In 2016 Conference on Lasers and Electro-Optics, CLEO 2016, 2016

Glossary

ASC . . . . . Adiabatic Soliton Compression

ASE . . . . . Amplified Spontaneous Emission

AWG . . . . . Arbitrary Waveform Generator

CNSLE . . . . . Coupled Nonlinear Shrödinger Equations

CPDF . . . . . Comb-like Profiled Dispersion Fiber

CPF . . . . . Comb Profile Fibers

CW . . . . . continuous wave

CW Laser . . . . . Continuous Wave Laser

DDF . . . . . Dispersion Decreasing Fibers

DF-DDF . . . . . Dispersion-flattened DDF

DSF . . . . . Dispersion Shifted Fiber

DW . . . . . Domain Wall

EDFA . . . . . Erbium-doped Fiber Amplifier

ESO . . . . . Electrical Sampling Oscilloscope

FROG . . . . . Frequency-Resolved Optical Gating

FT . . . . . Fourier transform

FT Limit . . . . . Fourier Transform Limit

FWHM . . . . . Full-Width Half Maximum

FWM . . . . . Four-Wave Mixing

GVD . . . . . Group Velocity Dispersion

HNLF . . . . . Highly NonLinear Fiber

IM . . . . . Intensity Modulator

LDE . . . . . Linear Differential Equations

MI . . . . . Modulation Instability

MZM . . . . . Mach-Zender Modulator

NLSE . . . . . Nonlinear Shrödinger Equation

NRZ . . . . . Non-Return to Zero

OSA . . . . . Optical Spectrum Analyser

OSO . . . . . Optical Sampling Oscilloscope

OTDM . . . . . Optical Time-Division Multiplexing

PBS . . . . . Polarization Beam Splitter

PC . . . . . Polarization Controller

PDW . . . . . Polarization Domain Walls

PM . . . . . Phase Modulator

PMD . . . . . Polarization Mode Dispersion

PMI . . . . . Polarization Modulation Instability

PPG . . . . . Pulse Pattern Generator

PWS . . . . . Polarization WaveShaper

RF . . . . . Radiofrequency

SBS . . . . . Stimulated Brillouin Back-scattering

SFG . . . . . Sum Frequency Generation

SMF . . . . . Single Mode Fiber

SOA . . . . . Semiconductor Optical Amplifier

SOP . . . . . State of Polarization

SPDF . . . . . Step-like Profiled Dispersion Fiber

SPM . . . . . Self-Phase Modulation

TWHD . . . . . TrueWave High-Dispersion fiber

WDM . . . . . Wavelength-Division Multiplexing

XPM . . . . . Cross-Phase Modulation

Bibliography

[1] Massimiliano Guasoni, Pierre-Yves Bony, Marin Gilles, Antonio Picozzi, and Julien Fatome. Fast and Chaotic Fiber-Based Nonlinear Polarization Scrambler. IEEE Journal on Selected Topics in Quantum Electronics, 22(2):1–12, 2016.

[2] Govind P. Agrawal. Nonlinear Fiber Optics (5th Ed.). Academic, Oxford, 2013.

[3] Clifford S. Gardner, John M. Greene, Martin D. Kruskal, and Robert M. Miura. Method for solving the Korteweg-deVries equation. Physical Review Letters, 19(19):1095–1097, 1967.

[4] M A Ablowitz and P A Clarkson. Solitons, nonlinear evolution equations and inverse scattering. 1991.

[5] Akira Hasegawa and Yuji Kodama. Solitons in optical communications. Number 7. Oxford University Press, USA, 1995.

[6] J. R. Taylor. Optical Solitons: Theory and Experiment. Cambridge University Press, 1992.

[7] L A Ostrovskii. Propagation of wave packets and space-time self-focusing in a nonlinear medium. Sov. Phys. JETP, 24(4):797–800, 1967.

[8] L A Ostrovskii. Envelope Shock Waves. Sov. Phys. JETP, 27(4):660–663, 1968.

[9] Rogers H. Stolen. Phase-Matched-Stimulated Four-Photon Mixing in Silica-Fiber Waveguides. IEEE Journal of Quantum Electronics, 11(3):100–103, 1975.

[10] Jonas Hansryd, Peter A. Andrekson, Mathias Westlund, Jie Li, and Per Olof Hedekvist. Fiber-based optical parametric amplifiers and their applications. IEEE Journal on Selected Topics in Quantum Electronics, 8(3):506–520, 2002.

[11] S. V. Manakov. On the theory of two-dimensional stationary self-focusing of electromagnetic waves. Soviet Physics JETP, 38(2):248–253, 1974.

[12] A. L. Berkhoer and V. E. Zakharov. Self Excitation of Waves With Different Polarizations in Nonlinear Media. Soviet Journal of Experimental and Theoretical Physics, 31(3):486–490, 1970.

[13] Robert A. Fisher and William K. Bischel. Numerical studies of the interplay between self-phase modulation and dispersion for intense plane-wave laser pulses. Journal of Applied Physics, 46(11):4921–4934, 1975.

[14] J. A. Armstrong. Measurement of picosecond laser pulse widths. Applied Physics Letters, 10(1):16–18, 1967.

[15] D J Kane and R Trebino. Characterization of Arbitrary Femtosecond Pulses Using Frequency-Resolved Optical Gating. Ieee Journal of Quantum Electronics, 29(2):571–579, 1993.

[16] Ferenc Krausz, M.E. Fermann, Thomas Brabec, P.F. Curley, Martin Hofer, M.H. Ober, Christian Spielmann, Ernst Wintner, and A.J. Schmidt. Femtosecond solid-state lasers. IEEE Journal of Quantum Electronics, 28(10):2097–2122, 1992.

[17] Christian Spielmann, Peter F. Curley, Thomas Brabec, and Ferenc Krausz. Ultrabroadband Femtosecond Lasers. IEEE Journal of Quantum Electronics, 30(4):1100–1114, 1994.

[18] Takashi Inoue and Shu Namiki. Pulse compression techniques using highly nonlinear fibers. Laser & Photonics Review, 2(1-2):83–99, 2008.

[19] S. V. Chernikov, E. M. Dianov, D. J. Richardson, R. I. Laming, and D. N. Payne. 114 Gbit/s soliton train generation through Raman self-scattering of a dual frequency beat signal in dispersion decreasing optical fiber. Applied Physics Letters, 63(3):293–295, 1993.

[20] Yasuyuki Ozeki, Shigehiro Takasaka, Takashi Inoue, Koji Igarashi, Jiro Hiroishi, Ryuichi Sugizaki, Misao Sakano, and Shu Namiki. Nearly exact optical beat-to-soliton train conversion based on comb-like profiled fiber emulating a polynomial dispersion decreasing profile. IEEE Photonics Technology Letters, 17(8):1698–1700, 2005.

[21] J. R. Taylor, R. Kashyap, and S.V. V. Chernikov. Experimental demonstration of step-like dispersion profiling in optical fibre for soliton pulse generation and compression. Electronics Letters, 30(5):433–435, mar 1994.

[22] Akira Hasegawa. Generation of a train of soliton pulses by induced modulational instability in optical fibers. Optics letters, 9(7):288–90, 1984.

[23] Julien Fatome, Ibrahim El-Mansouri, Jean-Luc Blanchet, Stéphane Pitois, Guy Millot, Stefano Trillo, and Stefan Wabnitz. Even harmonic pulse train generation by cross-polarization-modulation seeded instability in optical fibers. Journal of the Optical Society of America B, 30(1):99–106, 2013.

[24] Stefano Trillo, Stefan Wabnitz, and T. A B Kennedy. Nonlinear dynamics of dual-frequency-pumped multiwave mixing in optical fibers. Physical Review A, 50(2):1732–1747, 1994.

[25] Eric A. Swanson and Stephen R. Chinn. 40-GHz Pulse Train Generation Using Soliton Compression of a Mach-Zehnder Modulator Output. IEEE Photonics Technology Letters, 7(1):114–116, 1995.

[26] Julien Fatome, Stéphane Pitois, Coraline Fortier, Kibler Bertrand, Christophe Finot, Guy Millot, C. Courde, M. Lintz, and E. Samain. Multiple four-wave mixing in optical fibers: 1.5-3.4-THz femtosecond pulse sources and real-time monitoring of a 20-GHz picosecond source. Optics Communications, 283(11):2425–2429, 2010.

[27] K E Webb, M Erkintalo, Y Q Xu, G Genty, and S G Murdoch. Efficiency of dispersive wave generation from a dual-frequency beat signal. Optics Letters, 39(20):5850–5853, 2014.

[28] Christophe Finot, Julien Fatome, Stéphane Pitois, and Guy Millot. All-fibered high-quality low duty-cycle 20-GHz and 40-GHz picosecond pulse sources. IEEE Photonics Technology Letters, 19(21):1711–1713, 2007.

[29] Coraline Fortier, Kibler Bertrand, Julien Fatome, Christophe Finot, Stéphane Pitois, and Guy Millot. All-fibered high-quality low duty-cycle 160-GHz femtosecond pulse source. Laser Physics Letters, 5(11):817–820, 2008.

[30] J. J. Pigeon, S. Ya. Tochitsky, and C. Joshi. High-power, mid-infrared, picosecond pulses generated by compression of a CO_2 laser beat-wave in GaAs. Optics Letters, 40(24):5730, dec 2015.

[31] Andreas O J Wiberg, Camille Sophie Brès, Bill P P Kuo, John X. Zhao, Nikola Alic, and Stojan Radic. Pedestal-free pulse source for high data rate optical time-division multiplexing based on fiber-optical parametric processes. IEEE Journal of Quantum Electronics, 45(11):1325–1330, 2009.

[32] Pavel V. Mamyshev, Stanislav V. Chernikov, and E. M. Dianov. Generation of Fundamental Soliton Trains for High-Bit-Rate Optical Fiber Communication Lines. IEEE Journal of Quantum Electronics, 27(10):2347–2355, 1991.

[33] W. Tomlinson, R. H. Stolen, and C. Shank. Compression of optical pulses chirped by self-phase modulation in fibers, 1984.

[34] E. B. Treacy. Optical Pulse Compression With Diffraction Gratings. IEEE Journal of Quantum Electronics, 5(9):454–458, 1969.

[35] L. F. Mollenauer, R. H. Stolen, and J. P. Gordon. Experimental observation of picosecond pulse narrowing and solitons in optical fibers. Physical Review Letters, 45(13):1095–1098, 1980.

[36] Yasuhiro Matsui, Mark D. Pelusi, and Akira Suzuki. Generation of 20-fs optical pulses from a gain-switched laser diode by a four-stage soliton compression technique. IEEE Photonics Technology Letters, 11(10):1217–1219, 1999.

[37] H. Kubota, M. Nakazawa, Y. Kimura, and E. Yoshida. Generation of a 170 fs, 10 GHz transform-limited pulse train at 1.55 µm using a dispersion-decreasing, erbium-doped active soliton compressor. Electronics Letters, 30(24):2038–2040, nov 1994.

[38] K. R. Tamura and M. Nakazawa. Femtosecond Soliton Generation over a 32-nm Wavelength Range Using a Dispersion-Flattened Dispersion-Decreasing Fiber. IEEE Photonics Technology Letters, 11(3):319–321, 1999.

[39] K. Mori, H. Takara, S. Kawanishi, M. Saruwatari, and T. Morioka. Flatly broadened supercontinuum spectrum generated in a dispersion decreasing fibre with convex dispersion profile. Electronics Letters, 33(21):1806, 1997.

[40] K R Tamura and M Nakazawa. 54-fs, 10-GHz soliton generation from a polarization-maintaining dispersion-flattened dispersion-decreasing fiber pulse compressor. Optics letters, 26(11):762–4, 2001.

[41] M L V Tse, P Horak, J H V Price, F Poletti, F He, and D J Richardson. Pulse compression at 1.06 microm in dispersion-decreasing holey fibers. Optics letters, 31(23):3504–3506, 2006.

[42] Frédéric Druon, Nicolas Sanner, Gaëlle Lucas-Leclin, Patrick Georges, Kim P Hansen, and Anders Petersson. Self-compression and Raman soliton generation in a photonic crystal fiber of 100-fs pulses produced by a diode-pumped Yb-doped oscillator. Applied optics, 42(33):6768–6770, 2003.

[43] R. H. Stolen and E. P. Ippen. Raman gain in glass optical waveguides. Applied Physics Letters, 22(6):276–278, 1973.

[44] Masahiro Ikeda. Stimulated Raman amplification characteristics in long span single-mode silica fibers. Optics Communications, 39(3):148–152, oct 1981.

[45] F. Feng, J. Fatome, A. Sysoliatin, Y.K. Chembo, S. Wabnitz, and C. Finot. Wavelength conversion and temporal compression of pulse train using dispersion oscillating fibre. Electronics Letters, 50(10):768–770, 2014.

[46] Stéphane Pitois, Julien Fatome, and Guy Millot. Generation of a 160-GHz transform-limited pedestal-free pulse train through multiwave mixing compression of a dual-frequency beat signal. Optics letters, 27(19):1729–31, 2002.

[47] Q. Z. Wang, P. P. Ho, and R. R. Alfano. Degenerate cross-phase modulation for pulse compression and amplification of ultrashort laser pulses. Optics letters, 15(18):1023–5, 1990.

[48] R. Jin, M. Liang, G. Khitrova, H. M. Gibbs, and N. Peyghambarian. Compression of bright optical pulses by dark solitons. Optics letters, 18(7):494–6, 1993.

[49] Qi Guo and Xiujuan Jiang. Induced focusing from co-propagation of a pair of bright-dark optical beams in self-defocusing Kerr media. Optics Communications, 254(1-3):19–29, 2005.

[50] Andrew J. Stentz, Martti Kauranen, Jeffery J Maki, Govind P. Agrawal, and Robert W. Boyd. Induced focusing and spatial wave breaking from cross-phase modulation in a self-defocusing medium. Optics Letters, 17(1):19, jan 1992.

[51] Govind P. Agrawal, P. L. Baldeck, and R. R. Alfano. Optical wave breaking and pulse compression due to cross-phase modulation in optical fibers. Optics letters, 14(2):137–139, 1989.

[52] Julien Fatome, Christophe Finot, Guy Millot, A. Armaroli, and Stefano Trillo. Observation of optical undular bores in multiple four-wave mixing. Physical Review X, 4(2):021022, 2014.

[53] P. K. A. Wai and C. R. Menyak. Polarization mode dispersion, decorrelation, and diffusion in optical fibers with randomly varying birefringence. Journal of Lightwave Technology, 14(2):148–157, 1996.

[54] P.V. Mamyshev. All-optical data regeneration based on self-phase modulation effect. In 24th European Conference on Optical Communication. ECOC '98 (IEEE Cat. No.98TH8398), volume 1, pages 475–476. Telefonica, 1998.

[55] M. D. Pelusi, A. Sysoliatin, and A. Suzuki. Highly nonlinear optical fibre loop mirror for reshaping femtosecond pulses from a soliton-compressed electro-absorption modulator source over a wide repetition rate and wavelength range. Optical and Quantum Electronics, 33(7/10):775–784, 2001.

[56] L. A. Provost, C. Finot, P. Petropoulos, K. Mukasa, and D. J. Richardson. Design scaling rules for 2R-optical self-phase modulation-based regenerators. Optics Express, 15(8):5100–5113, 2007.

[57] M. A. Duguay and J. W. Hansen. An ultrafast light gate. Applied Physics Letters, 15(6):192–194, 1969.

[58] Tetsuya Kanada and Douglas L. Franzen. Optical waveform measurement by optical sampling with a mode-locked laser diode. Optics Letters, 11(1):4, 1986.

[59] Hiroshi Ohta, Seiji Nogiwa, N. Oda, and H. Chiba. Highly sensitive optical sampling system using timing-jitter-reduced gain-switched optical pulse. Electron. Lett., 33(25):2142–2144, 1997.

[60] I. Shake, E. Otani, H. Takara, K. Uchiyama, Y. Yamabayashi, and Toshio Morioka. Bit rate flexible quality monitoring of 10 to 16OGbit/s optical signals based on optical sampling technique. Transactions of the Korean Institute of Electrical Engineers, 36(25):2087–2088, 2000.

[61] R. L. Jungerman, G. Lee, O. Buccafusca, Y. Kaneko, N. Itagaki, R. Shioda, A. Harada, Y. Nihei, and G. Sucha. 1-THz bandwidth C- and L-band optical sampling with a bit rate agile timebase. IEEE Photonics Technology Letters, 14(8):1148–1150, 2002.

[62] Toshiaki Suhara, Hideki Ishizuki, Masatoshi Fujimura, and Hiroshi Nishihara. Waveguide quasi-phase-matched sum-frequency generation device for high-efficiency optical sampling. IEEE Photonics Technology Letters, 11(8):1027–1029, aug 1999.

[63] S. Nogiwa, Y. Kawaguchi, H. Ohta, and Y. Endo. Highly sensitive and time-resolving optical sampling system using thin PPLN crystal. Electronics Letters, 36(20):1727, 2000.

[64] Nobuhide Yamada, Seiji Nogiwa, and Hiroshi Ohta. 640-Gb/s OTDM signal measurement with high-resolution optical sampling system using wavelength-tunable soliton pulses. IEEE Photonics Technology Letters, 16(4):1125–1127, 2004.

[65] Jie Li, Jonas Hansryd, Per Olof Hedekvist, Peter A. Andrekson, and Stig N. Knudsen. 300-Gb/s eye-diagram measurement by optical sampling using fiber-based parametric amplification. IEEE Photonics Technology Letters, 13(9):987–989, 2001.

[66] S.-I. Oda, Akihiro Maruta, and K.-I. Kitayama. All-Optical Quantization Scheme Based on Fiber Nonlinearity. IEEE Photonics Technology Letters, 16(2):587–589, feb 2004.

[67] Jie Li, Mathias Westlund, Henrik Sunnerud, Bengt Erik Olsson, Magnus Karlsson, and Peter A. Andrekson. 0.5-Tb/s Eye-Diagram Measurement by Optical Sampling Using XPM-Induced Wavelength Shifting in Highly Nonlinear Fiber. IEEE Photonics Technology Letters, 16(2):566–568, 2004.

[68] P A Andrekson and M Westlund. Nonlinear optical fiber based high resolution all-optical waveform sampling. Laser & Photonics Review, 1(3):231–248, 2007.

[69] Shangjian Zhang, Yong Liu, Yongzhi Liu, and Harm J.S. Dorren. All-optical sampling exploiting nonlinear polarization rotation in a single semiconductor optical amplifier. Optics Communications, 285(6):1001–1004, 2012.

[70] Chris Xu and Xiang Liu. Photonic analog-to-digital converter using soliton self-frequency shift and interleaving spectral filters. Optics letters, 28(12):986–988, 2003.

[71] Reza Maram, James Van Howe, Ming Li, and José Azaña. Noiseless intensity amplification of repetitive signals by coherent addition using the temporal Talbot effect. Nature Communications, 5:5163, 2014.

[72] Carsten Schmidt-Langhorst and Hans Georg Weber. Optical sampling techniques. Journal of Optical and Fiber Communications Reports, 2(1):86–114, 2005.

[73] Robert W. Boyd. Nonlinear optics. Elsevier, 2008.

[74] Pierre Walczak, Stéphane Randoux, and Pierre Suret. Optical Rogue Waves in Integrable Turbulence. Physical Review Letters, 114(14):143903, apr 2015.

[75] Ghung En Zah and Tien Pei Lee. Observation of Highly Nondegenerate Four-Wave Mixing in 1. 5 ??m, Traveling-Wave Semiconductor Optical Amplifiers and Estimation of Nonlinear Gain Coefficient. IEEE Journal of Quantum Electronics, 28(1):151–156, 1992.

[76] P.A. Andrekson. Picosecond optical sampling using four-wave mixing in fibre. Electronics Letters, 27(16):1440–1441, 1991.

[77] Javier Nuño, Marin Gilles, Massimiliano Guasoni, Bertrand Kibler, Christophe Finot, and Julien Fatome. 40 GHz pulse source based on cross-phase modulation-induced focusing in normally dispersive optical fibers. Optics letters, 41(6):1110–1113, 2016.

[78] Javier Nuño, Marin Gilles, Massimiliano Guasoni, Christophe Finot, and Julien Fatome. All-optical sampling and magnification based on XPM-induced focusing. Optics Express, 24(22):986–988, 2016.

[79] Pierre Weiss. L'hypothèse du champ moléculaire et la propriété ferromagnétique. Journal de Physique Théorique et Appliquée, 6(1):661–690, 1907.

[80] Linda E. Reichl. A Modern Course in Statistical Physics. Wiley-VCH, 2016.

[81] Thierry Dauxois and Michel Peyrard. Physics of solitons. Cambridge University Press,, 2010.

[82] Dan M. Stamper-Kurn and Masahito Ueda. Spinor Bose gases: Symmetries, magnetism, and quantum dynamics. Reviews of Modern Physics, 85(3):1191–1244, 2013.

[83] Steven Weinberg. The Quantum Theory of Fields. Cambridge University Press, Cambridge, 1996.

[84] D. Y. Parpia, B. K. Tanner, and D. G. Lord. Direct optical observation of ferromagnetic domains. Nature, 303(5919):684–685, jun 1983.

[85] S. E. Trullinger and V. E. Zakharov. Solitons. Elsevier Science Ltd, 1986.

[86] J. Unguris, R. J. Celotta, and D. T. Pierce. Observation of two different oscillation periods in the exchange coupling of Fe/Cr/Fe(100). Physical Review Letters, 67(1):140–143, jul 1991.

[87] D. A. Allwood. Magnetic Domain-Wall Logic. Science, 309(5741):1688–1692, sep 2005.

[88] S. S. P. Parkin, M. Hayashi, and L. Thomas. Magnetic Domain-Wall Racetrack Memory. Science, 320(5873):190–194, apr 2008.

[89] J. A. Currivan-Incorvia, S. Siddiqui, S. Dutta, E. R. Evarts, J. Zhang, D. Bono, C. A. Ross, and M. A. Baldo. Logic circuit prototypes for three-terminal magnetic tunnel junctions with mobile domain walls. Nature Communications, 7:10275, jan 2016.

[90] J.-P. Tetienne, T. Hingant, L.J. Martínez, S. Rohart, A. Thiaville, L. Herrera Diez, K Garcia, J.-P. Adam, J.-V. Kim, J.-F. Roch, I.M. Miron, G. Gaudin, L. Vila, B. Ocker, D. Ravelosona, and V. Jacques. The nature of domain walls in ultrathin ferromagnets revealed by scanning nanomagnetometry. Nature Communications, 6:6733, apr 2015.

[91] Marc Haelterman and A. P. Sheppard. Bifurcations of the dark soliton and polarization domain walls in nonlinear dispersive media. Physical Review E, 49(5):4512–4518, may 1994.

[92] Marc Haelterman and A. P. Sheppard. Polarization domain walls in diffractive or dispersive Kerr media. Optics letters, 19(2):96, jan 1994.

[93] Marc Haelterman and A. P. Sheppard. Vector soliton associated with polarization modulational instability in the normal-dispersion regime. Physical Review E, 49(4):3389–3399, apr 1994.

[94] Boris A. Malomed. Optical domain walls. Physical Review E, 50(2):1565–1571, aug 1994.

[95] A. P. Sheppard and Marc Haelterman. Polarization-domain solitary waves of circular symmetry in Kerr media. Optics letters, 19(12):859–861, 1994.

[96] Marc Haelterman. Colour domain wall solitary waves for nonreturn-to-zero optical transmission scheme. Electronics Letters, 31(9):741, 1995.

[97] Stefan Wabnitz. Cross-polarization modulation domain wall solitons for WDM signals in birefringent optical fibers. IEEE Photonics Technology Letters, 21(13):875–877, 2009.

[98] J. P. Gordon and H. A. Haus. Random walk of coherently amplified solitons in optical fiber transmission. Optics Letters, 11(10):665–667, 1986.

[99] P. Kockaert, Marc Haelterman, Stéphane Pitois, and Guy Millot. Isotropic polarization modulational instability and domain walls in spun fibers. Applied Physics Letters, 75(19):2873, nov 1999.

[100] F. Gutty, Stéphane Pitois, Philippe Grelu, Guy Millot, M. D. Thomson, and John M. Dudley. Generation and characterization of 0.6-THz polarization domain-wall trains in an ultralow-birefringence spun fiber. Optics letters, 24(20):1389–1391, oct 1999.

[101] Quinton L Williams and Rajarshi Roy. Fast polarization dynamics of an erbium-doped fiber ring laser. Optics Letters, 21(18):1478–1480, 1996.

[102] Q. L. Williams, J. García-Ojalvo, and R. Roy. Fast intracavity polarization dynamics of an erbium-doped fiber ring laser: Inclusion of stochastic effects. Physical Review A, 55(3):2376–2386, 1997.

[103] H. Zhang, D. Y. Tang, L. M. Zhao, and X. Wu. Observation of polarization domain wall solitons in weakly birefringent cavity fiber lasers. Physical Review B, 80(August):052302, 2009.

[104] Caroline Lecaplain, Philippe Grelu, and Stefan Wabnitz. Polarization-domain-wall complexes in fiber lasers. Journal of the Optical Society of America B, 30(1):211, 2012.

[105] M. Marconi, J. Javaloyes, S. Barland, S. Balle, and M. Giudici. Vectorial dissipative solitons in vertical-cavity surface-emitting Lasers with delays. Nature Photonics, 9(6):450–455, 2015.

[106] Jae K Jang, Miro Erkintalo, Stephane Coen, and Stuart G Murdoch. Temporal tweezing of light through the trapping and manipulation of temporal cavity solitons. Nat Commun, 6:1–7, 2015.

[107] Veronika Tsatourian, Sergey V Sergeyev, Chengbo Mou, Alex Rozhin, Vitaly Mikhailov, Bryan Rabin, Paul S Westbrook, and Sergei K Turitsyn. Polarisation dynamics of vector soliton molecules in mode locked fibre laser. Scientific reports, 3(12):3154, 2013.

[108] Demetrios N. Christodoulides and R. I. Joseph. Vector solitons in birefringent nonlinear dispersive media. Optics letters, 13(1):53–55, jan 1988.

[109] M. V. Tratnik and J. E. Sipe. Bound solitary waves in a birefringent optical fiber. Physical Review A, 38(4):2011–2017, aug 1988.

[110] D. N. Christodoulides. Black and white vector solitons in weakly birefringent optical fibers. Physics Letters A, 132(8-9):451–452, 1988.

[111] M Haelterman, a P Sheppard, and a W Snyder. Bound-vector solitary waves in isotropic nonlinear dispersive media. Optics letters, 18(17):1406–1408, 1993.

[112] M. Haelterman and A.P. Sheppard. Cancelling soliton interaction in single-mode optical fibres. Electronics Letters, 29(13):1176, 1993.

[113] Stéphane Pitois, Guy Millot, Philippe Grelu, and Marc Haelterman. Generation of optical domain-wall structures from modulational instability in a bimodal fiber. Physical review. E, Statistical physics, plasmas, fluids, and related interdisciplinary topics, 60(1):994–1000, 1999.

[114] David Freedman, Robert Pisani, and Roger Purves. Statistics, Fourth edition. W. W. Norton & Company, 2007.

[115] Stéphane Pitois, Guy Millot, and Stefan Wabnitz. Polarization Domain Wall Solitons with Counterpropagating Laser Beams. CLEO/Europe Conference on Lasers and Electro-Optics, pages 1409–1412, 1998.

[116] A. Picozzi, J. Garnier, T. Hansson, P. Suret, S. Randoux, G. Millot, and D. N. Christodoulides. Optical wave turbulence: Towards a unified nonequilibrium thermodynamic formulation of statistical nonlinear optics. Physics Reports, 542(1):1–132, 2014.

[117] a J Barlow, J J Ramskov-Hansen, and D N Payne. Birefringence and polarization mode-dispersion in spun single-mode fibers. Applied optics, 20(17):2962–2968, 1981.

[118] M J Li and D a Nolan. Fiber spin-profile designs for producing fibers with low polarization mode dispersion. Optics letters, 23(21):1659–1661, 1998.

[119] Luca Palmieri. Polarization properties of spun single-mode fibers. Journal of Lightwave Technology, 24(11):4075–4088, 2006.

[120] Andrea Galtarossa, Luca Palmieri, and Davide Sarchi. Measure of spin period in randomly birefringent low-PMD fibers. IEEE Photonics Technology Letters, 16(4):1131–1133, 2004.

[121] Daniel A. Nolan, Xin Chen, and Ming Jun Li. Fibers with low polarization-mode dispersion. Journal of Lightwave Technology, 22(4):1066–1077, 2004.

[122] Luca Palmieri, Tommy Geisler, and Andrea Galtarossa. Effects of spin process on birefringence strength of single-mode fibers. Optics Express, 20(1):1, 2012.

[123] Jaroslav Kurzweil and Ji? Jarn k. Limit processes in ordinary differential equations. ZAMP Zeitschrift f r angewandte Mathematik und Physik, 38(2):241–256, mar 1987.

[124] Jean-Pierre Fouque, Josselin Garnier, George Papanicolaou, and Knut Sølna. Wave Propagation and Time Reversal in Randomly Layered Media, volume 56 of Stochastic Modelling and Applied Probability. Springer New York, New York, NY, 2007.

[125] Dietrich Marcuse, C. R. Menyuk, and P. K. A. Wai. Application of the Manakov-PMD equation to studies of signal propagation in optical fibers with randomly varying birefringence. Journal of Lightwave Technology, 15(9):1735–1745, 1997.

[126] Julien Fatome, Yadong Wang, Bruno Garbin, Bertrand Kibler, Abdelkrim Bendahmane, Nicolas Berti, Gian-Luca Oppo, François Leo, Stuart Murdoch, Miro Erkintalo, and Stephane Coen. Flip-Flop Polarization Domain Walls in a Kerr Resonator. In Advanced Photonics 2018 (BGPP, IPR, NP, NOMA, Sensors, Networks, SPPCom, SOF), page JTu6F.2, Washington, D.C., 2018. OSA.

[127] R. Dupiol, A. Bendahmane, K. Krupa, J. Fatome, A. Tonello, M. Fabert, V. Couderc, S. Wabnitz, and G. Millot. Intermodal modulational instability in graded-index multimode optical fibers. Optics Letters, 42(17):3419, 2017.

[128] Marin Gilles, Pierre-Yves Bony, Jocelin Garnier, Antonio Picozzi, Massimiliano Guasoni, and Julien Fatome. Topological Bits for Data Transmission. Nature Photonics, 11(January):102–107, 2017.

[129] J. Nuño, M. Gilles, M. Guasoni, C. Finot, and J. Fatome. All-optical sampling and magnification based on XPM-induced focusing. Optics Express, 24(22), 2016.

[130] M. Gilles, P.-Y. Bony, J. Garnier, A. Picozzi, M. Guasoni, and J. Fatome. Universal polarization domain walls in optical fibers as topological bit-entities for data transmission. In Optics InfoBase Conference Papers, 2016.

[131] J. Nuno, M. Gilles, M. Guasoni, B. Kibler, C. Finot, and J. Fatome. 40-Ghz pulse source based on XPM-induced focusing in normally dispersive optical fibers. In 2016 Conference on Lasers and Electro-Optics, CLEO 2016, 2016.

[132] J. Nuño, M. Gilles, M. Guasoni, C. Finot, and J. Fatome. Sampling and magnification technique based on XPM-induced focusing in normally dispersive optical fibers. In Optics InfoBase Conference Papers, 2016.

[133] J. Nuno, M. Gilles, M. Guasoni, and J. Fatome. Amplification technique based on XPM-induced focusing in normally dispersive optical fibers. In 2016 Conference on Lasers and Electro-Optics, CLEO 2016, 2016.

Title: Cross-phase modulation effects in normal dispersive fibers and their applications
Keywords: Domain walls, Nonlinear effects, Polarization

In this Ph.D., physical effects arising from cross-phase modulation between two orthogonally polarized signals propagating in normal dispersion fibers are studied and some of their applications investigated. First, a 40-GHz pulse generator is designed by sending two orthogonally polarized out-of-phase sinusoidal waves in a normally dispersive optical fiber. A large power imbalance between the two waves induces a periodic phase potential for the weak replica which turns the normal dispersive defocusing regime into a focusing dynamics, thus compressing the sinusoidal wave into short and well-separated pulses. A signal sampler and magnifier was then designed using the same principle, sending a high power high frequency sinusoidal pump on one axis of polarization, orthogonally to a long arbitrary shaped pulse with low power. We then report a 40-GHz sampling as well as a magnification factor up to 4. We then report the first observation of polarization domain walls in normal dispersion fibers by first transmitting anticorrelated orthogonally polarized periodic signals in a 10-km long fiber, and then encoding the word 'PETAL' as ASCII on the light waves and transmitting the signal in 2x25km fibers. The information encoded was properly decoded after propagation. Spontaneous apparition of such polarization domain walls was then studied by observing a polarization segregation process of two incoherent and uncorrelated signal. A thermodynamic approach was then used to explain the observed behaviour. The origin of those domain walls, which was theoretically related to isotropic polarization modulation instability, was then investigated. Injecting high power pulses in short segments of very low birefringence fibers, we were able to observe the growth of the theoretical bands in a up to 200m-long fibers, and highlight their extinction for longer strands, while new and unexplained side-bands appeared. Finally, an extension to the Manakov model is explicited taking into account the manufacturing process for the fibers used in the previous experiments.

Titre: Effets de modulation de phase croisée et leurs applications dans les fibres à dispersion normale
Mots Clés: Parois de domaine, Effets non-linéaires, Polarisation

Dans ce manuscrit, les effets émergeant de la modulation de phase croisée entre deux signaux polarisés orthogonalement dans des fibres optiques à dispersion normale sont étudiés et leurs applications approfondies. En premier lieu, un générateur d'impulsions cadencées à 40-GHz a été développé en injectant deux ondes sinusoïdales en opposition de phase polarisées orthogonalement au sein d'une fibre optique à dispersion normale. Une grande différence de puissance entre les deux ondes induit un potentiel de phase périodique pour la réplique de plus faible énergie, induisant ainsi dans régime de dispersion normale une dynamique de compression, comprimant ainsi l'onde sinusoïdale en impulsions courtes et correctement séparées. Un échantillonneur et amplificateur est ensuite démontré en utilisant le même Principe. Une pompe sinusoïdale de forte puissance et à haute fréquence est injectée dans une fibre optique sur un axe de polarisation, orthogonalement à un long pulse de forme arbitraire et de faible énergie. Nous avons alors démontré un échantillonnage à 40-GHz ainsi qu'une amplification jusqu'à un facteur 4. Nous rapportons ensuite la première observation de solitons en parois de domaine de polarisation dans des fibres à dispersion normale en transmettant tout d'abord des trains d'impulsions périodiques anticorrélés et polarisés orthogonalement dans une fibre de 10 km, puis en encodant le mot 'PETAL' en ASCII sur les ondes lumineuses et le transmettant dans une fibre de 2x25km. L'information encodée est correctement décodée après propagation. L'apparition spontanée de ces parois de domaine en polarisation est ensuite étudiée en observant le processus de ségrégation de polarisation entre deux ondes incohérentes et décorrélées. Une approche thermodynamique est ensuite utilisée afin d'expliquer le comportement observé. L'origine de ces parois de domaine, liée théoriquement à l'instabilité de modulation de polarisation isotrope est ensuite étudiée. En injectant des impulsions de fortes puissances dans de courts segments de fibre de très faible biréfringence, nous avons observé l'apparition des bandes théoriques d'instabilité modulationnelle jusqu'à des longueurs de 200m, et mettons en avant leur extinction dans de plus longues fibres. Enfin, une extension au modèle de Manakov est apportée en prenant en compte le processus de fabrication (spun) pour les fibres utilisées pour les expériences précédentes.